

**RAPIDLY SOLIDIFIED ALUMINIUM ALLOYS;  
THE PRECIPITATION BEHAVIOUR AND THE  
MECHANICAL PROPERTIES AFTER  
COMPACTION**

M. VAN ROOYEN

iss  
8

TR diss  
1678

655058

2178898

TR diss 1670

# **RAPIDLY SOLIDIFIED ALUMINIUM ALLOYS;**

## **THE PRECIPITATION BEHAVIOUR AND THE MECHANICAL PROPERTIES AFTER COMPACTION**

# **RAPIDLY SOLIDIFIED ALUMINIUM ALLOYS;**

## **THE PRECIPITATION BEHAVIOUR AND THE MECHANICAL PROPERTIES AFTER COMPACTION**

### **PROEFSCHRIFT**



ter verkrijging van de graad van doctor  
aan de Technische Universiteit Delft,  
op gezag van de Rector Magnificus,  
Prof.dr.s. P.A. Schenck  
in het openbaar te verdedigen ten overstaan  
van een commissie door het  
College van Dekanen daartoe aangewezen,  
op donderdag 3 november 1988  
te 14.00 uur

door

**MAARTEN VAN ROOYEN,**

geboren te Katwijk aan Zee,  
metaalkundig ingenieur

TR diss  
1678

Dit proefschrift is goedgekeurd door de promotoren:  
Prof.dr.ir. B.M. Korevaar  
en  
Prof.dr.ir. E.J. Mittemeijer

This thesis is concerned with a part of the research programme of the Foundation of Fundamental Research of Matter (FOM: Stichting voor Fundamenteel Onderzoek der Materie) and was financially supported by the Technology Foundation (STW: Stichting voor Technische Wetenschappen). The work has been carried out in the Laboratory of Metallurgy of the Delft University of Technology.

**Cover:**

**longitudinal section of consolidate of AlMg (5.6 at.% Mg) ribbons, degassed after precompaction; electrolytically polished; scanning electron micrograph.**

## Stellingen

1. Het onderzoek aan metastabiele, **kristallijne**, metalen verdient, zowel vanuit het oogpunt van de ontwikkeling van materialen met voor de praktijk betekenis hebbende bijzondere eigenschappen als vanuit het hergebruik van schroot, tenminste evenveel aandacht als het onderzoek aan **amorfe** metalen.

R.W. Cahn, Int. J. of Rap. Sol. 1(1984)81-84.

Dit proefschrift

2. De door snel uit de smelt afschrikken verkregen mikrokristalliniteit van aluminiumlegeringen is ter verkrijging van gunstige mechanische eigenschappen in de praktijk belangrijker dan de eveneens optredende oplosbaarheden van toegevoegde elementen groter dan de evenwichtswaarden.

Dit proefschrift.

3. De eenvoudig te bepalen mechanische eigenschap "hardheid" wordt thans te vaak als karakteristiek voor het materiaalgedrag gepresenteerd.

4. In de door Brown en Pratt uitgevoerde berekening van de op de reguliere benadering gebaseerde interactieparameter voor het systeem AlMg blijkt de gasconstante niet te zijn verdisconteerd; daardoor is de door hen gevonden waarde ongeveer een factor 2 te klein.

J.A. Brown and J.N. Pratt, Met. Trans. 1(1970)2743-2750.

5. Op basis van de door Donoso gehanteerde theorie is door het aanpassen, aan de gemeten waarden, van het aangenomen verband tussen de opgeloste fraktie precipitaatdeeltjes in de matrix en de gloeitijd slechts de verhouding van de pré-exponentiële reactiesnelheidsconstante en het kwadraat van de deeltjesgrootte te bepalen en niet ieder van deze factoren afzonderlijk, zoals door deze onderzoeker ten onrechte is aangenomen.

E. Donoso, Mat. Sci. and Eng. 74(1985)39-46.

6. In de verschillende rapporten aan de club van Rome, waarin een beschrijving wordt gegeven van de huidige en toekomstige mondiale milieuproblematiek, en tevens wordt gepoogd een aantal oplossingen te formuleren, wordt voorbijgegaan aan het feit dat de beschreven problematiek primair een religieuze achtergrond heeft; het formuleren van oplossingen op uitsluitend rationele basis is derhalve onmogelijk.

D. Meadows, D. Meadows, J. Randers en W. Behrens, "De grenzen aan de groei", Het Spectrum, Utrecht/Antwerpen, 1973.

M. Mesarovic en E. Pestel, "De mensheid op een kruispunt", Agon Elsevier, Amsterdam/Brussel, 1974.

E. Pestel, "Voorbij de grenzen aan de groei", Meulenhoff Informatief, Amsterdam, 1988.

7. De kwaliteitseisen die worden gesteld aan hen die in het openbaar bestuur betrokken zijn bij de voorbereiding van het beleid, in casu de ambtenaren, dienen ook van toepassing te zijn op degenen belast met de controle daarvan; ontkoppeling van deskundigheid en verantwoordelijkheid kan leiden tot democratisch oncontroleerbare machtsuitoefening.

R. Crinice le Roy, "De Vierde Macht", derde druk, VUGA, s-Gravenhage, 1976.

A.D. Belinfante en J.L. de Reede, Beginselen van Nederlands Staatsrecht, Samsom, Alphen aan den Rijn, 1983.

8. In de wetgeving regelende de samenstelling en werkwijze van de gemeentelijke vestigingscommissie huisartsen is onvoldoende onderkend dat het een relatief machtige beroepsgroep betreft. Via participatie in zowel de selectiecommissie van bovengenoemde commissie als die van de plaatselijke huisartsenvereniging, alsmede via het hanteren van stringente privaatrechtelijke gedragsregels door de beroepsgroep, kan laatstgenoemde een onevenredig grote invloed op het lokale benoemingsbeleid uitoefenen.

9. In het door de Raad voor het Jeugdbeleid aan de regering uitgebrachte advies "Ouderschap zonder onderscheid" wordt ten onrechte geïmpliceerd dat de overheid als neutraal, objectief normstellend orgaan kan optreden.

Raad voor het Jeugdbeleid, "Ouderschap zonder onderscheid", een beleidsadvies over de belangen van kinderen bij verantwoord ouderschap en kunstmatige voortplanting, Ministerie van Welzijn, Volksgezondheid en Cultuur, Rijswijk, september 1988.

10. Bij het onderzoek naar het hechtingsgedrag van kinderen beneden de twee jaar, dit in relatie tot kinderopvang, wordt dit hechtingsgedrag ten onrechte als een geïsoleerde onderzoeksparameter gehanteerd.

M. van Rooyen  
Delft, 3 november 1988

"Hij heeft ieder ding schoon gemaakt op zijn tijd; ook heeft Hij de eeuw in hun hart gelegd, zonder dat een mens het werk, dat God gemaakt heeft, kan uitvinden, van het begin tot het einde toe."

Prediker 3 :11

Ter nagedachtenis van mijn vader

Aan mijn moeder

# TABLE OF CONTENTS

TABLE OF CONTENTS	I
I. INTRODUCTION	1
II. MORPHOLOGY, MICROSTRUCTURE AND PRECIPITATION BEHAVIOUR OF MELT-SPUN ALMG AND ALSI-ALLOYS	5
II.1. RELATION BETWEEN SOLIDIFICATION MORPHOLOGY AND TEXTURE OF MELT-SPUN AL AND AL-ALLOYS (M. van Rooyen, N.M. van der Pers, L. Katgerman, Th. H. de Keijser and E.J. Mittemeijer, "Proc. 5th. Int. Conf. Rap. Quenched Metals", Würzburg, West-Germany; September 3-7, 1984, S.Steeb and H. Warlimont, eds., p. 823).	7
II.2. PRECIPITATION OF GUINIER-PRESTON ZONES IN ALUMINIUM-MAGNESIUM; A CALORIMETRIC ANALYSIS OF LIQUID-QUENCHED AND SOLID-QUENCHED ALLOYS (M. van Rooyen, J.A. SinteMaartensdijk and E.J. Mittemeijer, accepted for publication in Met. Trans. A).	11
II.3. PRECIPITATION OF SILICON IN ALUMINIUM-SILICON; A CALORIMETRIC ANALYSIS OF LIQUID-QUENCHED AND SOLID-QUENCHED ALLOYS (M. van Rooyen and E.J. Mittemeijer, submitted for publication in Met. Trans. A).	29
III. MECHANICAL PROPERTIES OF RAPIDLY SOLIDIFIED ALUMINIUM ALLOYS AFTER HOT COMPACTION	43
III.1. CONSOLIDATION AND RESULTING TENSILE STRENGTH OF MELT-SPUN ALMG AND ALSI ALLOYS (M.van Rooyen, J. A. van der Hoeven, L. Katgerman, P. van Mourik, Th. H. de Keijser and E.J. Mittemeijer, Powder Metallurgy Aerospace Materials Conf., Berne, Switzerland, November 12-14, 1984)	45

III.2. MORPHOLOGY AND MECHANICAL PROPERTIES OF MELT-SPUN AND CONVENTIONALLY CAST ALUMINIUM, ALMG AND ALSI ALLOYS BEFORE AND AFTER HOT EXTRUSION	59
(M. van Rooyen, P.F. Colijn, Th. H. de Keijser and E.J. Mittermeijer, J. Mater. Sci. <u>21</u> (1986)2373).	
III.3. STRUCTURE REFINEMENT AND IMPROVED MECHANICAL PROPERTIES OF AL-20 WT.% SI BY RAPID SOLIDIFICATION IN CONJUNCTION WITH STRONTIUM MODIFICATION	72
(M. van Rooyen, N.M. van der Pers, Th. H. de Keijser and E.J. Mittermeijer, Mat. Sci. and Eng. <u>96</u> (1987)17).	
SUMMARY	81
SAMENVATTING	85
CURRICULUM VITAE	89

## Introduction

The first results on rapid solidification of metals (quenching of the melt) were published in the early sixties [1,2]. This initiated a large number of studies devoted to this alternative route of formation of a solid from the liquid state.

Apart from the obvious interest in the theoretical background of liquid-quenching a great effort involved the development of a manifold of rapid solidification techniques (dependent on the method utilized, at present cooling rates in the range of  $10^3$ - $10^9$  K/s can be achieved [3]). The latter experimental developments were largely due to the potential importance of rapid solidification for practice: liquid-quenching in principle allows the production of new metallic materials possessing special properties (based on either a crystalline or an amorphous structure) and which may not be produced in a conventional way.

**This thesis is concerned with metastable, crystalline, liquid-quenched (by melt-spinning) AlMg and AlSi alloys before and after consolidation by hot extrusion.**

Within the entire field of research on rapidly solidified materials a relatively small amount of work deals with crystalline alloys. For instance, in a review on the fifth international conference on rapidly quenched metals (Würzburg, FRG, September 3-7, 1984) Cahn observed that more of 80 % of the papers were devoted to amorphous materials [4]. Further, it was noted: "Unless some way is found of effectively forcing the practical aspects.....eventually rapid quenching research will die away and its bright promise will be denied". In particular, an investigation into possible applications of rapidly solidified **crystalline** alloys is desired[4].

For obtaining a high cooling rate at least one of the dimensions of the liquid-quenched product is necessarily very small and therefore it has an unfavourable geometry from a technical point of view; in general the as-liquid-quenched materials can not be directly put in practice. Hence, the applicability of liquid-quenched alloys is strongly dependent on the consolidation after rapid solidification.

The importance of aluminium alloys can be demonstrated by considering the world production: 15.5 million tonnes in 1986; compare this with 9.85 million tonnes for copper, 5.47 million tonnes for lead and 6.65 million tonnes for zinc; see Reference 5. Favourable properties of aluminium alloys are their relatively high specific strength and their relatively high corrosion resistance.

A disadvantage of the use of aluminium is the very large amount of energy required for its production. In the last decades there has been a growing interest in the recycling of aluminium alloys since remelting of scrap

consumes only 5 % of the energy needed to produce the same weight of primary aluminium from the ore bauxite[5]. On the other hand, remelting of aluminium alloys in general leads to inferior products, unless a costly refining has been performed. This restricts the usefulness of scrap material as source material to foundry castings, which may contain a limited amount of this secondary aluminium. Hence, apart from allowing the production of new aluminium alloys with special properties, rapid solidification processing could also make possible a wider use of scrap material, because by liquid quenching undesirable, e.g coarse, microstructures can be suppressed.

As compared with conventionally cast alloys, crystalline alloys produced by rapid quenching from the melt can show [ 6,7 ]:

- a decreased grain size, enhancing both strength and ductility [8,9];
- a higher concentration of lattice imperfections (including quenched-in excess vacancies);
- an increased chemical homogeneity;
- an alloying-element solid solubility larger than that according to the equilibrium phase diagram.

Because of these consequences of rapid solidification it is anticipated that also the precipitation behaviour of liquid-quenched (LQ; rapidly solidified) alloys is different from that of solid-quenched (SQ; quenched after solution heat treatment) alloys as the precipitation sequence and the precipitation kinetics are influenced by, among other factors, amount and type of lattice defects and the supersaturation. With a view to practical applications this is of utmost importance, because tuning of the properties of (conventionally cast) aluminium alloys is achieved by applying, appropriate, carefully determined (and frequently standardized) heat treatments, performed after alloy production.

AlSi and AlMg alloys may be considered as model systems, showing extremes of precipitation behaviour. In the case of AlSi alloys a direct precipitation of silicon from the supersaturated solution takes place, whereas decomposition in AlMg alloys proceeds via preprecipitates (Guinier-Preston zones) and intermediate precipitates. The maximal equilibrium solid solubility of Si in the Al lattice equals 1.58 at.% Si at 850 K[10], whereas in the case of Mg 18.9 at.% Mg can be dissolved at 723 K[11].

Within the scope of this thesis the effects of rapid solidification upon the morphology and microstructure of AlSi and AlMg alloys have been examined by light microscopy, X-ray diffraction and transmission electron microscopy .

Differential scanning calorimetry has been employed as the principal technique for the analysis of the heat effects and kinetics of precipitation in LQ alloys of both systems. For comparison also SQ alloys with corresponding compositions have been investigated (see Chapter 1).

Many consolidation processes can be utilized in principle for the compaction of powder materials[12]. A widely used consolidation process is extrusion . Extrusion is usually performed at elevated temperature (hot extrusion), because at room temperature impracticably large extrusion forces are required for obtaining sufficiently intimate metallic contact between the (rapidly solidified) particles.

It is often claimed that liquid-quenched aluminium alloys must be subjected to a degassing treatment before hot extrusion (or any other processing of liquid-quenched material involving elevated temperatures) can be performed. The reasoning is as follows. In the atmosphere aluminium and aluminium alloys are normally covered with an oxide layer [13]. Most oxides are hygroscopic, which implies the bonding of H<sub>2</sub>O-molecules from the atmosphere to the surface of the material. In the case of rapidly solidified products the surface area/volume ratio can be very high, and, hence, a very large amount of H<sub>2</sub>O-molecules can be adsorbed. These H<sub>2</sub>O-molecules are enclosed in the product obtained by a consolidation immediately subsequent to liquid-quenching. A following heat treatment (to establish a desired microstructure) then induces the formation of H<sub>2</sub> within the material according to the overall reaction:



Blisters can be generated in the consolidate and eventually delamination of the material takes place.

A degassing procedure prior to consolidation could remove the adsorbed H<sub>2</sub>O-molecules. The degassing temperature and time are mainly dependent on the adhesive force between the layer of H<sub>2</sub>O-molecules and the oxide layer. In this thesis it is shown that a separate degassing procedure is not always necessary, in particular for AlSi alloys, and in fact, can be disadvantageous as material properties can deteriorate by degassing, e.g. by coarsening of the microstructure (see Chapter 2).

Before the degassing procedure is carried out the as-liquid-quenched products (flakes, ribbons or frozen droplets) are often precompact. Precompaction is employed to obtain a specimen manageable for consolidation. In order to maintain a sufficient gas permeability (for degassing) of the precompact the density to be attained usually equals not more than 85 % of the theoretical density [14-17].

Obviously, annealing after liquid-quenching can have detrimental effects on the microstructure and associated mechanical properties; at elevated temperature recovery, precipitation and coarsening of the matrix grains and second-phase particles can occur. Therefore, the selected combination of liquid-quenching and consolidation methods and of subsequent heat treatment will mostly involve a compromise.

Microstructural steering to prevent as well as possible loss of the gain in (mechanical) properties, achieved by liquid-quenching alone, is desired. In this respect, in the present research project the effect of addition of Sr to AlSi alloys is investigated. It will be shown that in this way an extremely fine microstructure can be obtained with an associated limited coarsening during hot extrusion. As compared to conventionally cast alloys, the ultimate tensile strength and the ductility can be improved with 85 % and 300 % respectively. The present research thereby indicates that development of dedicated alloys opens the Rapid Solidification Processing route for (crystalline) aluminium alloys (see Chapter 3).

## **References**

1. P. Duwez, R.H. Willens and W. Klement, *J. Appl. Phys.* **31**(1960) 1136
2. P. Duwez and R.H. Willens, *Trans. Met. Soc. AIME* , **227**(1963) 362
3. T.R. Anantharaman and C. Suryanarayana, "Rapidly Solidified Metals", *Trans. Tech. SA, Aedermannsdorf, Switzerland*, 1987, p.5
4. R.W. Cahn, *Int. J. Rap. Sol.* **1**(1984) 81
5. "Metallstatistik 1982-1986", *Metallgesellschaft AG (ed.), Frankfurt am Main, FRG*, p. 11
6. H. Jones, *J. Mater. Sci.* **19**(1984) 1043
7. R.E. Maringer, *Sampe Q.* **12**(1980) 30
8. G.E. Dieter: "Mechanical Metallurgy", (Mc.Graw-Hill, London), 2<sup>nd</sup>. ed., 1976, Ch.5.
9. R.P. Carreker, Jr., and W.R. Hibbard, Jr., *Trans. AIME*, **209**(1957) 1157
10. J.L. Murray and A.J. McAlister, *Bull. Alloy Phase Diagram* **5**(1984) 74
11. J.L. Murray, *Bull. Alloy Phase Diagram* **3**(1982) 60
12. A. Lawley: "Powder Metallurgy Processing", (Academic Press, New York), 1978.
13. D. Altenpohl: "Aluminium und aluminiumlegierungen", (Springer-Verlag, Berlin), 1965, Ch. 8.
14. D.P. Voss, *Research Report FB 79-34, DFVLR, Cologne*, 1979.
15. T. Sheppard and P.J.M. Chare, *Powder Metall.* **15**(1972) 17.
16. J. T. Morgan, H.L. Gegel, S.M. Dovaivelu, L.E. Matson, I.A. Martorell and J.F. Thomas, Jr., in "High-Strength Powder Metallurgy Aluminium Alloys", edited by M.J. Koczak and G.J. Hildeman (TMS-AIME, 1982) 193.
17. H.G. Paris, J.W. Mullins and T.H. Sanders, Jr., *ibid.*, 277.

## **II. MORPHOLOGY, MICROSTRUCTURE AND PRECIPITATION BEHAVIOUR OF MELT-SPUN ALMG AND ALSI-ALLOYS**

### **II.1. RELATION BETWEEN SOLIDIFICATION MORPHOLOGY AND TEXTURE OF MELT-SPUN AL AND AL-ALLOYS**

(M. van Rooyen, N.M. van der Pers, L. Katgerman, Th. H. de Keijser and E.J. Mittemeijer, "Proc. 5th. Int. Conf. Quenched Metals", Wurzburg, West-Germany; September 3-7, 1984, S.Steeb and H. Warlimont, eds., p. 823).

### **II.2. PRECIPITATION OF GUINIER-PRESTON ZONES IN ALUMINIUM-MAGNESIUM; A CALORIMETRIC ANALYSIS OF LIQUID-QUENCHED AND SOLID-QUENCHED ALLOYS**

(M. van Rooyen, J.A. SinteMaartensdijk and E.J. Mittemeijer, accepted for publication in Met. Trans. A).

### **II.3. PRECIPITATION OF SILICON IN ALUMINIUM-SILICON; A CALORIMETRIC ANALYSIS OF LIQUID-QUENCHED AND SOLID-QUENCHED ALLOYS**

(M. van Rooyen and E.J. Mittemeijer, submitted for publication in Met. Trans. A).

## RELATION BETWEEN SOLIDIFICATION MORPHOLOGY AND TEXTURE OF MELT-SPUN Al AND Al-ALLOYS

M. van Rooyen, N.M. van der Pers, L. Katgerman\*, Th.H. de Keijser and E.J. Mittemeijer.

Laboratory of Metallurgy, Delft Univ. of Techn., Rotterdamseweg 137, 2628 AL Delft, The Netherlands.

Al, AlMg- and AlSi-alloys were liquid quenched by melt-spinning. The microstructural morphology in cross-sections of the ribbons, as revealed by light-microscopical analysis, was related to the preferred orientations as detected by X-ray diffraction analysis. The present results, in combination with previous data, lead to a model description of the solidification process of melt-spun ribbons.

### 1. INTRODUCTION

By rapid quenching from the melt metastable crystalline alloys can be obtained with increased supersaturation and/or a very fine microstructure<sup>1</sup>. Rapid quenching is frequently achieved by the melt-spinning technique, yielding cooling rates of about  $10^6$  K/s. The heterogeneous microstructure of melt-spun ribbons is still only fragmentarily known<sup>2-4</sup>. This paper reports on the relation between preferred orientations and solidification morphology of melt-spun pure Al, AlMg- and AlSi-alloys applying X-ray diffraction and light-microscopical analyses.

### 2. EXPERIMENTAL

Al, AlMg (3.2, 5.6, 11.2 and 16.5 at% Mg)- and AlSi (1.0, 2.3, 4.4, 7.2, 11.4 and 20.2 at% Si)-ribbons (thickness of 25-50  $\mu\text{m}$  and a width of about 2 mm) were prepared from 99.998 wt% Al, 99.38 wt% Mg and 99.99 wt% Si by impinging a jet of molten alloy onto the cylindrical surface of a rotating copper wheel (circumferential velocity: 23.1 - 46.2 m/s). Melt-spinning was performed in air and the temperature of the melt before ejection was chosen 100 - 150 K above the equilibrium liquids temperature. Light microscopical analysis (phase and interference contrast, conical illumination) was performed on longitudinal sections of the ribbons using a

Neophot-2 microscope (Carl Zeiss, Jena). Pole figures were determined according to the Schulz reflection technique using a Siemens Lücke-type texture goniometer. The intensities were corrected for background and defocusing. Specimens were composed of pieces of ribbon with parallel spinning directions and exposing either all wheel or all upper sides to the X-rays.

### 3. RESULTS

According to X-ray diffraction analysis the AlMg-alloys are single-phase, whereas in the AlSi-alloys both a Si-rich and an Al-rich phase are present [cf. Ref. 2]. Melt-spinning resulted in a very fine microstructure. The grain size decreases with increasing alloy content; the smallest grains occur in the AlSi-alloys. According to the dendrite-arm spacing measurements (cf. Ref. 5) the cooling rate of the central region of the cross-section (where dendrites could be observed) was about  $10^6$  K/s.

The pole figures indicate that all textures are symmetrical with respect to a plane through the ribbon axis and perpendicular to the ribbon surface. The wheel-side pole figure is different from that of the upper side. Pole-figure interpretation shows that some textures are such that simple crystallographic directions are somewhat tilted with respect to the spinning direction.

\* Now with ALCAN International Ltd. Banbury Laboratories, Banbury, Oxon, England OX 167 SP

There is a strong tendency for absence of such a tilt for the wheel-side material. The volume fraction of randomly oriented crystallites increases with increasing alloy content and substrate velocity (in particular for the AlSi-alloys). Randomly oriented crystallites are especially evident in the top layer of the ribbons.

### 3.1. Aluminium

As illustrated by Fig. 2 very small crystallites are present at the wheel side with grain boundaries approximately perpendicular to the wheel surface. The major part of the cross-section shows columnar grains inclined forward with respect to the spinning direction.

The preferred orientation of wheel-side crystallites is different from that of upper-side crystallites (Fig. 2):  $\{110\}\langle 110\rangle$  vs  $\{100\}\langle 110\rangle$  with  $\alpha = 7^\circ$  (for definition of planes and directions see Fig. 1).

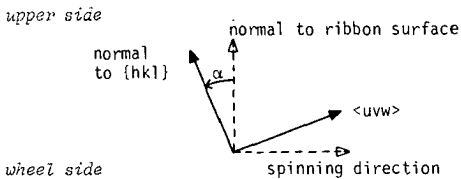


FIGURE 1. Texture  $\{hkl\}\langle uvw\rangle$ ; offset  $\alpha$  ( $\alpha$  not specified means  $\alpha = 0$ );  $\odot$  denotes fibre texture).

### 3.2. Aluminium-Magnesium

For Mg-contents  $\geq 11.2$  at% three zones are present (Fig. 3): At the wheel side small grains occur with grain boundaries approximately perpendicular to the wheel surface. The central zone, comprising a major part of the cross-section, consists of columnar grains inclined forward with respect to the spinning direction; at the ends of the columns the grain boundaries tend to be perpendicular to the ribbon surfaces (S-shaped boundaries, cf. Fig. 3). At the upper side a zone of small equiaxed crystallites oc-

curs; this zone increases in thickness with increasing Mg-content. For small Mg-contents ( $\leq 3.2$  at% Mg) no equiaxed crystallites were observed.

Texture analysis (Fig. 3) showed that at the wheel side  $\{111\}$ -planes tend to be aligned parallel to the surface. In particular for small Mg-contents a tendency to fibre texture is apparent. At the upper side the presence of randomly oriented crystallites is evident. For increasing Mg-content interpretation of the pole figures became increasingly difficult.

### 3.3. Aluminium-Silicon

For large Si-contents the microstructure is such fine that a morphological description in terms of distinct zones, as with the AlMg-alloys, is difficult to give. The micrograph of an AlSi (7.2 at% Si)-alloy (Fig. 4) enables the observation of a featureless zone at the wheel side, a central zone containing fine dendrites/columns inclined forward with respect to the spinning direction and a top layer of very small, possibly equiaxed, grains. The latter layer increases in thickness with increasing Si-content. For small Si-contents second-phase Si-rich particles along dendrite boundaries can be discerned (cf. Fig. 1a in Ref. 4).

Texture analysis of the Al-rich phase (Fig. 4) shows that at the wheel side  $\{110\}$ - and  $\{100\}$ -planes tend to be aligned parallel to the surface. The top layer consists of randomly oriented crystallites; most pronounced at large Si-contents. For increasing Si-content the interpretation of the pole figures became increasingly difficult.

According to the pole figures of the Si-rich phase, both for wheel and upper side, the Si-rich phase is randomly oriented.

Solidification morphology and texture of melt-spun Al and Al-alloys

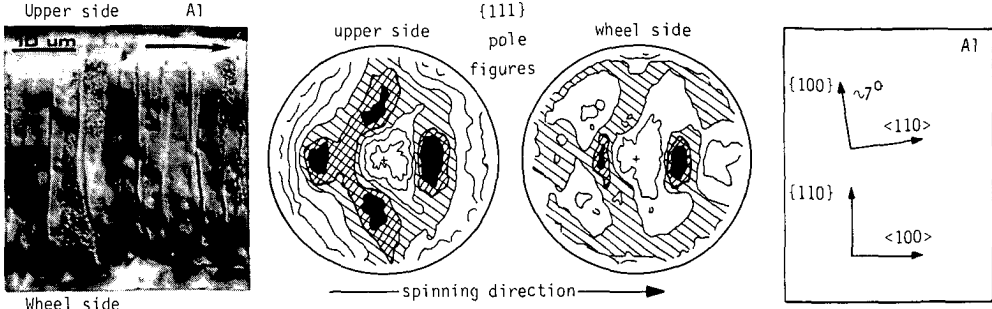


FIGURE 2. Optical micrograph , pole figures (highest intensity black) and schematic texture of melt-spun pure Al ribbons.

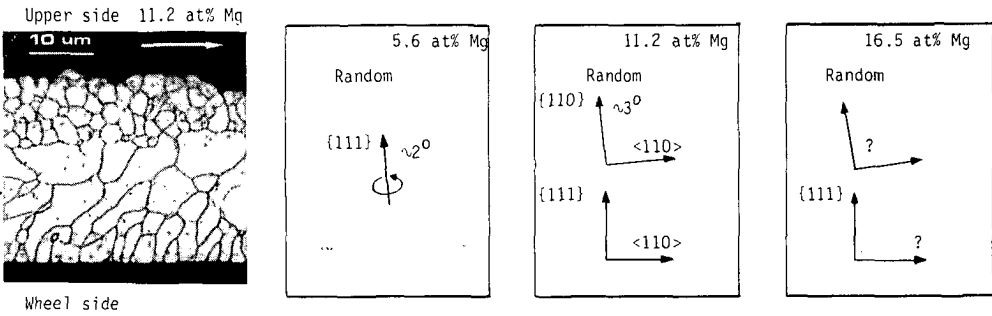


FIGURE 3. Optical micrograph of AlMg (11.2 at% Mg) and schematic texture of melt-spun AlMg-ribbons as a function of Mg-content.

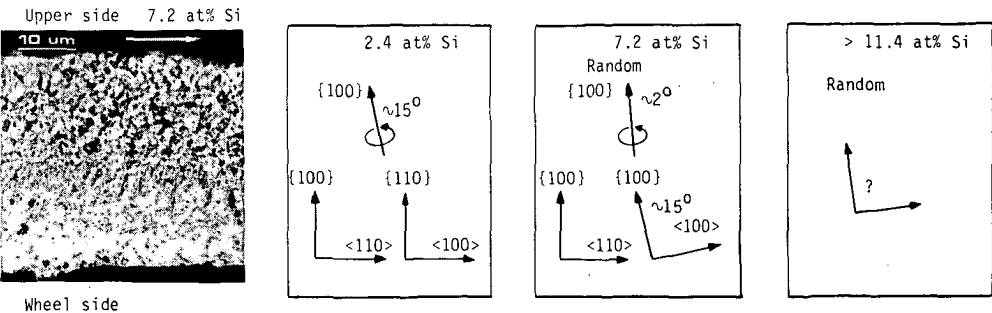


FIGURE 4. Optical micrograph of AlSi (7.2 at% Si) and schematic texture of melt-spun AlSi-ribbons as a function of Si-content.

#### 4. DISCUSSION

It can be shown from calculations based on thermodynamics and solidification kinetics that AlSi, as compared with AlMg, is a relatively difficult alloy system to achieve complete solid solubility by liquid quenching<sup>6</sup>. This agrees with the observation of single-phase AlMg- and two-phase AlSi-alloys in this investigation.

Obviously, the highest cooling and solidification rates occur at the wheel side (chill zone). This leads to very small crystallites in this region (showing a sometimes even "featureless" light-microscopical appearance), and the largest amount of dissolved alloying element (for the AlSi-alloys cf. Ref. 2, 4). Also, the structural imperfection as determined by X-ray diffraction line-broadening analysis is largest in the chill zone<sup>3</sup>. Further, the nearby presence of the heat sink induces a local thermal gradient perpendicular to the wheel surface and this serves to explain an initial development of grain boundaries perpendicular to the wheel surface.

The wheel-side texture in general is not a fibre texture, as one may intuitively expect, but it is symmetrical with respect to the longitudinal section of the ribbon. This could hint at the presence of mechanical stresses during solidification.

The uni-directional heat flow condition in the puddle leads to columnar grains. It was shown (7, 8) that the thermal gradient in the puddle has an inclination in the reverse direction, whereas the gradient of maximal constitutional undercooling has a forward inclination. This could explain the occurrence of columns inclined forward with respect to the spinning direction.

The presence of equiaxed crystallites in the top layer is ascribed to a relatively slow heat transfer. This leads to nucleation in the liquid (constitutional undercooling). In combi-

nation with convection in the liquid, equiaxed grains develop, which are randomly oriented.

The above ideas for the solidification history of melt-spun ribbon, showing the three-zone morphology, imply that segregation of alloying element occur in particular in the central region, as was demonstrated recently<sup>4</sup>.

The increased fineness of microstructure, the increase of the amount of randomly oriented crystallites and the decrease of distinctness of preferred orientation with increasing alloying element content can be due to the hindrance of preferred growth by micro-segregation (AlMg) and/or second-phase particles (AlSi), both at grain boundaries.

#### ACKNOWLEDGEMENTS

The authors are indebted to Mr. P.F. Colijn and Ir. P. van Mourik for optical microscopy and X-ray diffraction lattice parameter determinations respectively. Financial support of the Foundation for Fundamental Research of Matter (F.O.M.) is gratefully acknowledged.

#### REFERENCES

1. H. Jones, *J.Mater.Sci.*19(1984)1043.
2. A. Bendijk, R. Delhez, L. Katgerman, Th.H. de Keijser, E.J. Mittemeijer and N.M. van der Pers, *J.Mater.Sci.*15(1980)2803.
3. R. Delhez, Th.H. de Keijser, E.J. Mittemeijer, P. van Mourik, N.M. van der Pers, L. Katgerman and W.E. Zalm, *J.Mater.Sci.* 17(1982)2887.
4. J.A. van der Hoeven, P. van Mourik and E.J. Mittemeijer, *J.Mater.Sci. Letters* 2(1983)158.
5. H. Matyja, B.C. Giessen and N.J. Grant, *J. Inst. Metals* 96(1968)30.
6. L. Katgerman, *Scripta Met* 17(1983)537.
7. K. Takeshita and P.H. Shingu, *Trans. J.I.M.* 24(1983)529.
8. L. Katgerman, this conference.

# PRECIPITATION OF GUINIER-PRESTON ZONES IN ALUMINIUM-MAGNESIUM; A CALORIMETRIC ANALYSIS OF LIQUID-QUENCHED AND SOLID-QUENCHED ALLOYS

M. van Rooyen, J. A. Sinte Maartensdijk\* and E.J. Mittemeijer

Laboratory of Metallurgy, Delft University of Technology, Rotterdamseweg  
137, 2628 AL Delft, The Netherlands.

\* Now with Kemira B.V., Moezelweg 151, 3198 LS Rozenburg,  
The Netherlands

A calorimetric analysis of precipitation in liquid-quenched (LQ; rapidly solidified) and solid-quenched (SQ; quenched after solution heat treatment) AlMg alloys was made. Nonisothermal annealing (constant heating rate) experiments (differential scanning calorimetry) were performed using specimens of various compositions (12-17 at% Mg) aged at fixed temperatures (293-353 K) during variable times (up to 3 years). Constraints to be imposed on the heating rates to be applied were discussed. Attention was paid in particular to the formation on ageing and dissolution on subsequent annealing of Guinier-Preston (GP) zones. Quantitative analysis of the heat of dissolution of GP-zones led to estimates for the GP-zone solvus and the enthalpy of formation of GP-zones. The kinetics of formation and dissolution of GP-zones can be interpreted in terms of nucleation and excess-vacancy enhanced diffusion of magnesium. Rates of formation and dissolution of GP-zones are higher for SQ-alloys than for LQ-alloys, which is caused by a higher amount of excess vacancies retained after drastic SQ as compared to LQ by melt spinning where cooling in the last part of the quench can be relatively slow. The activation energy of GP-zone dissolution is generally smaller than that of GP-zone formation, which is interpreted in terms of a precipitation model where vacancy voids/loops, formed during quenching and/or in the beginning of ageing, become unstable at temperatures where the GP-zones dissolve. As compared to the precipitation of GP-zones, the precipitation of  $\beta'/\beta$  particles showed an "opposite" kinetic behaviour: it starts earlier in the LQ-alloys than in the SQ-alloys, which is ascribed to heterogeneous nucleation at structural heterogeneities (as grain boundaries) present with a higher density in the LQ-alloys.

## 1. Introduction

Ageing of an aluminium-rich matrix (face centred cubic) supersaturated with dissolved magnesium, can ultimately lead to the precipitation of  $\beta$  ( $\text{Al}_3\text{Mg}_2$ : face centred cubic) particles (see phase diagram<sup>[1]</sup>). However, a number of metastable phases, which can occur before the emergence of the equilibrium phase ( $\beta$ ), have been reported.

There is general agreement concerning the occurrence of an intermediate  $\beta'$  ( $\text{Al}_3\text{Mg}_2$ : hexagonal) phase immediately preceding the  $\beta$  phase. But no consensus exists with respect to possible preprecipitates. Guinier-Preston (GP) zone formation can occur during ageing at relatively low (e.g. room) temperature of AlMg alloys homogenized at elevated temperature and subsequently quenched (denoted as solid-quenched (SQ) alloys). Some authors report that at least about 10 at% Mg should be dissolved for GP-zone formation to occur at room temperature<sup>[2,3]</sup>, whereas others claim that this critical amount equals about 5 at% Mg<sup>[4,5]</sup>. Enhanced ageing may lead to a more stable intermediate phase (as derived from a shift to a higher temperature of the endothermal DSC (Differential Scanning Calorimetry) peak ascribed to the GP-zone dissolution on non-isothermally heating (constant heating rate) an aged alloy). This phase has been interpreted as an ordered "GP-zone" (denoted as  $\beta''$ <sup>[4]</sup> or  $\delta'$ <sup>[5]</sup>) possibly with a  $\text{L}1_2$ -type superstructure ( $\text{Al}_3\text{Mg}$ )<sup>[6,7]</sup>.

Only a few data exist about the ageing of aluminium alloys prepared by rapid solidification from the liquid state (denoted as liquid-quenched (LQ) alloys). As compared to SQ-alloys, in general one may expect that the initially high cooling/ solidification rate for LQ-alloys has large effects on the ageing kinetics. This has been demonstrated by recent experiments with AlSi-alloys and was

ascribed to a relatively high amount of excess vacancies and a very fine grain structure<sup>[8]</sup>. However, in some cases relatively low values have been reported for the excess-vacancy concentration after liquid-quenching<sup>[9]</sup> (see also results presented in this paper).

The purpose of this paper is to investigate by calorimetric analysis heat effects and kinetics of the formation and dissolution of preprecipitates in both LQ and SQ AlMg-alloys. Important stimuli for this work are the following: (i) the totally different precipitation behaviour expected for LQ AlMg-alloys as compared to the previously investigated LQ AlSi-alloys<sup>[10]</sup> (no preprecipitates or intermediate phases have been reported for AlSi); (ii) the role of the type of quenching performed; in the only previous work known to us on precipitation in LQ AlMg alloys it was claimed that no GP-zone formation occurs<sup>[11]</sup>.

## 2. Experimental procedure

### 2.1. Preparation and ageing of alloys

Liquid-quenched (LQ) AlMg-alloys containing 12.1, 12.8, 15.9, 16.1 and 17.2 at% Mg were prepared by melt-spinning (for details see Reference 12). Solid-quenched (SQ) material was obtained by annealing melt-spun ribbons in a hydrogen atmosphere (flow rate 40.7 cm/min) during 5 minutes at 723 K succeeded by quenching in ice water.

X-ray diffraction analysis (Debye-Scherrer photographs) demonstrated that all magnesium was in solid solution immediately after liquid or solid quenching; a second phase could not be detected.

Ageing experiments were performed at room temperature and at temperatures up to 353 K in a thermostatically controlled oil bath (Tamson, type TC (V), temperature control within 1 K).

## 2.2. Calorimetry

After ageing the ribbons were cleaned with trichloroethylene and ethylalcohol. Thereafter they were chopped into small pieces. The calorimetric measurements were performed with a differential scanning calorimeter (Perkin-Elmer, DSC-2). Both the sample and the reference holder were made of graphite. A protective gas atmosphere of pure argon was employed.

For determination of the enthalpy changes in all the cases a heating rate of 20 K/min was used (temperature range from 310 K until 723 K (= eutectic temperature of AlMg)).

For determination of the activation energy of the dissolution of the GP-zones the so-called Kissinger analysis was applied, using heating rates of 5, 10, 20 and 40 K/min (for a justification of the applicability of the Kissinger analysis to heterogeneous reactions in the solid state, see Reference 27).

Per sample two DSC-runs were successively performed; the second run was carried out in order to obtain the baseline.

### 3. Constraints for the heating rate

Consider the schematic phase diagram presented in Figure 1(a). On ageing at temperature  $T_{\text{start}}$  an aluminium matrix initially supersaturated with magnesium (composition  $x_0$ ), GP-zones develop. After a certain time of ageing,  $t$ , the composition of the matrix has decreased and become  $x_t$ . By performing subsequently (nonisothermal) annealing experiments in a calorimeter (Differential Scanning Calorimetry) both the enthalpy change associated with and the kinetics of the dissolution of the GP-zones formed by ageing at  $T_{\text{start}}$  can be analysed from the corresponding endothermic effect. Only for a limited range of heating rates reliable data can be obtained. During the anneal, with constant heating rate, a path in

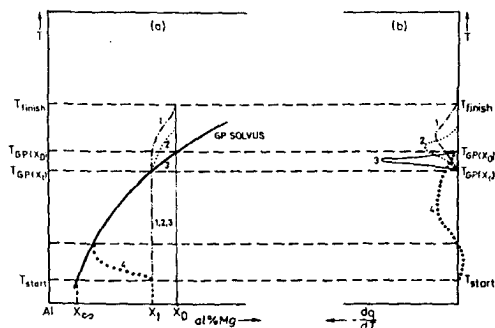


**Fig. 1.**

(a). Schematic presentation of the path followed by the AlMg-matrix composition in the AlMg phase diagram (Al-rich side) on heating from  $T_{\text{start}}$  to  $T_{\text{finish}}$  as a function of heating rate  $\Phi$ . It holds:  $\Phi_1 > \Phi_2 > \Phi_3 > \Phi_4$ , where the subscript corresponds with the path followed.  $x_0$ ,  $x_t$  and  $x_\infty$  denote the Al-matrix composition after ageing times 0,  $t$  and  $\infty$  at the start temperature.

(b). Schematic presentation of the corresponding DSC-scans.

( $\frac{dq}{dt}$  = rate of heat generation).

the phase diagram for the composition of the matrix can be indicated: the heating rate increases for the paths indicated in Figure 1(a) in the order 4-3-2-1.

#### 3.1. Analysis of enthalpy change

If the decomposition process of the matrix on ageing at  $T_{\text{start}}$  has not been completed, a (small) exothermic effect can occur in a subsequent anneal with a relatively low heating rate, as a consequence of continued GP-zone formation, before the large endothermic effect corresponding to GP-zone dissolution occurs (see path 4 and corresponding DSC-curve in Figures 1(a) and (b)). Hence, for the analysis of the enthalpy change of GP-zone dissolution, the heating rate should be at least as large as that corresponding to path 3 in Figure 1(a): vertical

path for  $T < T_{GP}(x_t)$ , thus avoiding GP-zone formation on annealing. This minimal heating rate is the smaller, the smaller  $x_t$  (because the driving force for GP-zone formation decreases on continued ageing).

For heating rates larger than or equal to the minimal one, the start temperature of the endothermic peak is equal to or larger than  $T_{GP}(x_t)$ . The minimal heating rate required for a vertical path in the phase diagram below the GP solvus ( $x = x_t$ ;  $T < T_{GP}(x_t)$ ) may be that large that for  $T > T_{GP}(x_t)$  the path followed does not necessarily coincide with the GP-solvus, but it could be located above it. Hence, the end temperature of the endothermic peak for the minimal heating rate can be equal to or larger than  $T_{GP}(x_0)$ .

For heating rates smaller than or equal to that corresponding to path 3, such that the GP-solvus is followed at least for the late stages of GP-zone dissolution, the end temperature in the DSC-curve for the GP-zone dissolution peak equals the GP-solvus temperature corresponding to the gross content  $x_0$  ( $T_{GP}(x_0)$ ; Figures 1(a) and (b)).

### 3.2. Analysis of the activation energy

In order to analyse the (Arrhenius) kinetics of the GP-zone dissolution process, the heating rate should be that large that this dissolution process is governed by the atomic mobility; at least, the matrix composition should not follow the GP-zone solvus (see also References 14 and 15).

For heating rates smaller than or equal to that of path 3 the rate of GP-zone dissolution can be determined by the course of the matrix composition along the GP-solvus; the rate of GP-zone dissolution then is governed by the slope of the GP-zone solvus.

For heating rates well above that of path 3 (see paths 2 and 1 in Figure 1(a)) atomic mobility can be rate limiting for the dissolution. Then the DSC-peak signal shifts

to higher temperatures (see Figure 1). However, a very high heating rate induces large thermal gradients within the specimens leading to kinetical inhomogeneity. In practice rates in the range 5-40 K/min are employed.

## 4. Heat effects

### 4.1. General interpretation

All magnesium was in solid solution immediately after liquid quenching (cf. section 2.1.). Ageing at room temperature led to GP-zone formation. In Figures 2(a) and 2(b) DSC-scans of liquid-quenched (LQ) AlMg alloys, recorded after the indicated number of hours of ageing at room temperature, are presented. Both the first scan and the rescan of each alloy are shown. The endothermic peak with a maximum at about 370 K is ascribed to the dissolution of GP-zones formed on ageing. The rescan, recorded immediately after cooling from the maximum temperature reached in the first run, indeed does not show the endothermic effect. It is noted that the peak temperature increases with ageing time at a constant ageing temperature (see Figure 3). This may be attributed to coarsening of GP-zones during ageing, causing retardation of the dissolution of the GP-zones on nonisothermal annealing with constant heating rate, which leads to a higher peak temperature. (Larger GP-zones are more stable (Gibbs-Thomson effect) and require more time to dissolve).

The exothermic peak at about 530 K in both the first scan and the rescan corresponds with the precipitation of  $\beta'/\beta$  particles, while the following endothermic effect is caused by the subsequent dissolution of these precipitates. A rescan recorded after slowly cooling (20 K/min; Figure 2(a)) from the maximum temperature reached in the first scan, only exhibits the endothermic

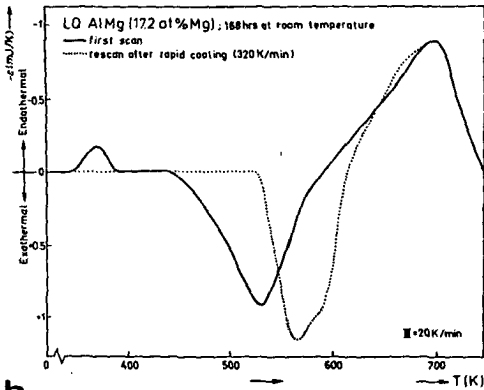
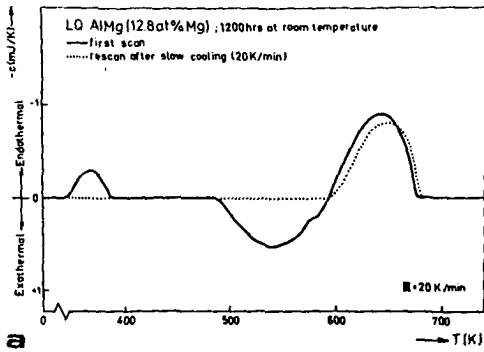


**Fig. 2.**  
**(a).** DSC scan and rescan of LQ AlMg (12.8 at% Mg) aged for 1200 h at room temperature (specimen weight 6.020 mg).  
**(b).** DSC scan and rescan of LQ AlMg (17.2 at% Mg) aged for 168 h at room temperature (specimen weight 7.960 mg).

effect due to the dissolution of the  $\beta'/\beta$  phase precipitated during the cooling process, whereas a rescan recorded after fast cooling (about 320 K/min; Figure 2(b)) shows the exothermic and endothermic effects due to the precipitation and dissolution respectively of the  $\beta'/\beta$  phase.

In all rescans the start temperature of the  $\beta'/\beta$  peak was shifted to a higher temperature as compared to the first scan. This suggests that the amount of structural heterogeneities facilitating nucleation (like

dislocations/vacancy loops (see below) and grain boundaries) had decreased during the first anneal (light-microscopical analysis indeed showed a very significant grain growth for 5 min. annealing at 723 K; see Figures 6(a) and (b)).

The onset of the  $\beta'/\beta$  peak was independent on the presence or absence of the endothermic GP-zone dissolution peak. Further, in all cases (except for an ageing temperature of 353 K, which is discussed later) no overlap of, but a clear separation instead between, the peak due to the dissolution of GP-zones and the peak due to the precipitation of  $\beta'/\beta$  could be discerned. Both observations indicate no direct relation between GP-zones and subsequent  $\beta'/\beta$  precipitates; on annealing the GP-zones dissolve before  $\beta'/\beta$  precipitates. These results can be consistent with the following precipitation model: after quenching clustering of both dissolved atoms (GP-zone formation) and of vacancies (void/loop-formation) occurs. On ageing ordering within and growth of the GP-zones can take place. On subsequent annealing the vacancy voids/loops can still exist at temperatures where the GP-zones are dissolved already<sup>[16]</sup>,

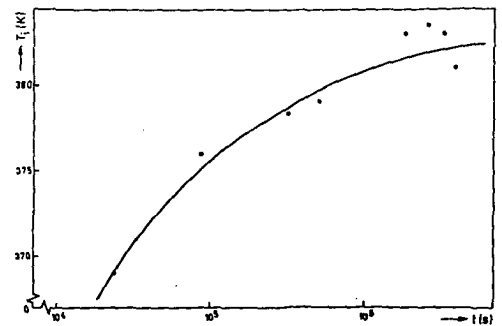


**Fig. 3.** Peak temperature,  $T_p$ , of the GP-zone dissolution peak as a function of ageing time,  $t$ , at 313 K for LQ AlMg (15.9 at% Mg);  $\Phi = 20$  K/min.

see also TEM data in Reference 17. These vacancy voids/loops then can serve as nucleation sites for semi- or incoherent  $\beta'/\beta$  precipitates. Hence the present results do not support a precipitation model<sup>[18]</sup> where a gradual transformation occurs of a GP-zone into a  $\beta'/\beta$  particle at the same location in the specimen.

#### 4.2. Liquid-quenching versus solid-quenching

##### 1. GP-zone formation

Solid-quenched material was prepared by annealing melt-spun ribbons during 5 minutes at 723 K succeeded by quenching in water (273 K). It should be noted that in this way an unusually high cooling rate for solid quenching is achieved as a consequence of the small ribbon thickness (about 30  $\mu\text{m}$ ).

Comparison of the heat effect of LQ AlMg with that of SQ AlMg shows that the rate of formation of GP-zones was much higher in the case of SQ AlMg: e.g. one half hour of ageing at room temperature of SQ AlMg (16.1 at% Mg) corresponded with an endothermic effect equal to that after 2800 hours of ageing of the analogous LQ-alloy. Further, the peak of the endothermic dissolution process occurred at about 348 K for the SQ-alloy in contrast with that at about 379 K for the LQ-alloy (heating rate: 20 K/min).

These results strongly suggest that the amount of quenched-in excess vacancies was significantly larger after the present (extreme) method of solid quenching than after liquid quenching by melt spinning. This interpretation is corroborated by activation-energy data given in section 7.2. Excess vacancies initially retained after liquid quenching may be annihilated or precipitate as vacancy loops as a consequence of the, melt-spinning inherent, relatively slow cooling rate in the lower temperature region of the quench\* and/or, realizing that grain

boundaries can act as vacancy sinks, the relatively large grain-boundary area in LQ-alloys may also lead to a relatively small excess-vacancy concentration.

\* In a previous paper<sup>[19]</sup> the presence of equi-axed crystals in the top layer of the melt-spun ribbons was considered as a (possible) result of incomplete solidification at the moment the (partly solidified) ribbon got off the spinning wheel, which also suggests a relatively slow cooling rate in the last stage of cooling.

##### 2. $\beta'/\beta$ precipitation

DSC-scans recorded from LQ and SQ AlMg-alloys containing 12.8 and 16.1 at% Mg and aged at room temperature during times indicated are presented in Figures 4 and 5. The exothermic  $\beta'/\beta$ -precipitation peak recorded from LQ AlMg (12.8 at% Mg) appears to be the composite of two overlapping peaks. The rescan, measured after fast cooling (320 K/min) from the maximum temperature in the first scan, shows a single exothermic precipitation peak at about the location of the apparent second peak in the composite peak of the first run (Figure 4). The exothermic precipitation peak recorded from the corresponding SQ AlMg (12.8 at% Mg) alloy is identical to that of the discussed rescan of the LQ AlMg (12.8 at% Mg) alloy. (The  $\beta'/\beta$  precipitation-peak area in the rescan after fast cooling of the LQ -alloy is smaller than that of the first scan, because the precipitation starts at a higher temperature in the rescan implying a smaller amount of precipitated phase in the latter case (cf. phase diagram); as a consequence the area of the subsequent dissolution peak is smaller too in the rescan).

The exothermic  $\beta'/\beta$ -precipitation peaks in the first scan and the rescan recorded from LQ AlMg (16.1 at% Mg) as well as that in the scan recorded from the corresponding SQ-alloy all appear to be the composite of

two neighbouring peaks. The  $\beta'/\beta$ -precipitation heat effect starts earliest in the first scan of the LQ AlMg(16.1 at% Mg) alloy; the peak temperature in the scan of the SQ AlMg(16.1 at% Mg) alloy is about the same as that in the first scan of the corresponding LQ-alloy.

These results can be interpreted as follows. As compared to SQ AlMg alloys, the precipitation of  $\beta'/\beta$  starts at a lower temperature in the LQ AlMg alloys because the amount of structural heterogeneities providing easy nucleation sites for precipitates is clearly larger after LQ than after SQ (compare also first scans and rescans and see discussion in section 4.1.); for TEM evidence demonstrating the preferential nucleation of  $\beta'$  and  $\beta$  particles on dislocations and grain boundaries: Reference 17. Optical microscopy confirmed that the amount of grain-boundary area is much larger in LQ-alloys than in SQ-alloys; cf. Figures 6(a) and 6(b). Then, in particular for the LQ-alloy, the precipitation sequence  $\beta' \rightarrow \beta$  can be expected which can be consistent with a precipitation peak in the DSC-scans composed of two overlapping peaks (see also discussion of Figure 8 in section 5). In view of its higher degree of structural perfection, a larger driving force for precipitation is needed in the case of the SQ-alloy. In combination with a relatively small amount of dissolved magnesium, as in the alloy containing 12.8 at% Mg, this could lead to precipitation at a higher temperature such that a direct occurrence of  $\beta$  phase is possible, corresponding to a single peak at the location of the second peak in the composite peak discussed for the LQ-alloy (see Figure 4 for AlMg (12.8 at% Mg)). However, if a large amount of dissolved magnesium occurs, the driving force may be that large that relatively easy nucleation is still possible leading to the precipitation sequence  $\beta' \rightarrow \beta$  and a composite peak in the DSC-scan occurs (see DSC-scans for SQ AlMg (16.1 at% Mg) in Figure 5).

## 5. Heat of dissolution and solvus of GP-zones

The heat of dissolution of the ageing-induced GP-zones is shown as a function of ageing time at the temperature indicated in

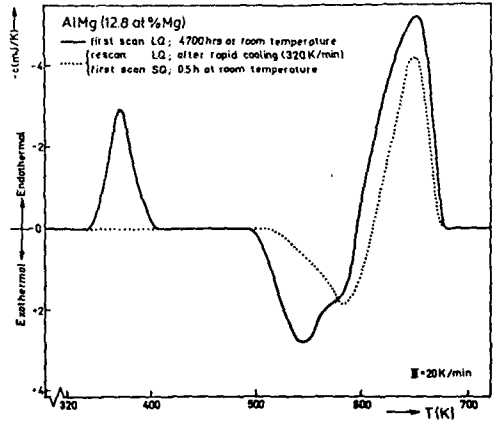


**Fig. 4.**

DSC scan of both LQ (aged for 4700 h at room temperature) and SQ (aged for 0.5 h at room temperature) AlMg (12.8 at% Mg) (specimen weight LQ: 16.920 mg and specimen weight SQ: 13.850 mg).

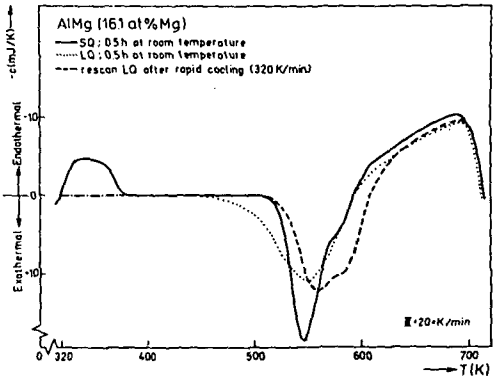


**Fig. 5.**

DSC scan of LQ as well as SQ AlMg (16.1 at% Mg), both aged for 0.5 h at room temperature (specimen weight LQ: 18.730 mg and specimen weight SQ: 13.940 mg).

Figures 7(a) through (d) for LQ AlMg containing about 16 at% Mg (composite of the curves is represented in Figure 7(g) and in Figures 7(e) and (f) for LQ AlMg-alloys containing about 12 at% Mg. After an incubation time of ageing (depending on composition and ageing temperature), the endothermic dissolution effect was observed. Eventually a plateau for the heat of dissolution was reached, indicating a completed GP-zone precipitation (for the ageing at 353 K see below). The height of this plateau increased with decreasing ageing temperature and increasing magnesium

content, which is consistent with a shape and location of the GP-zone solvus as indicated in Figures 1 and 10.

Ageing at 353 K led to an anomalous behaviour for the heat of dissolution (Figure 7(d)). After about  $10^5$  s of ageing the initially single GP-zone dissolution peak (peak maximum at about 380 K) is apparently composed of two overlapping peaks (see Figure 8). This may be ascribed to the occurrence of an ordering process in the GP-zones which could happen after long times of ageing according to literature data<sup>4,5</sup>. At this stage an overlap between the GP-zone dissolution peak and the  $\beta'$ / $\beta$ -precipitation peak develops (this overlap hinders an accurate determination of the heat of dissolution; see Figure 8); such an overlap was not observed in all other experiments (see section 4.1.). The overlap suggests that an ordered GP-zone may be conceived as a precursor for a  $\beta'$ -precipitate, in contrast with the unordered GP-zone. In this connection it may be remarked that for long times of ageing a clear splitting of the  $\beta'$ / $\beta$ -composite peak into a  $\beta'$  and a  $\beta$ -peak occurs (Figure 8)\* which may be considered as a consequence of the suggested association of an ordered GP-zone with  $\beta'$ -precipitate. In the rescans no splitting of the  $\beta'$ / $\beta$ -peak occurs (Figure 8) which is consistent with the above picture, since the specimen used for the rescans obviously does not contain ordered GP-zones (for further discussion see at the end of this section).

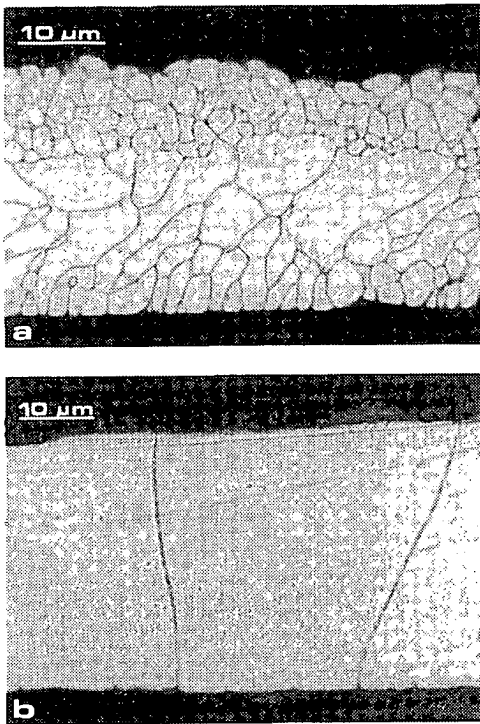


**Fig. 6.** Longitudinal section of AlMg (15.9 at% Mg)-ribbons (etched with Keller and Wilcox's reagent; optical micrograph: bright field; oil immersion):

- a. As liquid quenched.
- b. After annealing for 5 min. at 723 K.

\* Aged AlMg (15.9 at% Mg)-ribbon material was annealed up till appearance of the first or the second maximum of the  $\beta'$ / $\beta$  composite peak. Subsequent X-ray diffraction analysis of these specimens demonstrated that the second peak can be ascribed unambiguously to precipitation of  $\beta$ -phase particles; the first peak is likely to be due to  $\beta'$  precipitation since weak diffraction lines are observed consistent with the presence of  $\beta'$ -phase particles.

The value of the plateau for the heat of dissolution after completed GP-zone precipitation at room temperature (implying ageing times over more than 3 years), is plotted versus the gross magnesium content of the alloy in Figure 9. A linear relation exists between the heat of dissolution and the gross magnesium content. From the graph it follows that the minimum magnesium content in order to accomplish GP-zone formation at room temperature equals 10 at%. In earlier work<sup>[21]</sup> it was found that an increase in hardness of AlMg-alloys occurred at room temperature if the magnesium content was larger than about 10 at% Mg, which is consistent with the above interpretation of the calorimetric results. In Reference 4 no GP-zone formation could be detected by DSC-analysis in an AlMg (5.1 at% Mg) alloy, in agreement with the present data; however, in Reference 20 an extremely small endothermic effect was observed for an AlMg (5 wt% Mg) alloy which was tentatively ascribed to dissolution of GP zones formed by ageing.

The GP-zone solvus may now be estimated as follows. To assess the free enthalpy of mixing a modified regular solution model introduced by Hillert<sup>[21]</sup> can be fitted to experimental data of the stable solvi of both the Al-rich and the Mg-rich side of the phase diagram. Further, for the calculation of the coherent binodal and the coherent spinodal a strain energy term as given by Cahn<sup>[22]</sup> is added (See Appendix for details of calculation). From the above discussed experimental data it is concluded that the point (10 at% Mg, room temperature) belongs to the GP-zone solvus. Then, conceiving the coherent binodal as the effective GP-zone solvus, it can now be calculated by taking Young's modulus of the solid solution such that the point (10 at% Mg, room temperature) lies on the coherent binodal. This occurs if Young's modulus is taken as 66% of the value which holds for

pure aluminium in the  $\langle 100 \rangle$  direction (the latter taken as  $63.7 \times 10^9 \text{ N/m}^2$ <sup>[23]</sup>). In this connection the following remarks can be made: (i) for aluminium  $\langle 100 \rangle$  is the direction of the least dilatational elastic coefficient; (ii) it is well known that Young's modulus decreases significantly on alloying with magnesium<sup>[24]</sup> (This could imply that, as compared with the above estimate, both the coherent binodal and the coherent spinodal should be located at somewhat higher temperatures for magnesium contents appreciably larger than 10 at%) and (iii) other factors in the strain energy (cf. Appendix) are only slightly dependent on composition.

The coherent binodal estimated as described above and the corresponding coherent spinodal are shown in Figure 10; the composition and corresponding ageing temperatures of the alloys considered in this study are also indicated. In any case, the alloys dealt with have been aged outside the coherent spinodal. This implies that the formation of GP-zones in these alloys occurs by a process of nucleation and growth (see also discussion of activation energy in section 7). The location of the two alloys outside the estimated coherent binodal (taken as GP-zone solvus) may be ascribed to crudeness of the model for the calculation of the coherent binodal and the values taken for its parameters. Further, any solvus for GP-zones has a relative meaning: (i) on ageing some stabilization (e.g. by ordering/coarsening) of the GP-zones occurs as indicated by a shift to higher temperatures of the GP-zone dissolution peak (Figure 3), and (ii) continued ageing at elevated temperature may lead to dissolution of the GP-zones formed initially in favour of  $\beta'$  precipitates (see Figures 7(d) and 8 and discussion above). It may be concluded that the GP-zone solvus changes of position in the phase diagram during ageing. Only for those ageing experiments where a plateau for the

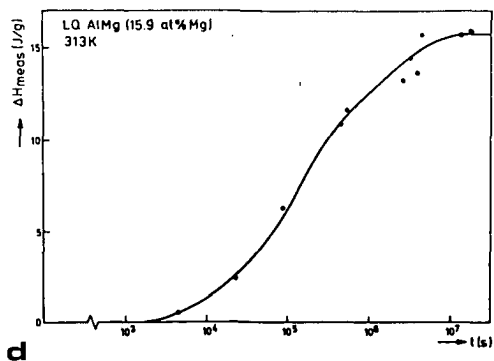
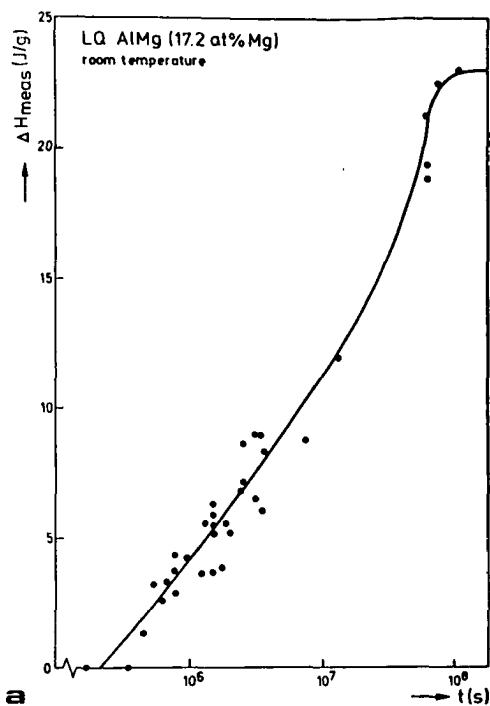


**Fig.7.**

**a.** Enthalpy change for GP-zone dissolution,  $\Delta H_{meas}$ , for LQ AlMg (17.2 at% Mg) aged at room temperature as a function of ageing time  $t$ .

**b.** Enthalpy change for GP-zone dissolution,  $\Delta H_{meas}$ , for LQ AlMg (15.9 at% Mg) aged at 313 K as a function of ageing time  $t$ .

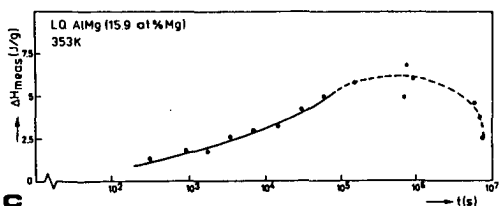
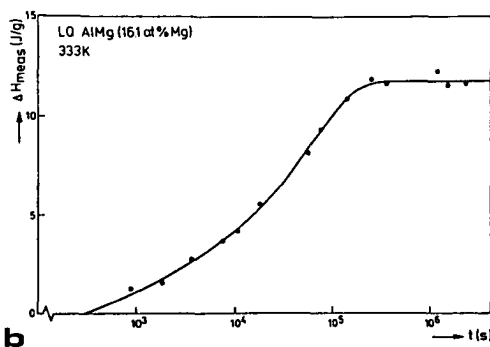
**c.** Enthalpy change for GP-zone dissolution,  $\Delta H_{meas}$  for LQ AlMg (16.1 at% Mg) aged at 333 K as a function of aging time  $t$ .

**d.** Enthalpy  $\Delta H_{meas}$ , for LQ AlMg (15.9 at% Mg) aged at 353 K as a function of ageing time  $t$ .

**e.** Enthalpy change for GP-zone dissolution,  $\Delta H_{meas}$  for LQ AlMg (12.8 at% Mg) aged at room temperature as a function of ageing time  $t$ .

**f.** Enthalpy change for GP-zone dissolution,  $\Delta H_{meas}$ , in LQ AlMg (12.0 at% Mg) aged at 333 K as a function of ageing time  $t$ .

**g.** Enthalpy change for GP-zone dissolution,  $\Delta H_{meas}$ , for LQ-alloy (15.9 - 17.2 at% Mg) as a function of ageing time at room temperature, 313 K, 333 K and 353 K. (Presentation of curves only; for data see Figures 7(a) to (d)).



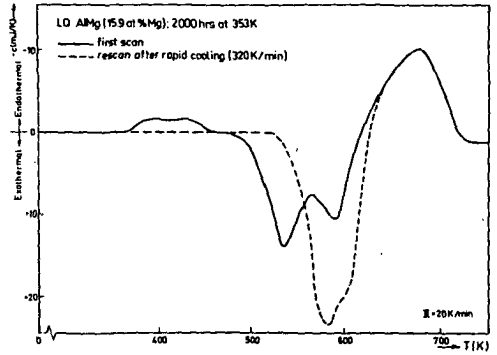
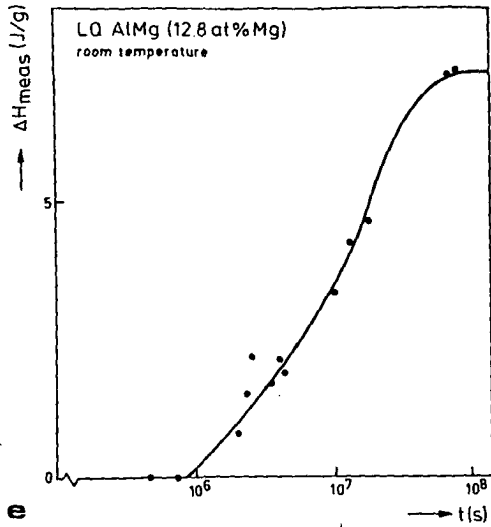


**Fig. 8.**  
DSC scan and rescan of LQ AlMg (15.9 at% Mg) aged for 2000 h at 353 K (specimen weight 12.360 mg).

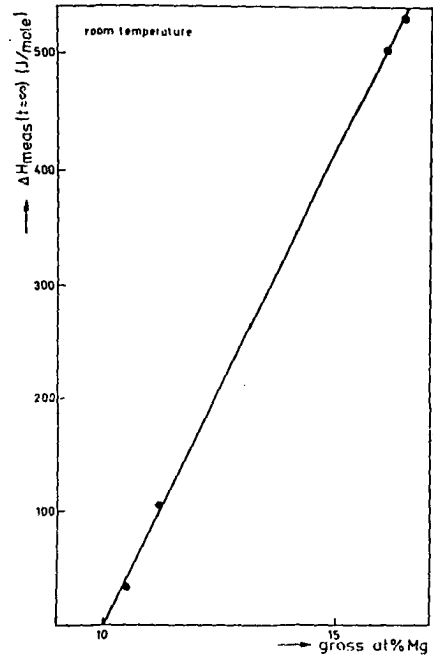
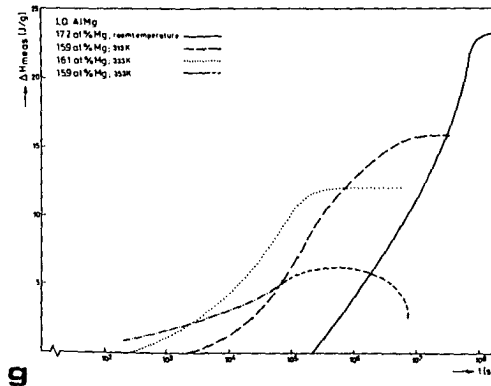
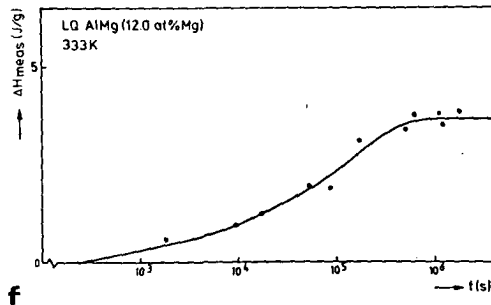


**Fig. 9.**  
Enthalpy change for GP-zone dissolution of LQ AlMg alloys fully aged at room temperature,  $\Delta H_{meas}(t = \infty)$ , as a function of gross magnesium content (completely dissolved initially).

heat effect occurs (Figures 7(a) through (c), (e) and (f)) a stable position for the GP-zone solvus is reached.

## 6. Enthalpy of formation of GP-zones

The dissolution process of the GP-zones can be described as:



where  $\alpha$  and  $\alpha'$  indicate the AlMg solid solution before and after GP-zone dissolution, respectively. The mass balance of this reaction can be expressed as:

$$\left(\frac{z-x}{z-y}\right)\alpha + \left(\frac{x-y}{z-y}\right)\text{GP} = \alpha' \quad (2)$$

where the atom fractions  $x$ ,  $y$  and  $z$  indicate the magnesium contents of  $\alpha'$ ,  $\alpha$  and GP. Then, the enthalpy change corresponding to this reaction and as measured by DSC,  $\Delta H_{\text{meas}}(t = \infty)$ , can be written as:

$$\Delta H_{\text{meas}}(t = \infty) = H_{\alpha'} - \left(\frac{z-x}{z-y}\right)H_{\alpha} - \left(\frac{x-y}{z-y}\right)H_{\text{GP}} \quad (3)$$

where  $H_{\alpha'}$ ,  $H_{\alpha}$  and  $H_{\text{GP}}$  denote the enthalpy per mole  $\alpha'$ ,  $\alpha$  and GP respectively.

Adopting the (modified) regular solution model (see Appendix) for the enthalpy of mixing, it follows:

$$H_{\alpha'} = \Omega x(1-x) + (1-x)H_{\text{Al}} + xH_{\text{Mg}} \quad (4)$$

$$H_{\alpha} = \Omega y(1-y) + (1-y)H_{\text{Al}} + yH_{\text{Mg}} \quad (5)$$

where  $H_{\text{Al}}$  and  $H_{\text{Mg}}$  are the enthalpies of Al and Mg respectively and  $\Omega$  is the interaction parameter. According to the definition for the enthalpy of formation of GP-zones,  $\Delta H_{\text{GP}}$ , it holds:

$$H_{\text{GP}} = \Delta H_{\text{GP}} + (1-z)H_{\text{Al}} + zH_{\text{Mg}} \quad (6)$$

At standard temperature and standard pressure  $H_{\text{Al}}$  and  $H_{\text{Mg}}$  are taken equal to zero and  $H_{\text{GP}} = \Delta H_{\text{GP}}$ .

After substitution of eqs. (4) through (6) into eq. (3) the enthalpy of formation of the GP-zones is obtained as:

$$\Delta H_{\text{GP}} = \left(\frac{z-y}{x-y}\right)\Omega x(1-x) - \left(\frac{z-x}{x-y}\right)\Omega y(1-y) - \left(\frac{z-y}{x-y}\right)\Delta H_{\text{meas}}(t = \infty) \quad (7)$$

A linear relation between  $\Delta H_{\text{meas}}(t = \infty)$  (= negative of the heat of dissolution of GP-zones) and  $x$  was found experimentally such that  $\Delta H_{\text{meas}}(t = \infty)/(x-y) = \text{constant} \equiv c$  (Figure 9). Then Eq. (7) can be rewritten as:

$$\Delta H_{\text{GP}}(x) = \Omega(y-z)x + C \quad (8)$$

with  $C = \Omega z(1-y) - (z-y)c$ .

The interaction parameter  $\Omega$  is only slightly dependent on composition and temperature (see Appendix). Hence, the enthalpy of formation of GP-zones is a linear function of the gross magnesium content dissolved.

For the temperature range where the dissolution occurs (peak temperature of the heat effect at about 368 K) it follows for  $\Omega$ : 14.4 kJ/mole (see Appendix). A reasonable estimate for the GP-zone composition,  $z$ , appears to be: 0.25<sup>[4,5]</sup>. Further,  $y$  and  $c$  follow from Figure 9. Finally, it is obtained for the enthalpy of formation of GP-zones:

$$\Delta H_{\text{GP}}(x) = -2160x + 1932 \text{ J/mole} \quad (9)$$

In principle, this enthalpy of formation holds at the dissolution temperature (~368 K). However, if the rule of Kopp and Neumann is valid (i.e. the heat capacity of GP is equal to the atomic-fraction weighted average of those of Al and Mg) this enthalpy of formation also corresponds to that at the temperature of ageing (room temperature). On increasing  $x$  the instability of the GP-zones, as indicated by  $\Delta H_{\text{GP}}$ , decreases ( $\Delta H_{\text{GP}}$  becomes less positive, whereas the instability of the solid solution, as indicated

by the enthalpy of mixing ( $= \Omega x(1-x)$ ), increases ( $\Omega$  is positive;  $x < 0.5$ ).

## 7. The kinetics of formation and dissolution of GP-zones

### 7.1. Isothermal ageing: formation of GP-zones

The formation of GP-zones can be traced by measuring the fraction formed as a function of ageing time. To this end the fraction formed,  $f$ , is expressed as

$$f(t) = \frac{\Delta H_{\text{meas}}(t)}{\Delta H_{\text{meas}}(t=\infty)} \quad (10)$$

where  $-\Delta H_{\text{meas}}(t)$  and  $-\Delta H_{\text{meas}}(t=\infty)$  are the heats of dissolution after ageing times  $t$  and  $\infty$ , respectively. Experimental data for  $\Delta H_{\text{meas}}(t)$  are presented in Figures 7(a) to (f).

It will be assumed that the fraction  $f$  is fully determined by the state variable  $\beta$ :

$$\beta = kt = k_0 t \exp(-Q/RT) \quad (11)$$

where  $Q$  is the activation energy and  $k_0$ ,  $R$  and  $T$  denote the pre-exponential factor, the gas constant and the absolute temperature respectively. Without recourse to any specific kinetic model a value for the activation energy can be obtained from the ageing times,  $t_1$  and  $t_2$ , corresponding to two fixed stages of transformation,  $f_1$  and  $f_2$ , measured at a number of temperatures. It follows

$$k(t_{f_2} - t_{f_1}) = \beta_{f_2} - \beta_{f_1} = \text{constant and thus}^{[27]}:$$

$$\ln(t_{f_2} - t_{f_1}) = \frac{Q}{RT} + \text{constant} \quad (12)$$

Hence, the activation energy can be derived from the slope of the straight line obtained by plotting  $\ln(t_{f_2} - t_{f_1})$  versus  $1/T$ .

Application of the above procedure to the experimental data obtained for the LQ AlMg-alloys containing about 16 at% Mg (Figures 7a-c) yields the following results:

$f_1 = 0.2$  and  $f_2 = 0.5$ ;  $Q = 133$  kJ/mole;  
regression coefficient = 0.973.

$f_1 = 0.5$  and  $f_2 = 0.8$ ;  $Q = 136$  kJ/mole;  
regression coefficient = 0.997.

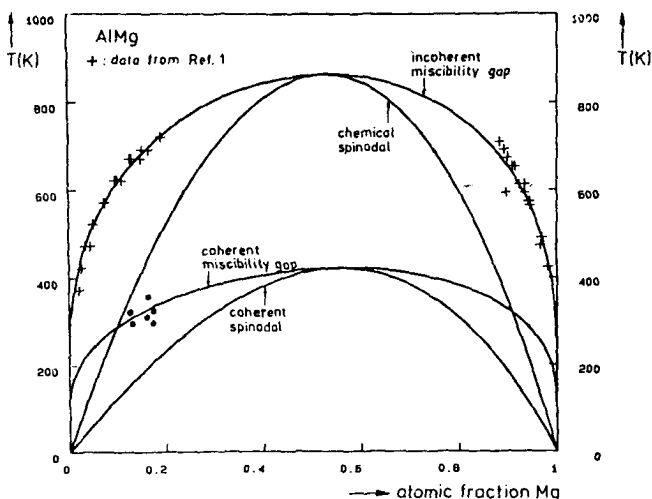


**Fig. 10.**

Calculated (metastable) phase diagram for the AlMg-system (see Appendix). The symbol + indicates alloys investigated.

According to literature data<sup>[25]</sup> the activation energy for volume diffusion of magnesium in aluminium equals about 130 kJ/mole. The distances which could be covered by volume diffusion of magnesium are much too small to bring about appreciable GP-zone precipitation at the ageing temperatures applied (for example, adopting  $x^2 = 2tD_0 \exp(-Q/RT)$ , where  $x$  and  $D_0$  denote "diffusion distance" and pre-exponential factor respectively, it follows with  $D_0 = 1 \text{ cm}^2/\text{s}$ ,  $Q = 130 \text{ kJ/mole}$ ,  $T = 295 \text{ K}$  and  $t = 10^6 \text{ s}$  (see Figure 7(a)):  $x = 4 \cdot 10^{-2} \text{ nm}$ ). In accordance with the results and the discussion presented in section 4 it can be expected that quenched-in excess vacancies facilitate the diffusion of magnesium atoms, in particular at the start of ageing. This would be associated with a (minimal) activation energy equal to about that for migration of vacancies in aluminium ( $\cong 60 \text{ kJ/mole}$ <sup>[26]</sup>). Hence, it is concluded that the nucleation of GP-zones corresponds with a significant contribution to the effective activation energy operative at the ageing temperatures applied.

7.2. *Nonisothermal annealing of aged alloys: dissolution of GP-zones; comparison of liquid-quenched and solid-quenched alloys*

Adopting JMA-kinetics, it has been shown that for a series of experiments, each with its own constant heating rate  $\Phi$ , it holds<sup>[13, 27]</sup>:

$$\ln\left(\frac{T_i^2}{\Phi}\right) = \frac{Q}{RT_i} + \text{constant} \quad (13)$$

where  $T_i$  denotes the temperature where an inflection point occurs on the curve of  $f$  versus  $T (+t)$ , i.e. the temperature where the maximal transformation rate is experienced during annealing. Hence, the activation energy can be determined from the slope of the straight line obtained on plotting  $\ln\left(\frac{T_i^2}{\Phi}\right)$  versus  $\frac{1}{T_i}$ . If the nonisothermal

annealing with constant heating rate is performed in a DSC-apparatus the temperature corresponding to the peak of the heat effect can be taken as an estimate for  $T_i$ . The error made is usually small and, furthermore, a correction can be calculated<sup>[28]</sup>.

A series of experiments was devised to assess the effect of the quenching procedure and the ageing treatment on the kinetics of dissolution of the GP-zones, as exhibited in the activation energy determined on the basis of eq. (13). The results obtained for AlMg (16-17 at% Mg) can be summarized *in order of increasing activation energy* as follows:

(i) SQ (from 723 K); aged for 0.5 h at room temperature.

$Q = 70 \text{ kJ/mole}$ ; regression coefficient = 0.997.

(ii) LQ; aged at room temperature (for all times investigated up to two years).

$Q = 92 \text{ kJ/mole}$ ; regression coefficient = 0.999.

(iii) SQ (from 423 K); aged for 360 h at room temperature.

$Q = 92 \text{ kJ/mole}$ ; regression coefficient = 0.994.

(iv) LQ; aged for 21 h at 333 K.

$Q = 110 \text{ kJ/mole}$ ; regression coefficient = 0.991.

(v) LQ; aged for 1 h at 423 K in the DSC-apparatus, slowly cooled (20 K/min) to 333 K followed by ageing at that temperature for 18 h.

$Q = 133 \text{ kJ/mole}$ ; regression coefficient = 0.997.

The above result for experiment (i) forcefully suggests that the amount of quenched-in excess vacancies, facilitating GP-zone dissolution, was much larger after the present, drastic, method of solid quenching than after liquid quenching by melt spinning (implying that diffusion of magnesium is rate determining for the GP-zone dissolution). This is fully consistent with results discussed in section 4.2. where a possible explanation has been proposed too. In this context it is striking to see that the experiment where the equilibrium concentration of vacancies at the considered ageing temperature has probably been attained most nearly (experiment (v)), yields an activation energy approximately equal to that reported for volume diffusion of magnesium in aluminium (about 130 kJ/mole<sup>[25]</sup>), as could be expected. As a consequence the amount of vacancies in the specimens investigated is thought to decrease in the order (i) → (v) given above.

It should be realized that the activation energy for formation of GP-zones is not equal to that for dissolution of GP-zones: nucleation contributes to the activation energy found for GP-zone formation (see section 7.1.).

Apart from vacancy annihilation at permanent sinks as grain boundaries, significant condensation of vacancies leading to vacancy loops occurred during cooling after rapid solidification by melt spinning and on ageing (see also section 4.2.). The relatively small values for the activation energy reported above for the dissolution of GP-zones in LQ-alloys (see experiments (ii) and (iv)) could then be ascribed to emitting of vacancies by such vacancy loops, because, the dissolution occurs at a relatively high temperature (370-380 K; see section 4.1.), where the loops become unstable. Thus, the vacancy loops are conceived as temporary sinks<sup>[29]</sup>; see also Reference 10.

## 8. Conclusions

(i) All results obtained in the present work on annealing AlMg-alloys, quenched and aged at temperatures below 353 K, are consistent with the following precipitation model:

(a) on ageing clustering of dissolved magnesium atoms (GP-zone formation) and of vacancies (*void/loop formation*) occurs;

(b) on subsequent annealing the GP-zones dissolve before  $\beta'/\beta$  precipitates develop; the  $\beta'/\beta$  particles can nucleate at structural heterogeneities as grain boundaries and vacancy voids/loops which are more stable than the GP-zones.

(ii) On ageing GP-zone formation (*homogeneous nucleation*) proceeds more rapidly in SQ-alloys than in LQ-alloys because of the larger amount of excess vacancies retained after (drastic) SQ than after LQ (melt spinning).

(iii) On annealing  $\beta'/\beta$  precipitation (*heterogeneous nucleation*) starts at a lower temperature in LQ-alloys than in SQ-alloys because of the larger amount of structural heterogeneities (grain-boundary area) in LQ-alloys.

(iv) From the dependence on magnesium content of the heat of dissolution of GP-zones for alloys fully aged at room temperature it follows that at least 10 at% Mg should be dissolved in order that GP-zones form at room temperature. This leads to an estimate for the GP-zone solvus by adopting established models for the chemical and strain contributions to the free enthalpy of mixing.

(v) Quantitative analysis of the heat of dissolution of GP-zones and applying a modified regular solution model for the free enthalpy of mixing, indicates that the enthalpy of formation of GP-zones depends linearly on gross magnesium atomic fraction,  $x$ , ( $\Delta H_{GP}(x) = -2160 \cdot x + 1932$  J/mole).

(vi) The kinetics of the formation of the GP-zones are governed by the process of

nucleation and excess-vacancy enhanced diffusion of magnesium.

(vii) The kinetics of the dissolution of the GP-zones are governed by diffusion of magnesium. Values found for the activation energy are smaller than those for volume diffusion of magnesium. This can be explained by emitting of vacancies from vacancy voids/loops, which become unstable at the temperatures where the GP-zones dissolve.

(viii) Values obtained for the activation energy of GP-zone dissolution in SQ-alloys are significantly smaller than those for LQ-alloys. This indicates that the amount of excess vacancies retained after SQ (whether or not in condensed state) is larger than after LQ, in agreement with conclusion (ii).

### Acknowledgements

The authors are indebted to Professor B.M. Korevaar for critically reading the manuscript and stimulating discussions and to Ir. P. van Mourik for X-ray diffraction lattice parameter determinations. Financial support by the Foundation for Fundamental Research of Matter (FOM) is gratefully acknowledged.

### Appendix: Coherent phase diagram of AlMg

The chemical free enthalpy of mixing,  $G_{\text{mix}}^{\text{chem}}$ , of a solid solution can be described by the following expression<sup>[21]</sup> (based on a regular solution model for the enthalpy of mixing, but with a composition and temperature dependent interaction parameter, and Gibb's expression for the entropy of mixing):

$$G_{\text{mix}}^{\text{chem}} = (a + bx - cT)x(1-x) + RT\{x \ln x + (1-x) \ln(1-x)\}$$

(A-1)

where  $x$  = atomic fraction of solute,  $T$  = absolute temperature and  $R$  = gas constant. Values for the constants  $a$ ,  $b$  and  $c$  can be determined from two (known) isothermal sections of the incoherent AlMg phase diagram. Data for the solvus at the Al-rich side and that at the Mg-rich side are given in Reference 1. It was derived:

$$a = 14590 \text{ J/mol}; b = 1104 \text{ J/mol}; c = 0.9364 \text{ J/mol K.}$$

Both the chemical binodal ("incoherent miscibility gap") and the chemical spinodal can be calculated, applying the common tangent construction and

$$\frac{\partial^2 G_{\text{mix}}^{\text{chem}}}{\partial x^2} = 0, \text{ respectively.}$$

For construction of the coherent binodal ("coherent miscibility gap") and the coherent spinodal the expression for the free enthalpy of mixing must be extended with a strain-energy term (approaching equilibrium the gradient-energy contribution becomes negligible, implying decomposition with composition fluctuations of "infinite wavelength"). Then, the coherent free enthalpy of mixing,  $G_{\text{mix}}^{\text{coh}}$ , can be given as<sup>[22]</sup>:

$$G_{mix}^{coh} = G_{mix}^{chem} + \eta^2 E^2 (x-x_0)^2 V_m \quad (A-2)$$

where  $\eta$  = fractional change of lattice parameter per unit composition change,  $E' = E/(1-\nu)$  with  $E$  and  $\nu$  as Young's modulus and Poisson's ratio, respectively.  $V_m$  is the molar volume and  $x_0$  is the composition of the homogeneous alloy considered. Note that eq. (A-2) implies that, on analysing decomposition behaviour, the dependence of  $G_{mix}^{coh}$  on  $x$  changes if the gross content  $x_0$  changes.

The construction of the coherent binodal can occur in principle by application of the common tangent rule to  $G_{mix}^{coh}$ . The compositions thus found for the coherent binodal are unchanged if a constant term and a term linear in  $x$  are added to  $G_{mix}^{coh}$  according to eq. (A-2). Therefore the common tangent rule can equally be applied to:

$$(G_{mix}^{coh} = G(x) + \eta^2 E^2 V_m x^2 \quad (A-3)$$

implying that, in contrast to the coherent free enthalpy of mixing, the location of the coherent binodal does not depend on gross content  $x_0$  of the solute in the alloy.

The coherent spinodal follows from:

$$\frac{\partial^2 G_{mix}^{coh}}{\partial x^2} = -2\eta^2 E^2 V_m \quad (A-4)$$

Values for  $\eta$ ,  $V_m$  and  $\nu$  were derived from References 1 and 23:

$$\begin{aligned} \eta &= 0.11051 \\ V_m &= 9.993 \times 10^{-6} \text{ m}^3 \\ \nu &= 0.345 \end{aligned}$$

For the value of Young's modulus used see discussion in section 4. The resulting coherent and incoherent binodals and spinodals are shown in Figure 10.

## References

1. J.L. Murray, Bull. Alloy Phasediagram 3 (1982) 60-74.
2. W.A. Pollard, J. Inst. Met. 93 (1964-65) 339-346.
3. M. Roth and J.M. Raynal, J. Appl. Cryst. 7 (1974) 219-221.
4. K. Osamura and T. Ogura, Met Trans. 15A (1984) 835-842.
5. R. Nozato and S. Ishihara, Trans. Jpn. Inst. Met. 21 (1980) 580-588.
6. A. Dager, E.K. Boudili and M. Roth, Scripta Met. 10 (1976) 1119-1124.
7. E.K. Boudili, M.F. Denanot and A. Dager, Scripta Met. 11 (1977) 543-548.
8. P. van Mourik, Th.H. de Keijser and E.J. Mittemeijer, Proc. Int. Conf. on Rapidly Solidified Materials, San Diego, California, USA, February 3-5, 1986, P.W. Lee and R.S. Carbonara (eds.), p. 341-350.
9. S.C. Agarwal and H. Herman, Aluminium 54 (1978) 257-260.
10. P. van Mourik, E.J. Mittemeijer and Th.H. de Keijser, J. Mater. Sci. 18 (1983) 2706-2720.
11. F. Thoyama, H. Okuda, K. Osamura and H. Shingu, Proc. 91st Annual Meeting of Japan Inst. Metals, 1982, Z. Yamamoto (ed.), p. 145.
12. M. van Rooyen, J.A. van der Hoeven, L. Katgerman, P. van Mourik, Th.H. de Keijser and E.J. Mittemeijer, in Proc. of the P.M.-Aerospace Mater. Conf., Berne (Switzerland), November 1984, Vol. 1, edited by Metal Powder Report, p. 34-1-16.
13. L.V. Meisel and P.J. Cote, Acta Met. 31 (1983) 1053-1059.
14. D. Dollimore, The State of the Art of Thermal Analysis, O. Menis, H. Rook and P.D. Garn, eds., Nat. Bur. Stand. (U.S.), Spec. publ. 580, U.S. Government Printing Office, Washington, DC, 1980, p. 1-31.

15. J.M. Papazian, *Met. Trans.* 13A (1982) 761-769.
16. Z. Katz and N. Ryum, *Scripta Met.* 15 (1981) 265-268.
17. M. Bernole, J. Raynal and R. Graf, *J. Microscopie* 8 (1969) 831-840.
18. G.W. Lorimer and R.B. Nicholson, *Acta Met.* 14 (1966) 1009-1013.
19. M. van Rooyen, N.M. van der Pers, L. Katgerman, Th.H. de Keijser and E.J. Mittemeijer, in "Proc. 5th Int. Conf. Rap. Quenched Metals", Würzburg (West Germany), September 3-7, 1984, S. Steeb and H. Warlimont (eds.), p. 823-826.
20. J.H. Driver and J.M. Papazian, *Mater. Sci. and Eng.* 76 (1985) 51-56.
21. M. Hillert, *J. Physique Radium* 23 (1962) 835-840.
22. J.W. Cahn, *Acta Met.* 10 (1962) 907-913.
23. C.J. Smithells (ed.), *Metals Reference Book*, 5th edition, Butterworths, London, 1976, 977.
24. L.F. Mondolfo, *Aluminium Alloys: Structure and Properties*, Butterworths, London, 1976, p. 314.
25. M. Bishop and K.E. Fletcher, *Int. Met. Rev.* 17 (1972) 203-225.
26. W. De Sorbo and D. Turnbull, *Acta Met.* 7 (1959) 83-85.
27. E.J. Mittemeijer, C. Liu, P.J. van der Schaaf, C.M. Brakman and B.M. Korevaar, *Met. Trans. A*, in press.
28. E.J. Mittemeijer, A. van Gent and P.J. van der Schaaf, *Met. Trans.* 17A (1986) 1441-1445.
29. E. Ozawa and H. Kimura, *Acta Met.* 18 (1970) 995-1004.

# PRECIPITATION OF SILICON IN ALUMINIUM-SILICON; A CALORIMETRIC ANALYSIS OF LIQUID-QUENCHED AND SOLID-QUENCHED ALLOYS

M. van Rooyen and E.J. Mittemeijer

Laboratory of Metallurgy, Delft University of Technology,  
Rotterdamseweg 137, 2628 AL Delft, The Netherlands

A calorimetric analysis of silicon precipitation in liquid-quenched (LQ; rapidly solidified) and solid-quenched (SQ; quenched after annealing the solid at elevated temperature) AlSi alloys was made. Nonisothermal annealing (with constant heating rate) experiments (differential scanning calorimetry) were performed using specimens of various gross silicon contents (1.3-19.1 at% Si). Initial and resulting microstructures were characterized by X-ray diffraction and transmission electron microscopy. Quantitative analysis showed that heat production in LQ alloys is due to precipitation of dissolved silicon and coarsening of silicon particles already present in the as liquid-quenched state, whereas heat production in SQ alloys can be solely ascribed to precipitation. The kinetics of silicon precipitation are affected by the presence of quenched-in excess vacancies (both LQ and SQ alloys). The solidification start temperature and the amount of grain-boundary area as a function of gross silicon content are discussed in terms of their effect on vacancy annihilation and the resulting effective activation energy.

## 1. Introduction

By rapid solidification solid solubilities and vacancy concentrations larger than the equilibrium ones can be achieved, in association with a very fine micro(grain)structure<sup>[1]</sup>. Such effects have been observed for AlSi alloys<sup>[2-4]</sup>; also the composition where a completely eutectic solidification occurs shifts to a higher silicon content<sup>[3]</sup>.

Consequently, the precipitation behaviour of alloys quenched from the melt (liquid quenching) can be quite different from that of

alloys quenched in the solid state after an anneal at elevated temperature (solid quenching). Only a relatively small number of investigations has been devoted to precipitation processes in LQ Al-base alloys, for example see References 4-6; in particular analyses of changes in energy (enthalpy; calorimetry) are rare (see References 7 and 8).

For the study of precipitation in Al-base alloys, the AlSi and AlMg systems provide two extremes. In the case of AlSi alloys a direct

precipitation of silicon from the supersaturated solid solution takes place, whereas decomposition in AlMg alloys proceeds via preprecipitates (Guinier-Preston zones) and intermediate precipitates. In a previous study<sup>[9]</sup> the precipitation behaviour of both liquid-quenched (LQ) and solid-quenched (SQ) AlMg-alloys was analysed employing differential scanning calorimetry (DSC); striking differences between LQ and SQ alloys were observed. The purpose of this paper is to present a quantitative analysis of the heat production and the kinetics of processes occurring on precipitation in both LQ and SQ AlSi-alloys.

## 2. Experimental procedure

### 2.1. Sample preparation

Liquid-quenched (LQ) AlSi-alloys containing 1.3, 4.4, 7.2, 11.4, 13.9 and 19.1 at% Si were prepared by melt-spinning (for a detailed description see Reference 10). Solid-quenched (SQ) material was obtained by annealing melt-spun ribbons of the indicated compositions in a hydrogen atmosphere (flow rate 40.7 cm/min) during 5 minutes at 823 K succeeded by quenching in ice water.

The gross silicon content of the alloys was determined by chemical analysis (gravimetry). The amount of silicon in solid solution in the Al-rich phase was derived from the lattice parameter of the Al-rich phase<sup>[2]</sup> as determined by X-ray diffraction analysis (Debye-Scherrer photographs<sup>[5]</sup>).

### 2.2. Differential Scanning Calorimetry (DSC)

The calorimetric analysis was performed with a differential scanning calorimeter (Dupont, type DSC 910). Both the sample pan and the reference pan were made of aluminium. The sample pan was filled with chopped ribbons and subsequently sealed with an aluminium cover. The reference pan was

provided with two aluminium covers in order to obtain a heat capacity comparable with that of the sample. A protective gas atmosphere of pure argon was employed (gas flow: 50 ml/min).

For determination of the heat production and the activation energy of the precipitation process a series of experiments with heating rates of 2.5, 5, 10, 20, 30 and 40 K/min were performed.

Per sample two DSC-runs were performed successively; the second run was carried out in order to obtain the baseline (cf. section 4.1).

### 2.3. Transmission Electron Microscopy (TEM)

Thin electron-transparent regions of the ribbons (in both the LQ and SQ conditions; cf. section 2.1.) were investigated using a Philips EM 400 electron microscope. In order to analyse the growth of second-phase particles during the nonisothermal annealing with constant heating rate, specimens of LQ AlSi were annealed up to the temperature where the exothermic peak has been completed in the DSC scan and thereafter quenched.

## 3. The amount of dissolved silicon after solid and liquid quenching

The amount of silicon dissolved in the Al-rich phase after solid quenching can be read from the solvus of the Al-rich phase in the equilibrium AlSi phase diagram<sup>[11]</sup> at the quench temperature. Obviously the content of dissolved silicon does not depend on the gross silicon content of the AlSi alloy.

An opposite behaviour is found for the AlSi alloys after liquid quenching; the amount of silicon dissolved in the Al-rich phase depends on the gross silicon content of the alloy (Fig. 1 and Table 1; based on lattice-parameter data recorded from the present LQ AlSi alloys; see also Reference 5). A maximum solid solubility occurs at a gross silicon content of 13-14 at%. This agrees with our earlier data for LQ AlSi

alloys<sup>[2]</sup> and can be interpreted as a result of a metastable extension on liquid quenching of the liquid-solid two-phase region towards lower temperatures for the Al-rich side of the AlSi-phase diagram, leading to a metastable eutectic at 13-14 at% Si (see also Reference 3).

z (at% Si)	x (at% Si)
1.3	0.9
4.4	1.4
7.2	2.5
11.4	3.3
13.9	3.3
19.1	2.9

**Table 1**

Gross silicon content,  $z$ , and composition,  $x$ , of the Al-rich phase of the investigated LQ AlSi alloys. The composition of the Al-rich phase of the SQ AlSi alloys after quenching from 823 K was 1.25 at% Si.

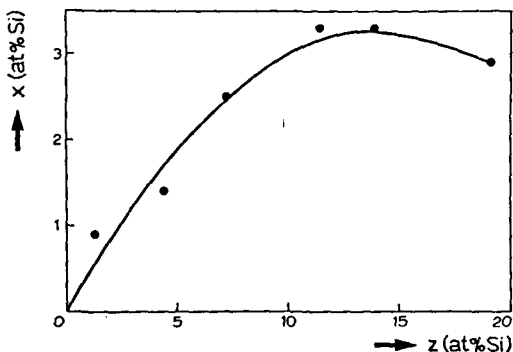


**Figure 1.**

The composition of the Al-rich phase,  $x$ , as a function of the gross silicon content,  $z$ , of LQ AlSi-alloys.

## 4. Heat effects

### 4.1. General description

On heating a SQ or LQ AlSi specimen the silicon initially dissolved in the Al-rich matrix precipitates.

The exothermic peak observed in a DSC scan of a SQ AlSi (2.3 at% Si) specimen in the temperature range 400-630 K (Fig. 2; 20 K/min) is due to this precipitation process. On continued heating an endothermic effect is observed for temperatures larger than about 650 K; this consumption of heat can be ascribed to the dissolution of silicon particles (cf. the phase diagram for AlSi<sup>[11]</sup>).

After the (first) DSC scan has been completed ( $T = 823$  K), the specimen is slowly cooled to room temperature (with about 10 K/min) and all silicon precipitates (again; at room temperature the equilibrium solid solubility of silicon in aluminium is negligible<sup>[11]</sup>). Then a second DSC scan will obviously not show the exothermic effect (due to silicon precipitation) but only the endothermic effect (due to silicon dissolution). Because in this work only the

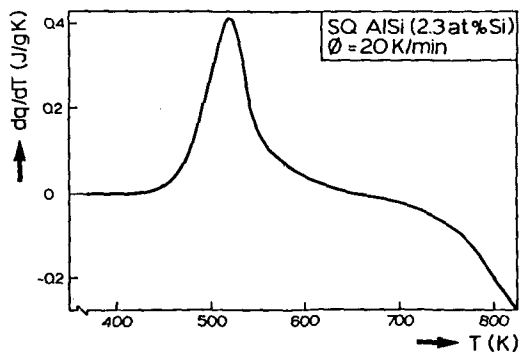


**Figure 2.**

DSC scan (rate of heat generation,  $dq/dT$  (per unit of mass and per degree Kelvin), versus temperature) of SQ AlSi (2.3 at% Si).

precipitation process is analysed, net calorimetric curves are shown (apart from the one in the above discussed Fig. 2) as obtained by removing the endothermic effect employing the second (= re)scan for base-line construction.

In the DSC scans of the LQ AlSi alloys a second exothermic effect, immediately following and overlapping with the first, exothermic, precipitation effect, was discerned, in particular for relatively large gross contents of silicon: see the DSC curve in Fig. 4b for LQ AlSi (11.4 at% Si). This heat production is ascribed to coarsening of the silicon particles: in the LQ AlSi alloys the major part of the silicon is usually not dissolved in the Al-rich matrix immediately after LQ (cf. Table 1), but is present as very small silicon particles (Fig. 6a). The occurrence of coarsening during precipitation is illustrated by a comparison of silicon particle size before annealing and just after annealing up to the temperature where the exothermic peak has been completed in the DSC scan (~ 630 K) (Figs. 3a and b; TEM micrographs; note the difference in magnification between the micrographs); for the example shown the decrease of Si/Al-rich matrix interfacial area is about 80%. This interpretation will be substantiated by quantitative analysis of the total heat production (see section 5.2).

#### 4.2. Liquid quenching versus solid quenching

DSC curves obtained from LQ and SQ AlSi alloys can be compared in Figs. 4a and 4b for gross silicon contents of 1.3 and 11.4 at%, respectively.

The shape and temperature range of the exothermic effect did not depend significantly on gross silicon content for the SQ alloys. This can be understood realizing that for specimens prepared by SQ from the same annealing temperature the amount of silicon dissolved in the Al-rich matrix is independent of gross silicon content, implying a constant supersaturation (related to the driving force



**Figure 3a.**

Transmission electron micrograph (bright field) of LQ AlSi (7.2 at% Si)-ribbon. As liquid-quenched condition.



**Figure 3b.**

Transmission electron micrograph (bright field) of LQ AlSi (7.2 at% Si) ribbon. After DSC run (heating rate 20 K/min) from 303 up to 630 K. (Note difference in magnification between Figs. 3a and b).

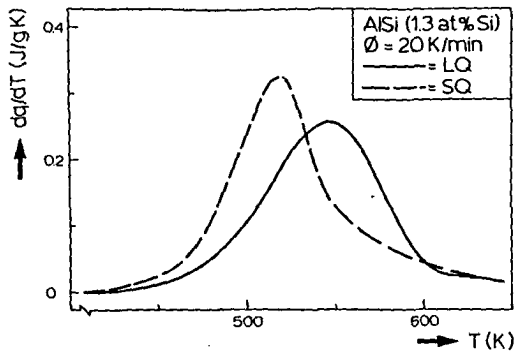


**Figure 4a.**  
DSC scan of both LQ and SQ AlSi (1.3 at% Si).

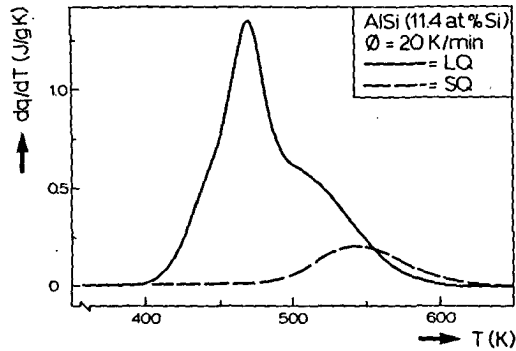


**Figure 4b.**  
DSC scan of both LQ and SQ AlSi (11.4 at% Si).

for precipitation) and a constant heat production per mole Al-rich phase due to precipitation.

The amount of silicon dissolved in LQ AlSi alloys is in general larger than in SQ AlSi alloys (especially for gross silicon contents larger than the maximal amount of silicon dissolvable in equilibrium: 1.58 at% Si at 850 K<sup>(11)</sup>; see Table 1 and Section 3). Therefore the heat effect can be much larger for LQ alloys than for SQ alloys (see Fig. 4b). Since the driving force for precipitation can then be larger for LQ alloys, due to the larger supersaturation, the heat production starts at

lower temperatures in the DSC scan (see Fig. 4b). This is consistent with the observation that the peak temperature of the heat effect for the LQ alloys decreases for an increasing amount of dissolved silicon (Fig. 5). In this context it is noted that for the AlSi alloys with a gross silicon content of 1.3 at% the amount of silicon dissolved in the Al-rich matrix is larger for the SQ alloy than for the LQ alloy (1.25 at% Si vs. 0.9 at% Si; cf. Table 1), which, in accordance with the above discussion, implies that for this particular case silicon precipitation on heating starts at a lower temperature for the SQ alloy (see Fig. 4a).

As demonstrated by TEM micrographs the silicon particles present in the as-quenched LQ alloys are very much smaller than the silicon particles in the SQ alloys (cf. Figs. 6a and 6b): sizes of the order of 1 nm vs. sizes of the order of 1  $\mu$ m. The size of the silicon particles in the SQ alloys is determined by the annealing during 5 min at 823 K before SQ (cf. section 2.1.). The size of the silicon particles in the LQ

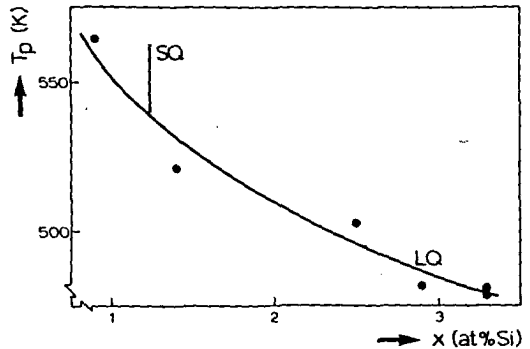


**Figure 5.**  
Peak temperature of the exothermic peak,  $T_p$ , as a function of the composition of the Al-rich phase of the LQ AlSi alloys,  $x$ , for a constant heating rate (40 K/min). The exothermic peak temperature for the SQ AlSi alloys has been indicated by the vertical bar.

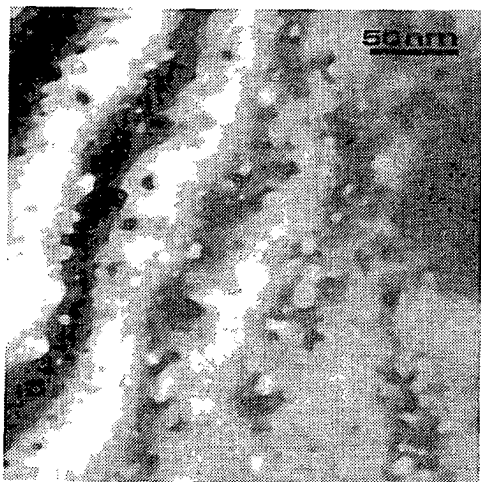


**Figure 6a.**  
Transmission electron micrograph (bright field) of LQ AlSi (11.4 at% Si) ribbon. As liquid-quenched condition.

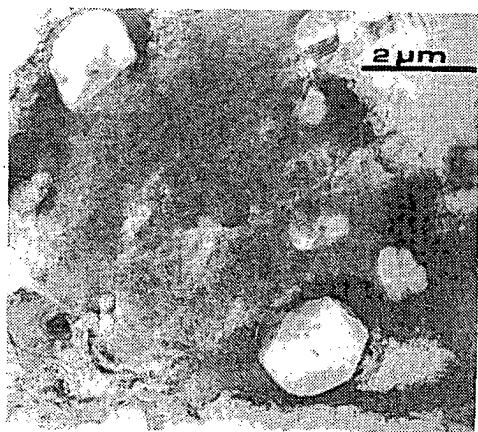


**Figure 6b.**  
Transmission electron micrograph (bright field) of SQ AlSi (11.4 at% Si). As solid-quenched condition. (Note the difference in magnification between Figs. 6a and b).

alloys is very small because these particles develop during rapid solidification (LQ is initially related with a cooling rate of about  $10^6$  K/s<sup>[12]</sup>) or precipitate during the cooling

immediately after the solidification (indications exist that a relatively slow cooling rate occurs in the low temperature region of the quench<sup>[9]</sup>). It may then be anticipated that for the LQ alloys significant reduction of Gibbs free energy results by coarsening of the silicon particles (see quantitative data in section 5.2). The side maximum at the high-temperature side of the total exothermic peak of, for example, the LQ AlSi (11.4 at% Si) alloy (Fig. 4b) may be thus explained. For smaller gross contents of silicon the effect will be less distinctly visible in a DSC scan because (i) the precipitation process occurs at a higher temperature range (due to a smaller supersaturation; see above discussion) and (ii) less silicon particles are present in the as-quenched condition in proportion to the silicon content dissolved in the Al-rich matrix (see Table 1): cf. the DSC curves for the LQ alloys in Figs. 4a and 4b.

## 5. Heats of precipitation and coarsening

### 5.1. Precipitation (SQ alloys)

The heat produced in the temperature range 400-630 K (exothermic peak in the DSC scan) can be expressed as the heat produced,  $Q_{Al_{1-x}Si_x}$  on precipitation of silicon in one mole of the Al-rich phase with an initially dissolved atomic fraction  $x$  of silicon (see eq. (A-3) in the Appendix). Data obtained for  $Q_{Al_{1-x}Si_x}$  are shown as a function of  $x$  in Fig. 7 for the SQ alloys\*: it can be concluded that a linear relationship occurs, implying that for the SQ

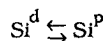
\* To determine the relationship between  $Q_{Al_{1-x}Si_x}$  and  $x$  for the SQ alloys (Fig. 7), in addition to the SQ alloys indicated in section 2.2. (all with 1.25 at% Si in solid solution) SQ alloys were prepared from AlSi alloys with a gross content of silicon of 7.2 at% by quenching after annealing for 5 min at 723 and 793 K leading to 0.46 and 0.92 at% Si in solid solution.

alloys the heat produced during precipitation of one mole silicon,  $Q_{Si}$ , does not depend on silicon composition of the Al-rich matrix (see eq. (A-7) in the Appendix). From the value cut from the abscissa by the straight line it follows that after the reaction has been completed an atomic fraction  $y$  corresponding to about 0.15 at% Si remains dissolved in the Al-rich matrix; this value agrees well with the equilibrium value of dissolved silicon at about the end temperature of the exothermic peak: 0.17 at% Si<sup>[11]</sup>.

Applying eq. (A-7) (see Appendix), the value for the heat production in the SQ alloys on precipitation of one mole silicon,  $Q_{Si}^{SQ}$ , can be calculated from the slope of the straight line in Fig. 7:

$$Q_{Si}^{SQ} = 58 \text{ kJ/mole Si}$$

An estimate for the heat of (solely) precipitation can be derived from known data for the equilibrium solvus of the Al-rich phase, as follows. For the equilibrium constant,  $K_{Si}^{prec}$ , of



where  $Si^d$  and  $Si^p$  denote dissolved and precipitated silicon, it holds

$$K_{Si}^{prec} = \frac{a_{Si^p}}{a_{Si^d} \gamma x} = \frac{1}{\gamma x} \quad (1)$$

where  $a$  denotes activity and  $\gamma$  and  $x$  indicate the activity coefficient and composition of the Al-rich phase, and where it has been realized that the precipitated phase can be conceived as pure silicon<sup>[11]</sup> ( $a_{Si^p} = 1$ ). Further, for the small amounts of silicon dissolved in equilibrium in the Al-rich matrix, Henry's law can be applied, implying that  $\gamma$  can be taken as constant. According to chemical thermodynamics

$$RT \ln K_{Si}^{prec} = -\Delta G_{Si}^{prec} = -\Delta H_{Si}^{prec} + T\Delta S_{Si}^{prec}$$

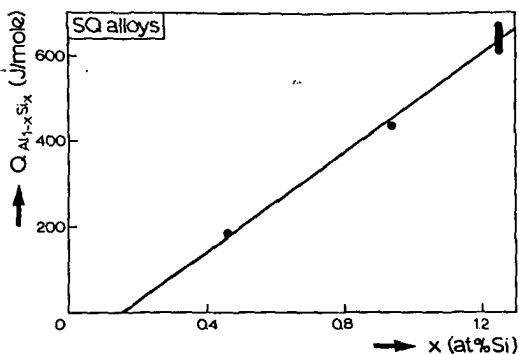


Figure 7.

The heat of silicon precipitation,  $Q_{Al_{1-x}Si_x}$  (per mole Al-rich phase), as a function of the composition of the Al-rich phase,  $x$ , for SQ AlSi alloys.

where  $\Delta G_{Si}^{prec}$ ,  $\Delta H_{Si}^{prec}$  and  $\Delta S_{Si}^{prec}$  are the changes in Gibbs free energy, enthalpy and entropy for the above precipitation reaction, and  $R$  and  $T$  are the gas constant and the absolute temperature. Then it is obtained from eq. (1) for  $K_{Si}^{prec}$

$$\ln x = \frac{\Delta H_{Si}^{prec}}{RT} - \frac{\Delta S_{Si}^{prec}}{R} - \ln \gamma \quad (2)$$

If  $\Delta H_{Si}^{prec}$ ,  $\Delta S_{Si}^{prec}$  and  $\gamma$  do not depend significantly on temperature, a plot of  $-\ln x$  versus  $1/T$  yields a straight line with slope  $-\Delta H_{Si}^{prec}/R$ . Using data from Reference 11, such a plot is shown in Fig. 8. As a result it is obtained

$$-\Delta H_{Si}^{prec} = 54 \text{ kJ/mole Si}$$

Comparing the experimental data for heat production,  $Q_{Si}^{SQ}$ , with the predicted value for the heat of precipitation,  $-\Delta H_{Si}^{prec}$ , it can be concluded that, within experimental error (see Figs. 7 and 8),  $Q_{Si}^{SQ}$  and  $-\Delta H_{Si}^{prec}$  agree well. Hence, the heat production in the SQ alloys can be ascribed entirely to precipitation of the silicon initially dissolved.

## 5.2. Precipitation and coarsening (LQ alloys)

If for the LQ alloys all heat produced in the temperature range 400-630 K would be fully attributed to precipitation of silicon from the Al-rich matrix, the heat produced per mole precipitated silicon would be approximately 60% larger than that for the SQ alloys. A comparison of the DSC curves for the LQ and the SQ alloys and the microstructural changes observed during the precipitation reaction (see section 4) suggest that this surplus in heat production for the LQ alloys may be due to the appreciable coarsening of the very small silicon particles present in the as-quenched condition.

For quantitative interpretation the heat due to the actual precipitation process has to be subtracted from the total observed heat production. Per mole alloy the heat production due to only precipitation,  $Q_{Al_{1-z}Si_z}^{prec}$ , can be obtained from the (now known; see above) heat production per mole precipitated silicon,  $Q_{Si}^{prec}$ , according to (cf. eq. (A-6) in the Appendix):

$$Q_{Al_{1-z}Si_z}^{prec} = \frac{(1-z)(x-y)}{(1-x)(1-y)} \cdot Q_{Si}^{prec} \quad (3)$$

and the surplus heat production per mole alloy,  $Q_{Al_{1-z}Si_z}^{LQ, surplus}$ , is obtained from

$$Q_{Al_{1-z}Si_z}^{LQ, surplus} = Q_{Al_{1-z}Si_z}^{LQ} - Q_{Al_{1-z}Si_z}^{prec} \quad (4)$$

where  $Q_{Al_{1-z}Si_z}^{LQ}$  is the measured heat production per mole alloy. Then, the surplus heat production in terms of the heat production by the coarsening process per mole initially present silicon particles,  $Q_{Si}^{coars}$ , can be given by (cf. eqs. (A-1) and (A-2) in the Appendix):

$$Q_{Al_{1-z}Si_z}^{LQ, surplus} = \frac{z-x}{1-x} \cdot Q_{Si}^{coars} \quad (5)$$

Data obtained for  $Q_{Al_{1-z}Si_z}^{LQ, surplus}$  (eqs. (3) and (4) where  $Q_{Si}^{SQ}$  has been taken for  $Q_{Si}^{prec}$ ; see section 5.1.) are shown as a function of

$(z-x)/(1-x)$  in Fig. 9. For the hypo-eutectic alloys (up to 14 at% Si; section 3) a linear relation between  $Q_{Al_{1-z}Si_z}^{LQ, surplus}$  and  $(z-x)/(1-x)$  is observed, implying a constant value for  $Q_{Si}^{coars}$  (≠ slope of straight line):

$$Q_{Si}^{coars(hypo)} = 13 \text{ kJ/mole.}$$

For the hyper-eutectic alloy (19.1 at% Si) it follows:

$$Q_{Si}^{coars(hyper)} = 4.3 \text{ kJ/mole}$$

In the coarsening process two contributions for the gain in energy can in principle be discerned: (i) misfit-strain relaxation and (ii) reduction of the Si-particle/Al-rich matrix interfacial area, which will be discussed successively.

The significant difference between atomic volumes (of in particular silicon, in the present case) for second-phase particles and matrix can induce appreciable strain development in matrix and second-phase particles during precipitation (for a quantitative discussion see Reference 6). As long as the volume misfit is accommodated fully elastically, the associated total misfit-strain energy,  $W^m$ , induced in a specimen composed of a misfitting particle B of volume  $v_B$  in a matrix A can be calculated from (cf. Reference 13 and see also Reference 14):

$$W^m = 6 \cdot G_A \cdot \frac{3 K_B}{3 K_B + 4 G_A} \cdot v_B \cdot \epsilon_B^2 / A \quad (6)$$

where G and K denote shear and bulk moduli and  $\epsilon$  is the linear misfit parameter. This equation holds for either coherent or incoherent B-particles of spherical shape. (It is already remarked here that the Si particles in the LQ alloys before and after annealing are of approximately spherical shape: Figs. 3a,b and 6a and see Reference 16). Then, the misfit-strain energy per mole silicon,  $W_{Si/Al}^m$ , of a specimen containing Si-precipitates in an Al-matrix can be given by

$$W_{Si/Al}^m = 6 \cdot G_{Al} \cdot \frac{3 K_{Si}}{3 K_{Si} + 4 G_{Al}} \cdot \frac{A_{Si}}{\rho_{Si}} \cdot \epsilon_{Si/Al}^2 \quad (7)$$

where  $A$  and  $\rho$  are atomic weight and specific density. Using literature data for  $G$ ,  $K$ ,  $A$  and  $\rho$  (see Reference 15) and taking the value for  $\epsilon$  given in Reference 16, it is obtained

$$W_{Si/Al}^m = 6 \text{ kJ/mole Si}$$

If during the precipitation on annealing, in the DSC apparatus, a full relaxation of the misfit strains induced initially by the precipitating particles occurs, no net effect of the associated misfit-strain energy on the total amount of heat produced results. Previous analyses of lattice-parameter behaviour during precipitation suggest that strains evoked by the precipitation process of initially dissolved silicon are fully (LQ alloys) or largely (SQ alloys) relaxed during the precipitation for "normal" precipitation times and temperatures<sup>[6,16,17]</sup>. It may, however, be suggested that no complete misfit-strain relaxation occurs during LQ for those Si-particles which precipitate in the low-temperature region of the quench (see section 4.2). Therefore, part of the surplus heat production in the LQ-alloys may be due to such strain relaxation; cf. the above given values for  $Q_{Si}^{coars}$  and  $W_{Si/Al}^m$ .

For spherical Si-particles of radius  $r_{Si}$  in an Al-matrix, the interfacial energy per mole silicon,  $W_{Si/Al}^S$ , is given by

$$W_{Si/Al}^S = 3 \cdot \frac{A_{Si}}{\rho_{Si}} \cdot \frac{1}{r_{Si}} \cdot \sigma_{Si/Al} \quad (8)$$

where  $\sigma_{Si/Al}$  denotes the interfacial energy per unit area interface. A reasonable estimate for  $\sigma_{Si/Al}$  appears to be  $1.5 \text{ J/m}^2$ <sup>[18]</sup>. As an example the change in interfacial energy,  $\Delta W_{Si/Al}^S$ , is estimated for the initially present Si-particles in the LQ AlSi (7.2 at% Si) alloy during the nonisothermal annealing treatment. TEM analysis leads to the following

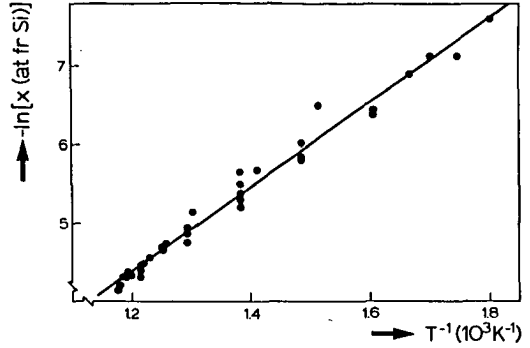


**Figure 8.**

$-\ln x$ , where  $x$  = composition of the Al-rich phase, as a function of the reciprocal of the solvus temperature,  $T$ . Data taken from Table 3 of Reference 11.

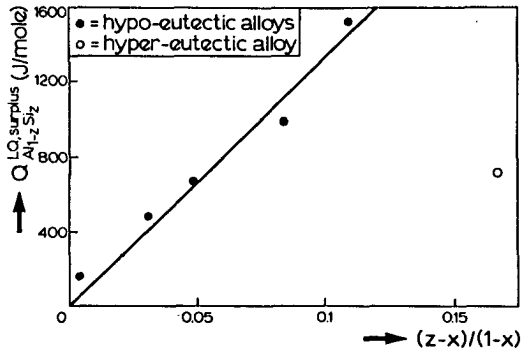


**Figure 9.**

The surplus heat production in LQ AlSi-alloys,  $Q_{Al_{1-x}Si_x}^{LQ, surplus}$  (per mole alloy) as a function of  $(z-x)/(1-x)$ , where  $z$  = gross silicon content and  $x$  = composition of the Al-rich matrix.

assessment of average values for  $r_{Si}$  before and after the annealing treatment (see Figs. 3a and 3b): 4 nm and 20 nm. Then, using literature data for  $A_{Si}$  and  $\rho_{Si}$ <sup>[15]</sup>, it is obtained

$$\Delta W_{Si/Al}^S = 11 \text{ kJ/mole Si}$$

Finally, comparing the experimental value for  $Q_{Si}^{coars(hypo)}$  with the predicted values for  $W_{Si/Al}^m$  and  $\Delta W_{Si/Al}^s$ , it can be concluded that coarsening of the Si-particles initially present in the LQ AlSi alloys can explain the surplus heat production observed for the LQ alloys, as compared to the SQ alloys; reduction of interfacial area and misfit-strain relaxation can in principle contribute significantly. The smaller value for the surplus heat production in the hyper-eutectic alloy, as compared to the hypo-eutectic alloys (cf. above given results for  $Q_{Si}^{coars(hypo)}$  versus  $Q_{Si}^{coars(hyper)}$ ; Fig. 9), can be ascribed to the presence of primary and consequently relatively coarse Si-particles in the as-quenched hypereutectic alloy.

## 6. Kinetics of precipitation

Consider the variable  $\beta$  defined as

$$\beta(t) = \int_0^t k dt = \int_0^t k_0 \exp \{-E_A/RT\} dt \quad (9)$$

where  $E_A$  is an effective activation energy describing the overall process and  $t$ ,  $k_0$ ,  $R$  and  $T$  denote the annealing time, the pre-exponential factor, the gas constant and the absolute temperature, respectively. For nonisothermal annealing  $T$ , and thus  $k$ , depends on  $t$ . For nonisothermal annealing with a constant heating rate it was recently derived that, if  $\beta$  is adopted as a state variable for the (solid-state) transformation concerned (this is for example compatible with Johnson-Mehl-Avrami kinetics), the following relation between the temperature for a fixed stage of transformation,  $T_f$ , and the activation energy,  $E_A$ , holds<sup>[19]</sup>

$$\ln \frac{T_f^2}{\Phi} = \frac{E_A}{RT_f} + \ln \beta_f \quad (10)$$

where  $\Phi$  denotes heating rate. Hence, for a series of experiments each with a different heating rate, the activation energy can be determined from the slope of the straight line obtained by plotting  $\ln(T_f^2/\Phi)$  versus  $1/T_f$ . It

can be shown that the stage of transformation where the maximal rate of transformation occurs, is approximately independent on the heating rate<sup>[19]</sup>. In a DSC experiment the temperature where the maximal heat effect is observed can be taken as approximately equal to the temperature of maximal reaction rate (a correction, if necessary, can be performed: see Res. 1 in eq. (13) of Reference 20). Thus, in the present work, for activation-energy analysis  $T_f$  in eq. (10) has been taken equal to  $T_p$ , the peak temperature as observed in the DSC experiment. For this specific stage of maximal transformation rate the procedure described resembles the so-called Kissinger analysis<sup>[21]</sup> and variants thereof<sup>[22]</sup>. However, the latter methods have been derived for homogeneous reactions only, whereas solid-state transformations usually are heterogeneous reactions (see general treatment in Reference 19).

Data obtained for the activation energy of silicon precipitation in the LQ AlSi alloys are plotted in Fig. 10 as a function of the composition of the Al-rich phase. Precipitation of silicon requires diffusion of silicon atoms. All values found for the activation energy are significantly smaller than the value corresponding with volume diffusion of silicon in aluminium (about 130 kJ/mole<sup>[23]</sup>).

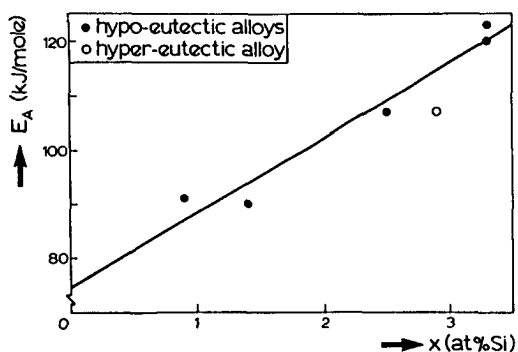


Figure 10.

The activation energy of silicon precipitation,  $E_A$ , in LQ AlSi-alloys as a function of the composition of the Al-rich matrix,  $x$ .

It is likely that after liquid quenching excess vacancies occur in the Al-rich phase (e.g. see References 4, 9). The activation energy for volume diffusion of silicon can be conceived as the sum of the contributions due to formation and migration of a vacancy, which both amount to about 62 kJ/mole<sup>[24]</sup>. It can then be expected that in the presence of excess vacancies the effective activation energy of silicon precipitation will be in the range 62-124 kJ/mole, as observed (cf. Fig. 10).

It is striking to note that the activation energy for the LQ alloys increases with an increasing content of dissolved silicon (Fig. 10). In accordance with the above discussion it is thus suggested that the excess vacancy concentration (relative to the amount of dissolved silicon) decreases for an increasing amount of dissolved silicon. This result can be discussed in several ways. For example, realizing that the Al-matrix grain size decreases if the gross content of silicon increases<sup>[12]</sup>, annihilation of excess vacancies during annealing can be more pronounced for larger gross contents of silicon. Also, realizing that on liquid quenching solidification begins at a relatively high temperature for a (hypoeutectic) AlSi alloy containing a relatively small gross content of silicon (for the hypoeutectic AlSi alloys a larger gross content of silicon leads to a larger amount of dissolved silicon; see Fig. 1 and the corresponding discussion in section 3), a relatively large amount of (excess) vacancies can be retained after liquid quenching for a relatively small gross content of silicon as the equilibrium amount of vacancies increases with temperature.

The present activation-energy data for LQ alloys have been obtained by nonisothermal annealing experiments and can be compared with previous data<sup>[5]</sup> derived from isothermal annealing experiments. The peak maximum of the DSC curves used here for activation-energy analysis by nonisothermal annealing occurs at a temperature 50-100 K higher than the temperatures used earlier for isothermal

annealing. This could explain a somewhat larger value for the effective activation energy as obtained in the present work because of a more pronounced stage of vacancy annihilation.

No significant dependence of the activation energy for silicon precipitation on (gross) content of silicon was found for the SQ alloys. This is consistent with the above discussion for the LQ alloys, because the SQ alloys were annealed at the same temperature before SQ, implying identical vacancy concentrations (and identical amounts of dissolved silicon).

The average value of the activation energy for the SQ alloys equals: 89 kJ/mole. Thus the present method of (drastic) SQ (see section 2.1 and Reference 9) involves that after SQ an amount of (excess) vacancies is retained which is comparable with that after LQ.

## 7. Conclusions

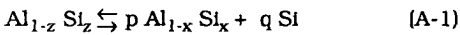
- (i) The precipitation of silicon starts generally earlier in LQ than in SQ alloys because of a larger driving force due to a larger silicon super-saturation.
- (ii) The total exothermic heat effect for the LQ alloys is caused by two processes: precipitation of silicon initially dissolved in the Al-rich phase and coarsening of the Si particles already present after liquid quenching.
- (iii) The heat produced by precipitation of silicon has been determined from the experiments with the SQ alloys as 58 kJ/mole silicon (initially dissolved).
- (iv) The surplus heat production for the LQ alloys equals 13 kJ/mole silicon (initially present particles). It can be ascribed primarily to reduction of the amount of interfacial area between Si particles and Al-rich matrix (calculated as 11 kJ/mole silicon) and possibly also to relaxation of the misfit strains due to the atomic volume difference for silicon as second-phase particle

(precipitated in the low temperature region of the quench) and as dissolved element (calculated as, at most, 6 kJ/mole silicon).

(v) Activation energies for silicon precipitation in both LQ and SQ alloys are smaller than that for volume diffusion of silicon in aluminium because of the presence of quenched-in excess vacancies. The activation energy for the (hypoeutectic) LQ alloys increases with the amount of silicon dissolved initially. This is ascribed to a solidification start temperature on liquid quenching that decreases for an increasing gross content of silicon and/or an Al-matrix grain size that decreases for increasing gross content of silicon; both effects can lead to a decrease of the excess vacancy concentration (relative to the amount of dissolved silicon).

#### Appendix: Calculation of heat production

Consider an AlSi alloy composed of an Al-rich matrix containing an atomic fraction  $x$  of dissolved silicon and dispersed silicon particles. The (hypothetical) formation of this two-phase system out of the homogeneous one-phase alloy containing an atomic fraction  $z$  of dissolved silicon can be described by



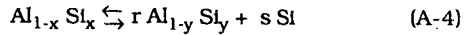
Conservation of mass requires

$$p = \frac{1-z}{1-x} \quad \text{and} \quad q = \frac{z-x}{1-x} \quad (\text{A-2})$$

It thus follows that the heat produced on precipitation of silicon from the Al-rich matrix per mole Al-rich matrix, i.e.  $Q_{\text{Al}_{1-x}\text{Si}_x}$  can be derived from the measured heat production per mole alloy, i.e.  $Q_{\text{Al}_{1-z}\text{Si}_z}$  according to

$$Q_{\text{Al}_{1-x}\text{Si}_x} = \frac{1-x}{1-z} \cdot Q_{\text{Al}_{1-z}\text{Si}_z} \quad (\text{A-3})$$

The precipitation reaction in the Al-rich matrix can be expressed as



where  $y$  denotes the (equilibrium) atomic fraction of silicon dissolved in the Al-rich matrix after completed precipitation. Conservation of mass requires

$$r = \frac{1-x}{1-y} \quad \text{and} \quad s = \frac{xy}{1-y} \quad (\text{A-5})$$

Consequently,  $p \cdot s$  moles of silicon precipitate per mole alloy (eqs. (A-1) and (A-4)). Hence, the heat produced per mole precipitated silicon, i.e.  $Q_{\text{Si}}$ , can be derived from the measured heat production per mole alloy, i.e.  $Q_{\text{Al}_{1-z}\text{Si}_z}$ , according to

$$Q_{\text{Si}} = \frac{(1-x)(1-y)}{(1-z)(x-y)} \cdot Q_{\text{Al}_{1-z}\text{Si}_z} \quad (\text{A-6})$$

Obviously, it follows immediately from eqs. (A-4) and (A-5)

$$Q_{\text{Al}_{1-x}\text{Si}_x} = \frac{x-y}{1-y} \cdot Q_{\text{Si}} \quad (\text{A-7})$$

and, if  $Q_{\text{Si}}$  does not depend on  $x$ , a plot of  $Q_{\text{Al}_{1-x}\text{Si}_x}$  versus  $x$  yields a straight line with a slope governed by  $Q_{\text{Si}}$ .

#### Acknowledgements

The authors are indebted to Mr. P.J. van der Schaaf for skilful overall experimental assistance, to Ir. P. van Mourik for X-ray diffraction work, to Mr. C.D. de Haan for electron microscopical work and to Ir. P. van Mourik and Professor B.M. Korevaar for discussion.

## References

1. T.R. Anantharaman and C. Suryanarayana: Rapidly Solidified Metals, Trans. Tech. SA, Aedermannsdorf, Switzerland, 1987, pp. 1-4.
2. A. Bendijk, R. Delhez, L. Katgerman, Th.H. de Keijser, E.J. Mittemeijer and N.M. van der Pers: J. Mater. Sci. 15 (1980), pp. 2803-2810.
3. P.H. Shingu, K. Kobayashi, K. Shimomura and R. Ozaki: J. Jap. Inst. Met. 37 (1973), pp. 433-440.
4. P. van Mourik, Th.H. de Keijser and E.J. Mittemeijer: Proc. 5th Int. Conf. Rap. Quenched Metals, Würzburg (West Germany), September 3-7, 1984, S. Steeb and H. Warlimont (eds.), pp. 899-902.
5. P. van Mourik, E.J. Mittemeijer and Th.H. de Keijser: J. Mater. Sci. 18 (1983), pp. 2706-2720.
6. P. van Mourik, Th.H. de Keijser and E.J. Mittemeijer: Proc. 1st Int. Conf. on Rapidly Solidified Materials (eds. P.W. Lee and R.S. Carbonara, San Diego, (California (USA), February 3-5, 1986), ASM, Metals Park, Ohio (USA), 1986, pp. 341-350.
7. I. Yamauchi, I. Ohnaka, S. Kawamoto and T. Fukusako: Trans. Jap. Inst. Met. 27 (1986), pp. 187-194.
8. K. Kobayashi, M. Kumikawa and P.H. Shingu: J. Jap. Inst. Met. 49 (1985), pp. 59-63.
9. M. van Rooyen, J.A. Sinte Maartensdijk and E.J. Mittemeijer: Metall. Trans. A, in press.
10. M. van Rooyen, J.A. van der Hoeven, L. Katgerman, P. van Mourik, Th.H. de Keijser and E.J. Mittemeijer: Proc. P.M. Aerospace Mater. Conf. Berne (Switzerland), November 1984, Vol. 1, edited by Metal Powder Report, pp. 34-1-16.
11. J.L. Murray and A.J. McAlister: Bull. Alloy Phase Diagr. 5 (1984), pp. 74-84.
12. M. van Rooyen, N.M. van der Pers, L. Katgerman, Th.H. de Keijser and E.J. Mittemeijer: Proc. 5th Int. Conf. Rap. Quenched Metals, Würzburg (West Germany), September 3-7, 1984, S. Steeb and H. Warlimont (eds.), pp. 823-826.
13. J.W. Christian: The Theory of Transformations in Metals and Alloys, 2nd ed., Pergamon Press, Oxford, 1975, part I.
14. M.A.J. Somers, R.M. Lankreijer and E.J. Mittemeijer: Phil. Mag., in press.
15. C.J. Smithells (ed.), Metals Reference Book, 5th ed., Butterworths, London, 1976.
16. E.J. Mittemeijer, P. van Mourik and Th.H. de Keijser: Phil. Mag. A, 43 (1981), pp. 1157-1164.
17. P. van Mourik, Th.H. de Keijser and E.J. Mittemeijer: Scripta Met. 21 (1987), pp. 381-385.
18. K. Kobayashi, P.H. Shingu, H. Kanbara and R. Ozaki: Trans. Jap. Inst. Met. 17 (1976), pp. 545-550.
19. E.J. Mittemeijer, Liu Cheng, P.J. van der Schaaf, C.M. Brakman and B.M. Korevaar: Metall. Trans. A, 19A (1988), pp. 925-932.
20. E.J. Mittemeijer, A. van Gent and P.J. van der Schaaf: Metall. Trans. A, 17A (1986), pp. 1441-1445.
21. H.E. Kissinger: Anal. Chem. 29 (1957), pp. 1702-1706.
22. T. Ozawa: J. Therm. Anal. 2 (1970), pp. 301-324.
23. M.E. Bishop and K.E. Fletcher: Int. Met. Rev. 17 (1972), pp. 203-225.
24. R.W. Siegel: J. Nucl. Mater., 69-70 (1978), pp. 117-146.

### **III. MECHANICAL PROPERTIES OF RAPIDLY SOLIDIFIED ALUMINIUM ALLOYS AFTER HOT COMPACTION**

#### **III.1. CONSOLIDATION AND RESULTING TENSILE STRENGTH OF MELT-SPUN ALMG AND ALSI ALLOYS**

(M. van Rooyen, J. A. van der Hoeven, L. Katgerman, P. van Mourik, Th. H. de Keijser and E.J. Mittemeijer, Powder Metallurgy Aerospace Materials Conf., Berne, Switzerland, November 12-14, 1984)

#### **III.2. MORPHOLOGY AND MECHANICAL PROPERTIES OF MELT-SPUN AND CONVENTIONALLY CAST ALUMINIUM, ALMG AND ALSI ALLOYS BEFORE AND AFTER HOT EXTRUSION**

(M. van Rooyen, P.F. Colijn, Th. H. de Keijser and E.J. Mittemeijer, J. Mater. Sci. 21(1986)2373).

#### **III.3. STRUCTURE REFINEMENT AND IMPROVED MECHANICAL PROPERTIES OF AL-20 WT.% SI BY RAPID SOLIDIFICATION IN CONJUNCTION WITH STRONTIUM MODIFICATION**

(M. van Rooyen, N.M. van der Pers, Th. H. de Keijser and E.J. Mittemeijer, Mat. Sci. and Eng. 96(1987)17).

## CONSOLIDATION AND RESULTING TENSILE STRENGTH OF MELT-SPUN AlMg AND AlSi ALLOYS

M. van Rooyen, J.A. van der Hoeven, L. Katgerman\* , P. van Mourik,  
Th.H. de Keijser and E.J. Mittemeijer

Laboratory of Metallurgy, Delft University of Technology,  
Rotterdamseweg 137, 2628 AL Delft, The Netherlands

\*Now with ALCAN Int. Ltd. Banbury Laboratories,  
Banbury, Oxon, England, OX 167 SP

Al, AlMg (0-16.5 at% Mg) and AlSi (0-20.2 at% Si) alloys were rapidly quenched by melt-spinning. After precompaction of the ribbons, a part of the densified material was degassed. Both degassed and undegassed materials were consolidated by hot extrusion. The microstructural morphology was examined by light-microscopical analysis. Tensile properties of the extruded bars were determined both in longitudinal and transverse directions. For comparison such tensile testing was also applied to extruded conventionally cast materials of identical compositions. In general, as compared to the conventionally cast materials, melt-spun AlMg alloys showed an inferior mechanical behaviour, whereas melt-spun AlSi alloys exhibited an improved mechanical performance. In the case of relatively large alloying-element contents, degassing before extrusion led to inferior mechanical properties. The main advantage of the rapid-solidification technique appears to be the resulting ultrafine grain size and the very fine second-phase dispersion. This offers possibilities for the processing of aluminium based (automobile) scrap.

### 1. Introduction

At present improved strength and/or processing of aluminium-based scrap are pursued in aluminium-alloy development. By rapid quenching from the melt metastable aluminium alloys can be obtained, which, as compared to conventionally cast materials, can show<sup>[1-4]</sup>:

- decreased grain size;
- increased chemical homogeneity (including extended alloying-element solid solubilities);

- increased densities of lattice imperfections (including quenched-in excess vacancies).

Many techniques for liquid quenching have been developed<sup>[5]</sup>. The relatively easily accessible melt-spinning technique yields cooling rates of the order  $10^6$  K/s. A description of the microstructure of melt-spun aluminium alloys is provided in References 6 to 10.

In general melt-spun ribbons (with a thickness of 25-50  $\mu\text{m}$  and a width of about 2 mm) cannot be used directly in practice. The ribbons should be bonded together to obtain a sound product. This process step of consolidation should bring about intimate contact between the ribbons (cf. "pressure welding") such that the resulting density (nearly) equals the theoretical density. (Hot) extrusion could meet this requirement. In such a process the main problem is to preserve the profitable properties gained by rapid solidification.

One of the advantages of the rapid solidification technology discussed above can be the ability to process aluminium-based (automobile) scrap with no refining and/or diluting steps. As a first step towards understanding the rapid solidification processing behaviour of commercial aluminium alloys, binary AlMg and AlSi alloys have been investigated in this work.

In the present paper we only present results on tensile testing after consolidation. A detailed description of the microstructure before and after consolidation will be presented elsewhere; however, in the present discussion the basic microstructural findings will be related to the tensile-testing results.

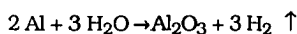
## 2. Aspects of consolidation by extrusion of aluminium alloys

### 2.1. Precompaction

To obtain a manageable specimen, precompaction of melt-spun ribbons is necessary. For a rapid degassing after precompaction, the utmost density to be attained by precompaction equals about 85% of the theoretical value (e.g. see References 11 to 14). In the case of uniaxial compaction friction between the press cylinder and the ribbons can lead to undesired heterogeneity of the density after precompaction<sup>[13]</sup>.

### 2.2. Degassing

Aluminium-alloy specimens are normally covered with an oxide layer. These oxides can be hygroscopic implying bonding of  $\text{H}_2\text{O}$  molecules to melt-spun ribbons of aluminium alloys. Heat treatment could cause release of  $\text{H}_2\text{O}$  molecules and subsequently a reaction of the type



might occur. This could lead to blisters and, eventually delamination of the extruded product (e.g. see References 11, 13, 15 to 17). An analogous problem occurs on sintering aluminium powder (SAP)<sup>[18,19]</sup>. Degassing until pressures in the range of  $10^{-7}$ - $10^{-6}$  atm are reached, can avoid blister formation (e.g. see Reference 20). However, at the corresponding degassing temperature microstructural changes can be induced causing loss of mechanical strength.

### 2.3. Ram speed, extrusion ratio and temperature

In general a load limitation and a temperature limitation can be recognized. These operating constraints can be represented in a limit diagram, which, for example, can be obtained by plotting (the logarithm of) the *maximal* extrusion ratio as a function of preheating (billet) temperature for specified ram speeds<sup>[21]</sup> (Figure 1). Note that speed, deformation and temperature are interdependent extrusion parameters.

The following remarks can be made:

- At a relatively low temperature upper bounds for both extrusion ratio and ram speed (in combination) exist as a consequence of the finite press pressure available: sticking in the extrusion container should not occur.
- At a relatively high temperature upper bounds for both extrusion ratio and ram speed (in combination) exist as a consequence of heat production by energy dissipation provoking undesired microstruc-

tural changes (e.g. excessive coarsening). Ultimately, melting might occur, leading to the "firtree cracking" appearance<sup>[22]</sup>.

- An increase of ram speed decreases the possible maximum extrusion ratio for any temperature.

In practice temperature control of billets to within (20-50) K is possible. Preheating (billet) temperatures of (50-100) K below the solidus temperature are employed<sup>[22]</sup>. Normally the ram speed cannot be precisely controlled, in contrast with the extrusion ratio. In poly-phase materials a high extrusion ratio, but satisfying the constraints discussed above, leads to large deformation gradients across the phase boundaries, possibly causing internal cracks. For consolidation of melt-spun ribbons a low extrusion ratio could imply insufficient contact between the ribbons, causing porosity. Extrusion ratios in the range of 10-50 are employed<sup>[11, 15 to 17, 23, 24]</sup>.

### 3. Experimental procedure

#### 3.1. Melt-spinning

AlMg (0-16.5 at% Mg) and AlSi (0-20.2 at% Si) alloys were prepared from 99.998 wt% Al, 99.38 wt%Mg and 99.99 wt% Si. Specimens in the form of ribbons (thickness 25-50  $\mu\text{m}$ ; width about 2 mm) were made by melt-spinning in an air atmosphere. The melt-spinning equipment (Figure 2) consisted of a graphite crucible in a quartz tube and a rotating copper wheel (diameter 294 mm; circumferential velocity 23.1-46.2 m/s). The metal was melted by induction heating and ejected through an orifice in the bottom of the crucible (diameter 0.8 mm) onto the cylindrical surface of the rotating wheel by an overpressure (0.08 atm) of argon. The molten metal temperature was chosen 100-150 K above the equilibrium liquidus temperature. The composition of the ribbons produced was determined by chemical analysis.

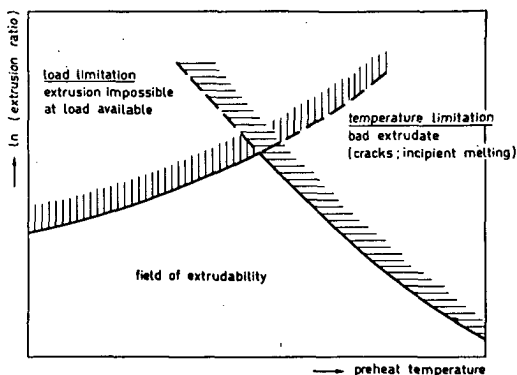


**Fig. 1.** Limit diagram for extrusion. The load and temperature limitations indicated hold for a certain ram speed.

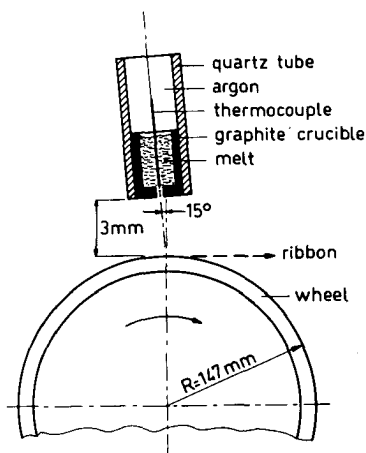


**Fig. 2.** Melt-spinning equipment.

#### 3.2. Precompaction and canning

Precompaction of the ribbons was performed by cold pressing in a steel cylinder yielding cylindrical billets having densities 63-76% of the theoretical value. From each

alloy at least 4 billets were produced. Canning implied insertion of two billets in a container made of AA6082 (0.7-1.3 wt% Si, 0.6-1.2 wt% Mg, <0.2 wt% Zn, <0.1 wt% Fe, <0.1 wt% Ti, balance Al).

### 3.3. Degassing

One of the canned billets for each alloy investigated was degassed by vacuum annealing. Degassing temperatures applied were about 715 K and 730 K for the AlMg and the AlSi alloys respectively. Degassing was continued until pressures smaller than  $2 \times 10^{-7}$  atm were reached. After cooling to room temperature enclosure of the billet was achieved by electron-beam welding of a lid onto the container.

### 3.4. Extrusion

Canned, degassed and undegassed, billets as well as some uncanned undegassed billets were hot extruded. Extrusion temperatures employed were about 675 K and 725 K for the AlMg and AlSi alloys respectively. Preheating of the specimens in the extrusion container was applied to achieve a homogeneous temperature distribution within the billets before extrusion. In particular for the canned specimens it appeared necessary to employ preheating times of at least 30 min. A preheating time of 40 min. was employed usually. The extrusion ratio usually employed was 25 (with an extrusion speed of about 1 m/min. corresponding to a ram speed of about 7 cm/min.); in some cases an extrusion ratio of 44.4 was applied. After extrusion air cooling of the extruded bars occurred.

For comparison conventionally cast material\* was extruded under analogous conditions.

\* Specimens were prepared from Al, Mg and Si of purity as indicated in section 3.1. by gravity-die casting followed by annealing for 65 h at about 710 K and 815 K for the AlMg and AlSi alloys respectively.

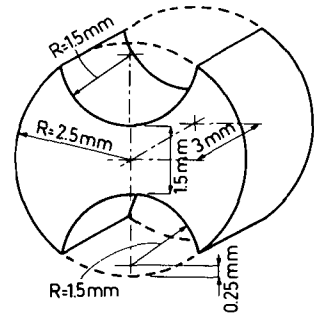


Fig. 3a.  
Transverse-tensile specimen.

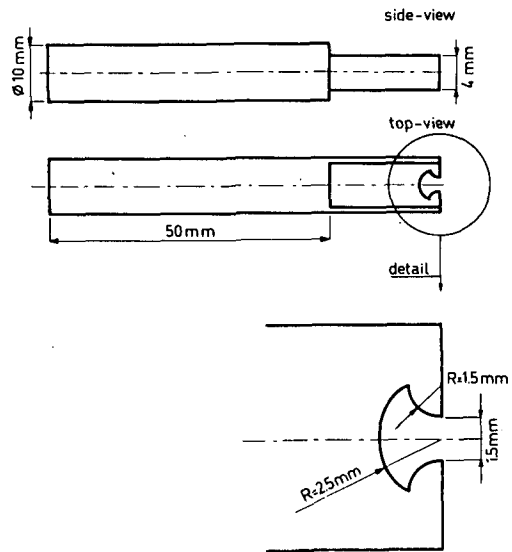


Fig. 3b.  
Gripping jaw for transverse-tensile testing.

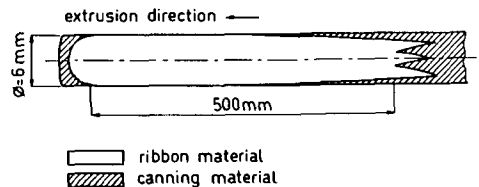


Fig. 4.  
Distribution of canning and ribbon material; longitudinal section of extrudate.



**Fig. 5a.** Transverse section of initial part of extrudate showing poor bonding between ribbons. Uncanned precompacted AlMg (2.3 at% Mg) ribbons extruded with an extrusion ratio of 44.4; optical micrograph.



**Fig. 5b.** Transverse section of last part of extrudate showing pores. Uncanned precompacted Al ribbons extruded with an extrusion ratio of 44.4; optical micrograph.

### 3.5. Tensile testing

After removal, by machining, of the canning material from the extruded bars, specimens were prepared for tensile testing in longitudinal and transverse directions. Longitudinal-tensile specimens were prepared according to DIN 50125 with a length/diameter ratio equal to 10. Because of the small diameter of the extruded bar (usually 6 mm), transverse-tensile specimens could not be made according to a standard as mentioned above. Instead transverse-tensile specimens were prepared following the design presented in Figure 3(a);

corresponding gripping jaws for the tensile-testing machine were made according to Figure 3(b). An Instron tensile-testing machine (Model TTCML MI 1.4.6.) was applied. For each strength value presented about 4 tensile experiments were performed.

## 4. Extrusion process

In the case of canned billets at the start of the extrusion easy slip is possible between can and billet. As a result the initial part of the extrudate contains a relatively large amount of ribbon material. At the end of the

extrusion, as the ram approaches the die, the "dead-metal region" is broken up and the extrudate contains a relatively large amount of canning material (Figure 4).

On extruding at first a compaction of the (already precompact) ribbons takes place corresponding to a non-linear increase of load. Poor bonding between the ribbons occurs (Figure 5(a)).

In the final stages of the extrusion the deformation can be that large that shear along the interfaces between a yielding, soft (aluminium) matrix and unyielding, hard second-phase (e.g. oxide/precipitate) particles leads to porosity (Figure 5(b)).

At intermediate ("quasi-static") stages of extrusion the deformation process is such that a continuous creation and destruction of bonds between ribbons takes place, accompanied by breaking up the oxide layers at the ribbon surfaces, until normal shear processes occur finally. To achieve a coherent product on extruding ribbons, the redundant work\* for the extrusion will be larger than that for the extrusion of massive conventional castings.

\* Other energy terms involved are the work of homogeneous deformation (characterized by the logarithm of the extrusion ratio) and the work done by the (extrusion-geometry dependent) friction forces.

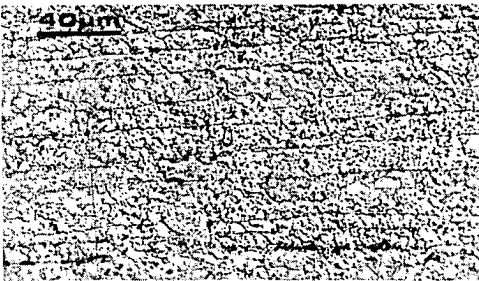


**Fig. 6.** Longitudinal section of extrudate showing reminiscences of former ribbon surfaces. Canned precompact AlSi (2.3 at% Si) ribbons extruded with an extrusion ratio of 25; optical micrograph.

The billets before extrusion exhibit a random arrangement of the ribbons. During extrusion the ribbons are stretched and aligned roughly parallel to the extrusion direction. This is suggested by lines parallel to the extrusion direction in optical micrographs of longitudinal sections which may arise from fragmented remnants of oxide films by etching (e.g. Figure 6). Furthermore, the ratio of the ribbon thickness before extrusion to the distance between these parallel lines is approximately equal to the square root of the extrusion ratio (Figure 7). According to the process of homogeneous deformation, this finding indicates that the distance between the parallel lines can be interpreted as the "ribbon thickness" after extrusion.

The ribbon-straightening effect can be considered as a consequence of a metal flow in the longitudinal direction which is inhomogeneous over the transverse section, while maintaining the ribbon morphology (imagine tangled threads of wool being spun).

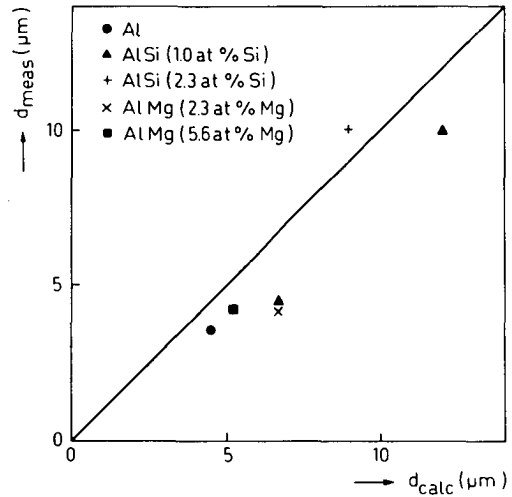


**Fig. 7.** The measured "ribbon thickness" after extrusion,  $d_{meas}$ , versus the calculated one,  $d_{calc}$ , as obtained from the division of the ribbon thickness before extrusion by the square root of the extrusion ratio.



**Fig. 8.** Transverse section of extrudate showing large recrystallized grains in surface layer. Uncanned precompacted Al ribbons extruded with an extrusion ratio of 44.4; optical micrograph.

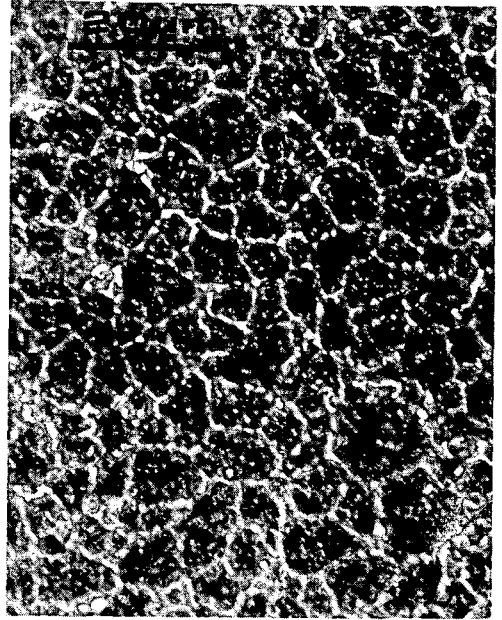


**Fig. 9.** Transverse section of extrudate showing a micro-structure suggesting melting during extrusion (see text). Uncanned precompacted AlMg (16.5 at% Mg) ribbons extruded employing a preheat temperature of about 725 K and an extrusion ratio of 44.4; optical micrograph (phase contrast).

Two undesired effects caused by inappropriate extrusion conditions should be indicated:

- A surface layer of large recrystallized grains may occur (Figure 8). In metals with a high stacking-fault energy, such as aluminium, recovery processes occur during hot extrusion (*dynamic recovery*). This recovery can be most distinct in the surface region (also recognizing that the extrusion-induced temperature rise is largest in the surface region; cf. section 2.3.). Immediately after extrusion *static recrystallization* occurs and large grains develop at the surface (small residual deformation).

- Melting may occur. Energy dissipation during extrusion could ultimately lead to melting of the material to be extruded (cf. section 2.3.). An example is shown in Figure 9: precompacted AlMg (16.5 at% Mg) ribbon material was extruded employing a preheat temperature of about 725 K (whereas the corresponding solidus temperature equals about 740 K). After extrusion no reminiscences of ribbon surfaces are discernable; the grains are equiaxed and of about the same size. Also, the load to be applied during extrusion was relatively small.

## 5. Tensile strength

The ultimate tensile strength in both the longitudinal and the transverse direction of the extruded bars, denoted by  $\sigma_{UTS}^{\parallel}$  and  $\sigma_{UTS}^{\perp}$  respectively, is presented in Figures 10(a)-(b) and 11(a)-(b) as a function of the alloying-element content for the AlMg and the AlSi system respectively. By plotting  $\sigma_{UTS}^{\parallel}$  versus  $\sigma_{UTS}^{\perp}$  an impression of the anisotropy of the tensile strength is obtained (Figures 12(a) and (b)). Each tensile-strength value is based on about 4 testings; the corresponding standard deviations are in the range (1-9) % with the larger values occurring for the transverse tensile strengths.

### 5.1. Strength as a function of alloying-element content

#### AlMg alloys:

From the X-ray diffraction analysis (Debye-Scherrer photographs) it followed:

- AlMg melt-spun ribbons were single-phase: all Mg in solid solution.
- AlMg extrudates of only the alloy with the largest amount of Mg of this investigation (+16.5 at% Mg) clearly showed the presence of a second phase ( $\beta$ ). This holds for both melt-spun and conventionally cast materials.

The initial increase of  $\sigma_{UTS}^{\parallel}$  for AlMg as a function of Mg-content can therefore be interpreted as due to solid-solution strengthening. The precipitation of  $\beta$ -phase particles during extrusion for large Mg-contents has a detrimental influence on  $\sigma_{UTS}^{\parallel}$  (Figure 10(a)).

The microstructure of the consolidated ribbons, as revealed by optical microscopy, showed that significant recrystallization had occurred *within* the ribbons; only rarely a recrystallized grain had grown across a ribbon boundary, implying a deficient contact between the constituents of the consolidated product. Thus the ribbon boundaries, composed of oxides (electron-microprobe analysis indicated O presence and, as com-

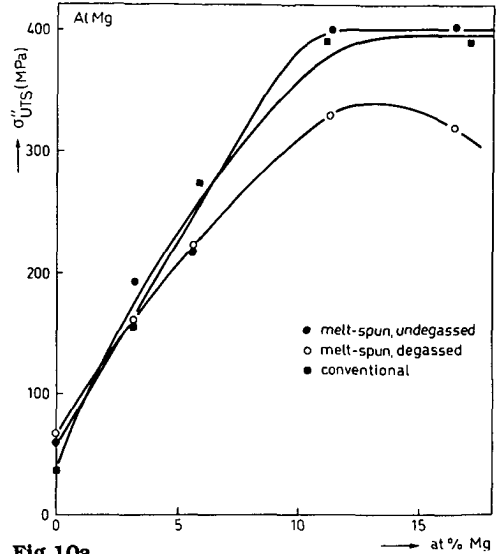


**Fig. 10a.**

Ultimate tensile strength in longitudinal direction,  $\sigma_{UTS}^{\parallel}$ , versus alloying-element content for extruded AlMg alloys prepared from either undegassed melt-spun ribbons, or degassed melt-spun ribbons or conventional castings.

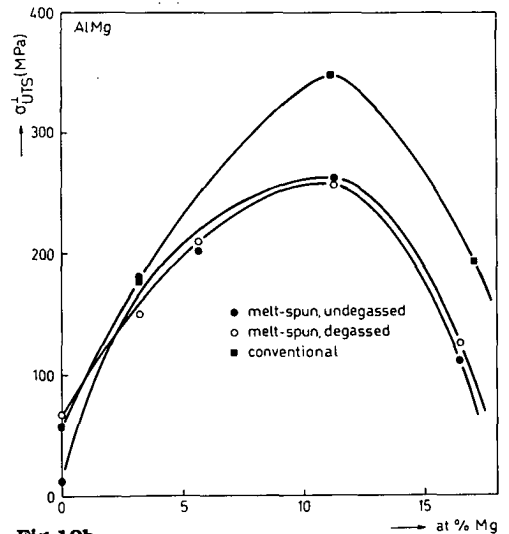


**Fig. 10b.**

Ultimate tensile strength in transverse direction,  $\sigma_{UTS}^{\perp}$ , versus alloying-element content for extruded AlMg alloys prepared from either undegassed melt-spun ribbons, or degassed melt-spun ribbons or conventional castings.

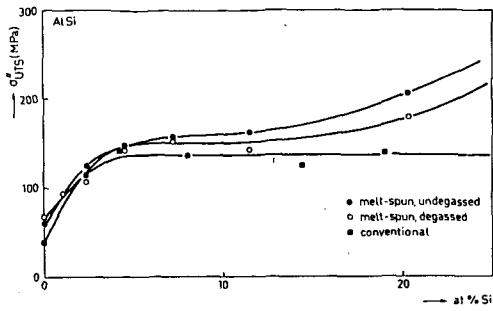


**Fig. 11a.**

Ultimate tensile strength in longitudinal direction,  $\sigma''_{UTS}$ , versus alloying-element content for extruded AlSi alloys prepared from either undegassed melt-spun ribbons, or degassed melt-spun ribbons or conventional castings.

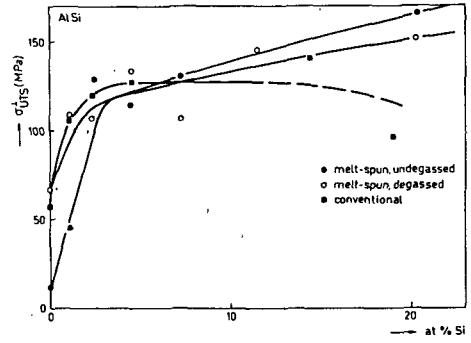


**Fig. 11b.**

Ultimate tensile strength in transverse direction,  $\sigma^{\perp}_{UTS}$ , versus alloying-element content for extruded AlSi alloys prepared from either undegassed melt-spun ribbons, or degassed melt-spun ribbons or conventional castings. Note ordinate-scale difference with Figure 11(a).

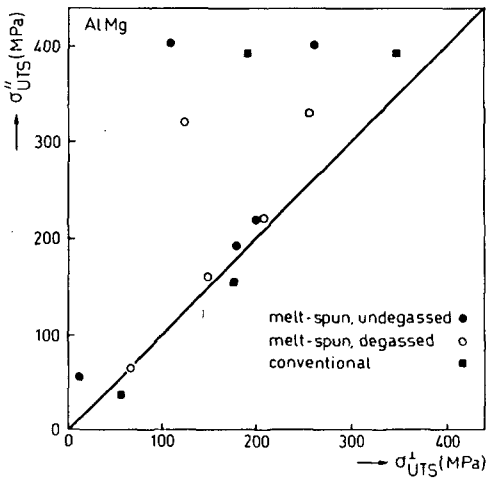


**Fig. 12a.**

Ultimate tensile strength in longitudinal direction,  $\sigma''_{UTS}$ , versus ultimate tensile strength in transverse direction,  $\sigma^{\perp}_{UTS}$ , for extruded AlMg alloys prepared from either undegassed melt-spun ribbons, or degassed melt-spun ribbons or conventional castings.

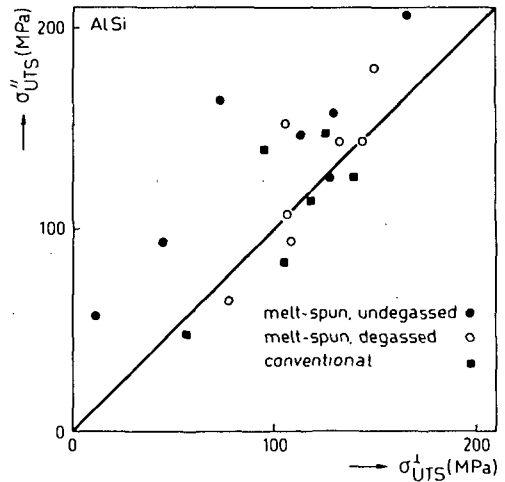


**Fig. 12b.**

Ultimate tensile strength in longitudinal direction,  $\sigma''_{UTS}$ , versus ultimate tensile strength in transverse direction,  $\sigma^{\perp}_{UTS}$ , for extruded AlSi alloys prepared from either undegassed melt-spun ribbons, or degassed melt-spun ribbons or conventional castings.

pared to the matrix, Mg enrichment), can be considered as weak places in the consolidated product. Further the ribbons were straightened in the longitudinal direction during extrusion (cf. section 4). Hence, the  $\sigma_{UTS}^{\perp}$  values for consolidated ribbons are smaller than those for extruded conventional castings (Figure 10(b)). Also the precipitation of  $\beta$ -phase particles at ribbon/grain boundaries, for both melt-spun and conventional material, particularly affects  $\sigma_{UTS}^{\perp}$  (cf. Figure 10(a) vs. 10(b)). These effects lead to marked anisotropy for the tensile strength as indicated by Figure 12(a).

#### AlSi-alloys:

From the X-ray diffraction analysis (Debye-Scherrer photographs) it followed:

- AlSi melt-spun ribbons were two-phase: an Al-rich phase (matrix) and a Si-rich phase (finely dispersed particles). We have shown earlier that by melt spinning a maximal amount of 5 at% Si can be dissolved *locally* (at thin regions) of the ribbons produced (see Figure 3 of Reference 6).
- AlSi extrudates were two-phase such that the Al-rich matrix contained an amount of Si in solid solution approximately equal to the maximal amount dissolved in equilibrium at the preheating temperature (+ about 0.5 at% Si).

The increase of  $\sigma_{UTS}^{\parallel}$  for AlSi as a function of Si-content can therefore be interpreted as due to dispersion strengthening. As compared to solid-solution strengthening (cf. the above discussion for the AlMg extrudates), dispersion strengthening is not only dependent on composition but also on particle size and spacing. This could serve to explain the tendency for a plateau in the  $\sigma_{UTS}^{\parallel}$  curve, in particular for extruded conventionally cast material (Figure 11(a)).

As a result of extrusion the grain size of the matrix and the second-phase particle size increased. However, compared to extruded conventional castings, a smaller grain size of the matrix and a smaller second-phase particle size occurred in consolidated ribbons. This leads to a tensile strength for con-

solidated melt-spun material which is significantly larger than that for extruded conventionally cast material: improvements as large as 50% occur (at about 20 at% Si; Figure 11(a)).

Oxide layers at melt-spun ribbon surfaces were much less developed for AlSi alloys than for AlMg alloys. It may therefore be understood that, as compared to consolidated AlMg ribbons, recrystallization across ribbon boundaries had occurred more frequently in consolidated AlSi ribbons, implying a more intimate contact between the constituents of the consolidated product (cf. section 1). Therefore, with reference to the transverse-tensile strength of extruded conventional castings, the transverse-tensile strength of consolidated ribbons can be better for the AlSi alloys than for the AlMg alloys. Further, analogous to the discussion of  $\sigma_{UTS}^{\parallel}$ , the relatively small size of the matrix grains and the second-phase particles even can contribute to  $\sigma_{UTS}^{\perp}$  values larger for consolidated AlSi ribbons than for extruded conventional AlSi castings (cf. Figures 11(b) and 10(b); see also section 5.2. for small Si-contents). In addition the anisotropy of the tensile strength for consolidated AlSi ribbons can be less outspoken than for consolidated AlMg ribbons (cf. Figures 12(a) and (b)).



**Fig. 13.**

Longitudinal section of extrudate after heat treatment showing pore development. Uncanned (undegassed), precompact AlMg (2.3 at% Mg) ribbons extruded with an extrusion ratio of 44.4; preheating time of 5 min. at 675 K; heat treated after extrusion during 2 h at 705 K; optical micrograph.

## 5.2. Role of degassing

With respect to porosity ascribed to H<sub>2</sub> development (cf. section 2.2.) the following observations were made:

- Extrudates of degassed melt-spun ribbons did not show any porosity;
- Extrudates of undegassed melt-spun ribbons did not show any porosity in the case a preheating time of 40 min. (cf. section 3.4.) was employed.
- A heat treatment (e.g. 2 h at about 675 K) after extrusion of both degassed and undegassed ribbons did not cause porosity in the case a preheating time of 40 min. was employed\*. However, in the case of a preheating time of 5 min. severe porosity was provoked (cf. Figure 13).

It can be concluded that preheating before extrusion can replace a (costly) degassing procedure.

\* Some porosity was found in consolidated Al and AlSi alloys with small amounts of Si (1.0 at% Si).

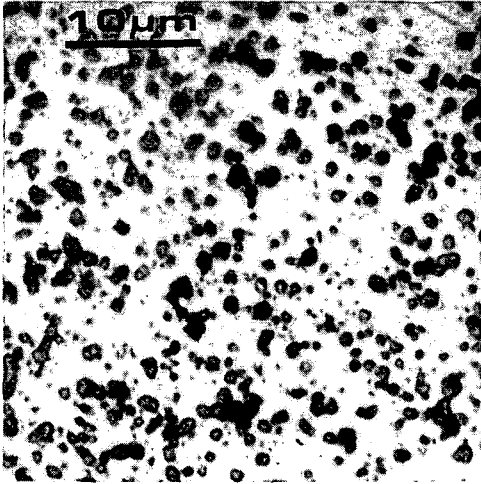


Fig. 14a.

Transverse section of extrudate from undegassed AlSi ribbons. Canned, precompact AlSi (11.4 at% Si) ribbons extruded with an extrusion ratio of 25; optical micrograph.

Obviously porosity has a detrimental effect on tensile strength. In accordance with the above observation (see footnote), improvement of (in particular transverse!) tensile strengths by degassing is expected only for consolidated melt-spun Al and AlSi alloys with small amounts of Si. This corresponds with the experimental result (Figure 11(b)). The larger tensile-strength values,  $\sigma_{UTS}^{\parallel}$  and  $\sigma_{UTS}^{\perp}$ , for consolidated degassed melt-spun ribbons of pure Al, as compared to extruded conventionally cast pure Al, may be due to oxides at the ribbon boundaries (dispersion strengthening; cf. Sintered Aluminium Powder).

The heat treatment corresponding to the degassing procedure can lead to growth of matrix grains and to precipitation and coarsening of second-phase particles (e.g. see Figure 14). Thus the degassing-induced reduction in tensile strength experienced for consolidated ribbons can be understood (Figures 10(a) and 11(a)).

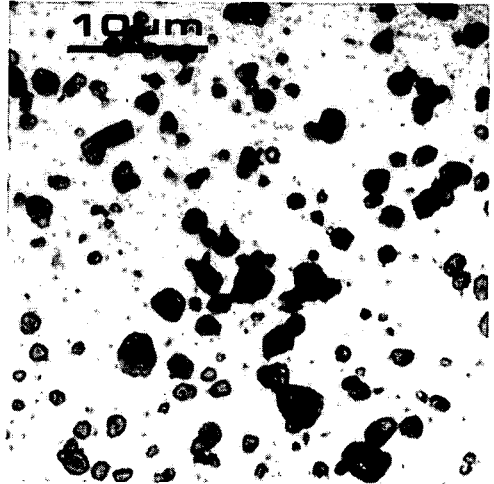


Fig. 14b.

Transverse section of extrudate from degassed AlSi ribbons. Canned, precompact AlSi (11.4 at% Si) ribbons extruded with an extrusion ratio of 25; optical micrograph. The degassing procedure implied a heat treatment of 5 h at 725 K. Note the coarser Si-rich phase particles, as compared to the specimen of Figure 14(a).

## 6. Conclusions

- (i) As compared to the extrusion of massive conventional castings, additional redundant work during quasi-static extrusion is required to achieve a coherent product from melt-spun ribbons.
- (ii) During extrusion the ribbons are stretched and aligned roughly parallel to the extrusion direction.
- (iii) The ratio of the ribbon thickness before extrusion to the ribbon thickness after extrusion is approximately equal to the square root of the extrusion ratio, as prescribed by the process of homogeneous deformation.
- (iv) Increases of tensile strengths of AlMg and AlSi extrudates, included by increasing alloying-element contents, are dominantly due to solid-solution and dispersion strengthening mechanisms respectively.
- (v) Intimate bonding between the ribbons by extrusion is less well obtained in consolidated AlMg ribbons than in consolidated AlSi ribbons. This is considered as a consequence of the difference in thickness of the oxide layers occurring at the surfaces of the ribbons.
- (vi) The tensile strength of consolidated AlMg ribbons is smaller than that of extruded conventional AlMg castings. This holds in particular for the transverse-tensile strength; see also conclusion (v).
- (vii) The tensile strength of consolidated AlSi ribbons can be significantly larger (up to 50%) than that of extruded conventional AlSi castings. This is ascribed to the smaller matrix-grain size and the finer dispersion of second-phase particles occurring in the consolidated ribbons.
- (viii) The tensile strength of consolidated, degassed (see conclusion (ix)) ribbons of pure Al is significantly larger than that of an extruded conventional pure Al casting. This is caused by the oxides at the ribbon boundaries (dispersion strengthening).
- (ix) Preheating before extrusion can replace a vacuum degassing procedure normally applied to precompacted billets of melt-spun ribbons. Improvement of (transverse) tensile strength as a result of degassing was only observed for consolidated melt-spun Al and AlSi alloys with small amounts of Si.
- (x) Vacuum degassing at high temperature leads to growth of matrix grains and/or precipitation and coarsening of second-phase particles. This has appreciably detrimental effects on tensile strengths.

## Acknowledgements

The authors are indebted to Professor B.M. Korevaar for stimulating discussions. Mr. P.F. Colijn assisted with the light-microscopical analysis. Financial support by the Foundation for Fundamental Research of Matter (FOM) is gratefully acknowledged.

## References

1. H. Jones, *J.Mater Sci.* 19(1984)1043.
2. R.E. Maringer, *SAMPE Q* 12(1980)30.
3. R.E. Maringer and C.E. Mobley in: "Rapid Solidification Processing"; Principles and Technologies, R. Mehrabian, B.H. Kear and M. Cohen (eds.), Proc.Int.Conf. on RSP, Reston, Virginia, USA, 1977, p. 208.
4. R. Delhez, L. Katgerman, Th.H. de Keijser, E.J. Mittemeijer, P. van Mourik, N.M. van der Pers, M. van Rooyen and W.E. Zalm, *Met. Powder Rep.* 38(1983)450.
5. S.J. Savage and F.H. Froes, *J.Metals* 36(1984)20.
6. A. Bendijk, R. Delhez, L. Katgerman, Th.H. de Keijser, E.J. Mittemeijer and N.M. van der Pers, *J.Mater.Sci.* 15(1980)2803.
7. R. Delhez, Th.H. de Keijser, E.J. Mittemeijer, P. van Mourik, N.M. van der Pers, L. Katgerman and W.E. Zalm, *J.Mater.Sci.* 17(1982)2887.
8. J.A. van der Hoeven, P. van Mourik and E.J. Mittemeijer, *J.Mater.Sci. Lett.* 2(1983)158.
9. M. van Rooyen, N.M. van der Pers, L. Katgerman, Th.H. de Keijser and E.J. Mittemeijer in "Proc. 5th Int. Conf. Rap. Quenched Metals", Würzburg, West-Germany; September 3-7, 1984, S. Steeb and H. Warlimont, eds., p. 823.
10. P. van Mourik, Th.H. de Keijser and E.J. Mittemeijer, *ibid*, p. 899
11. D.P. Vos, Research Report FB 79-34, DFVLR, Cologne (1979).
12. T. Sheppard and P.J.M. Chare, *Powder Metall.* 15(29)(1972)17.
13. J.T. Morgan, H.L. Gegel, S.M. Dovaivelu, L.E. Matson, I.A. Martorell and J.F. Thomas, Jr. in "High-Strength Powder Metallurgy Aluminium Alloys" edited by M.J. Koczak and G.J. Hildeman (TMS-AIME, 1982)p. 193.
14. H.G. Paris, J.W. Mullins and T.H. Sanders, Jr., *ibid*, p. 277.
15. J.P. Lyle and W.S. Cebulak, *Met.Trans.* 6A(1975)685.
16. M. Lebo and N.J. Grant, *Met.Trans.* 5(1974)1547.
17. J.P.H.A. Durand, R.M. Pelloux and N.J. Grant, *Mater.Sci.Eng.* 23(1976)247.
18. E.M. Modl-Onitsch, *Aluminium* 37(1961)724.
19. E.M. Modl-Onitsch, *Powder Metall.* 4(1959)120.
20. S.G. Roberts, AMMRC CTR 73-33, October, 1973.
21. T. Sheppard, *Met.Technol.* 8(1981)130.
22. J.N. Harris, "Mechanical working of metals", *Int.Ser. on Mat.Sci. and Technol.* vol. 36 (Pergamon Press, Oxford, 1983).
23. C.E. Mobley, A.H. Clauer and B.A. Wilcox, *J.Inst. Metals* 100(1972)142.
24. O. Hunderi and T. Save, *Scand.J. of Metallurgy* 10(1981)231.

# Morphology and mechanical properties of melt-spun and conventionally cast aluminium, AlMg and AlSi alloys before and after hot extrusion

M. VAN ROOYEN, P. F. COLIJN, TH. H. DE KEIJSER, E. J. MITTEMEIJER  
*Laboratory of Metallurgy, Delft University of Technology, Rotterdamseweg 137,  
2628 AL Delft, The Netherlands*

---

Rapidly solidified aluminium, AlMg (0 to 16.5 at% Mg) and AlSi (0 to 20.2 at% Si) alloys were produced by melt spinning. The AlMg ribbons were single-phase, whereas the AlSi ribbons were dual-phase. In the ribbons of both alloy systems the fineness of the microstructure increased with increasing alloying element content. The melt-spun ribbons were consolidated by hot extrusion. For comparison, conventionally cast alloys of corresponding compositions were extruded analogously. During the extrusion process in AlMg (16.5 at% Mg) and in the AlSi alloys precipitation occurred. The consolidation of the ribbons was markedly influenced by the oxide layer on the ribbon surfaces: in the AlSi consolidates a more intimate contact between the ribbons was apparent than in the aluminium and AlMg consolidates. In the extrudates of the conventionally cast alloys the grains and second-phase particles were much larger than in the consolidates. The observed dependence on alloy composition of hardness, ultimate tensile strength and elongation at fracture of both consolidated ribbons and extrudates of the conventionally cast alloys are discussed in terms of matrix grain size, solute content of the matrix, amount and size of second-phase particles and recrystallization behaviour. For all compositions of the alloys the Vickers hardness of the as-melt-spun ribbons was higher than that of the consolidated products, owing to recrystallization and precipitation provoked by the hot consolidation process. The ultimate tensile strength as well as the elongation at fracture of both consolidated ribbons and extruded conventionally cast alloys did not differ significantly for AlMg. However, due to a finer microstructure and a stronger inter-ribbon bonding, for AlSi alloys with a high silicon content the rapid solidification processing route did yield a product with significantly improved mechanical properties as compared with the extruded conventionally cast alloys.

---

## 1. Introduction

Although there is a strong and global interest in rapidly quenched metals, it has been stated recently [1]: "Unless some way is found of effectively forcing the practical aspects . . . eventually rapid quenching research will die away and its bright promise will be denied". In particular, an investigation into possible applications of rapidly solidified *crystalline* alloys is desired.

This paper deals with metastable crystalline liquid-quenched (melt-spun) AlMg and AlSi alloys before and after compaction by hot extrusion. The morphology and mechanical properties have been studied and compared with those of conventionally cast alloys.

Various strengthening mechanisms can be utilized to improve the mechanical properties of metallic materials [2]. Commonly one distinguishes

- (a) work hardening,
- (b) strengthening from grain refinement,
- (c) solid-solution hardening,
- (d) precipitation or age-hardening and
- (e) dispersion hardening.

By rapid quenching from the melt, aluminium alloys can be obtained which exhibit, as compared to conventionally cast alloys [3, 4],

- (a) decreased grain size,
- (b) increased chemical homogeneity,
- (c) enhanced supersaturation of alloying elements and vacancies and
- (d) retention/appearance of non-equilibrium crystal structures.

Hence, with reference to the strengthening mechanisms mentioned, rapid-solidification technology can be applied to the production of materials with improved mechanical properties. However, rapid quenching unavoidably leads to (half) products which are small in at least one dimension. Consequently, the utilization of liquid-quenched materials requires a consolidation process after solidification. Such a process implies mechanical and/or thermal treatment, which may cause deterioration of initially useful properties of the material.

Hot extrusion is a frequently applied compaction process. Then, in advance, a number of operations can be carried out in succession:

- (a) precompaction (to avoid an excessively large extrusion chamber),
- (b) degassing (occasionally necessary to prevent development of hydrogen from adsorbed water) and
- (c) preheating.

The extrusion process is controlled by many parameters; the most important are

- (a) extrusion ratio,
- (b) working temperature,
- (c) speed of deformation (ram speed) and
- (d) frictional conditions at the die and container wall.

A discussion of the pretreatments and the extrusion process itself can be found elsewhere [5, 6].

The behaviour of the oxide layer on the ribbon surfaces during the deformation process is of crucial significance for the quality of the final product. In the case of an ideal consolidation the oxide layers are broken up and the oxide particles are finely dispersed in the compact. This causes a strengthening effect [5]. The degree of dispersion obtained depends on the adherence of the oxide layer to the ribbon surface; too high a bond strength leads to an insufficient breaking-up of the layer. This prevents intimate contact between ribbons and diffusion welding across the boundaries is impeded; a strong anisotropy of the mechanical properties will result.

Hot working accelerates diffusion and recovery/recrystallization processes. These processes affect the structure and mechanical properties of the extrudates.

It is well understood that more complicated multi-component (aluminium-base) alloys may show properties appropriate for special applications (e.g. [7]). However, until now, the rationale for understanding the relation between treatment and properties is

generally lacking, and optimization is pursued in an empirical way. In the present research project binary AlMg and AlSi alloys have been chosen as model systems. These alloy systems allow evaluation of the effectiveness of solid-solution strengthening and dispersion strengthening in rapid-solidification processing.

## 2. Experimental details

### 2.1. Production and processing of melt-spun ribbons

Melt-spun ribbons (thickness 25 to 50  $\mu\text{m}$ , width about 2 mm, cooling rate about  $10^6 \text{ K sec}^{-1}$ ) were prepared from pure aluminium, AlMg (2.6, 3.2, 5.6, 11.2 and 16.5 at % Mg) and AlSi (1.1, 2.4, 4.6, 7.2, 11.4 and 20.2 at % Si) using aluminium (99.998 wt %), magnesium (99.38 wt %) and silicon (99.99 wt %).

Extrusion was performed at about 675 K for the AlMg alloys and at about 725 K for aluminium and the AlSi alloys, employing a preheating time of about 40 min. The extrusion ratio was 25 and the extrusion speed was about  $1 \text{ m min}^{-1}$  (when taking into account the associated densification this corresponds to a ram speed of about  $7 \text{ cm min}^{-1}$ ).

For comparison, conventionally cast aluminium and alloys of corresponding compositions (AlMg: 3.2, 5.8, 11.2 and 17.0 at % Mg; AlSi: 1.0, 2.3, 4.4, 8.0, 10.9, 14.4 and 19.0 at % Si) were extruded under identical conditions. For further details (melt-spinning equipment, precompaction and canning) see van Rooyen *et al.* [5].

### 2.2. Microscopy

Light microscopy (phase and interference contrast, conical illumination and bright field) was performed on longitudinal sections of the ribbons and on both longitudinal and transverse sections of the extrudates, using a Neophot-2 microscope (Carl Zeiss, Jena). Depending on the type of alloy the specimens were etched with Keller and Wilcox's reagent or electrolytically polished (Bath D2, Struers).

Scanning electron microscopy was applied using a JEOL JXA 50A instrument.

Transmission electron microscopy was performed with a Philips EM400 apparatus. Thin electron-transparent regions of the ribbons were investigated. Samples taken from the extruded bars were jet-electropolished (in a bath of 20% perchloric acid and 80% ethanol) before examination in the microscope.

### 2.3. X-ray diffraction

Lattice parameter determinations were performed using the Debye-Scherrer technique. For details see Mittemeijer *et al.* [8].

TABLE 1 Alloying-element (silicon) content of liquid-quenched AlSi alloys. Gross content determined by chemical analysis; dissolved content determined by lattice-parameter measurements

Gross content (at %)	In solid solution (at %)
1.1	0.9
2.4	1.2
4.6	1.2
7.2	2.0
11.4	2.7
20.2	2.3

#### 2.4. Hardness measurements

Hardness measurements were performed according to DIN 50133 applying a Leitz Durimet micro-Vickers hardness tester. The hardness measurements were carried out on longitudinal sections. To obtain reliable hardness values the distance between the centre of the indentation and the nearest edge of the specimen should be at least 2.5 times the average length of the diagonals of the diamond indentation. Therefore, when testing sections of the thin ribbons, a load of only 10g was applied. Consolidates of aluminium, AlMg and AlSi alloys were tested on longitudinal sections of the extruded bars using loads of 50 and 25 g respectively.

#### 2.5. Tensile testing

After removal by machining of the canning material from the extruded bars, specimens were prepared for tensile testing. The (longitudinal) tensile specimens were prepared according to DIN 50125 with a length/diameter ratio of 10. At least four specimens of each alloy were tested on an Instron tensile-testing machine (Model TTCML MI 1.4.6.).

### 3. Results and discussion

In a preceding paper [5] attention was paid to the extrusion process itself, including a (geometric) description of the bonding, stretching and alignment of the

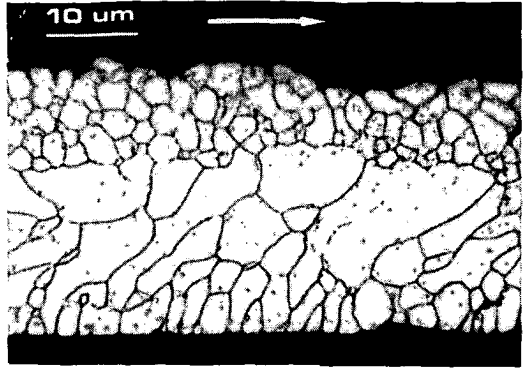


Figure 2 Longitudinal section of an AlMg (11.2 at % Mg) ribbon (etched with Keller and Wilcox's reagent; optical micrograph: bright field). Arrow indicates spinning direction.

ribbons. Further, the benefits of an (in practice costly) degassing procedure (see Introduction) were examined. It was found that, under the present conditions, the preheating procedure applied was sufficient to obtain a sound product. An additional degassing in fact led to deterioration of the mechanical properties [5]. Therefore, in this paper results are reported only on undegassed materials.

#### 3.1. Composition of ribbons and extrudates

The melt-spun AlMg ribbons were single-phase: all magnesium was in solid solution. However, the melt-spun AlSi ribbons were dual-phase (see Table 1 for the amount of silicon dissolved in the aluminium matrix). From a theoretical point of view it can be expected that the critical cooling rate above which the alloy solidifies as a single phase is higher for AlSi than for AlMg [9].

In the extruded AlMg alloys (both melt-spun and conventionally cast) with about 3 and 5 at % Mg, no

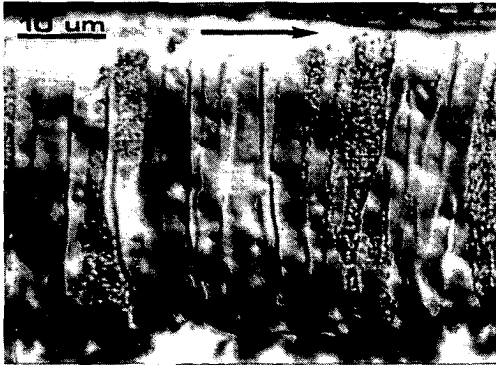


Figure 1 Longitudinal section of a pure aluminium ribbon (electrolytically polished; optical micrograph with interference contrast). Arrow indicates spinning direction.

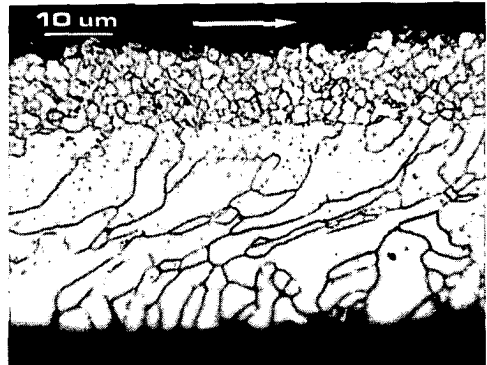


Figure 3 Longitudinal section of an AlMg (16.5 at % Mg) ribbon (etched with Keller and Wilcox's reagent; optical micrograph: bright field). Arrow indicates spinning direction.

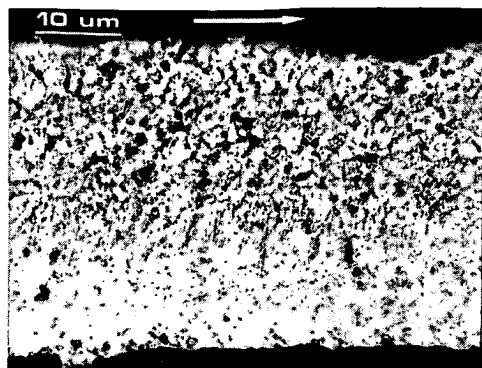


Figure 4 Longitudinal section of an AlSi (7.2 at % Si) ribbon (etched with Keller and Wilcox's reagent; optical micrograph: conical illumination). Arrow indicates spinning direction. Note zone of ultrafine columns in central region of the section.

trace of a second phase could be found. Optical micrographs of extrudates of AlMg alloys with about 11 at % Mg clearly showed small precipitates at grain boundaries (e.g. Figs 9c and 11c below). These grain-boundary precipitates are thought to develop during cooling of the extruded bars. In all extrudates of the 16.5 at % Mg alloy a homogeneous precipitation was observed by optical microscopy (see Fig. 9d below). X-ray diffraction demonstrated the presence of the  $\beta$  phase (about  $\text{Al}_3\text{Mg}_5$ ). According to the phase diagram and the extrusion temperature applied for this alloy, the  $\beta$  phase already starts to precipitate during extrusion.

The aluminium-rich matrix of the AlSi extrudates of both melt-spun and conventionally cast materials contained a small amount of dissolved silicon (about 0.5 at %). Apparently, at the extrusion temperature, precipitation had occurred until the equilibrium solubility was reached.

### 3.2. Morphology of the melt-spun ribbons

Typical examples are shown in Figs 1 to 4. In general, three zones can be discerned in the ribbons:

(i) Chill zone. Obviously, the highest cooling and solidification rates occur at the wheel side. This leads to very small crystallites in this region (showing sometimes an even "featureless" light-microscopical

appearance) and the largest amount of dissolved alloying element (e.g. [10, 11]). Also, the structural imperfection as determined by X-ray diffraction line-broadening analysis is largest in the chill zone [12]. Further, the nearby presence of the heat sink induces a local thermal gradient perpendicular to the wheel surface, and this serves to explain an initial development of grain boundaries in the direction of the wheel-surface normal (Fig. 2).

(ii) Columnar grain zone. The unidirectional heat flow condition in the puddle leads to columnar grains. It has been shown [13, 14] that with respect to the spinning direction, the thermal gradient in the puddle has an inclination in the reverse direction whereas near the solid-liquid interface the gradient of constitutional undercooling has a forward inclination. This could explain the occurrence of columns inclined forward with respect to the spinning direction. This is supported by Figs 1 to 3: in the case of (almost pure) aluminium there is (almost) no constitutional undercooling and therefore (almost) no column inclination, whereas for the AlMg ribbons the inclination increases with increasing magnesium content (i.e. increasing width of the solidus-liquidus gap). This columnar zone is also present in the AlSi ribbons, but can hardly be recognized because of the ultrafine grains (Fig. 4).

(iii) Equiaxed grain zone. The presence of equiaxed crystallites in the top layer is ascribed to a relatively slow heat transfer. This leads to nucleation in the liquid. In combination with convection in the liquid, equiaxed grains develop which are randomly oriented. Consistent with this conception, Fig. 5 shows that a slow heat transfer (because of an air bubble between the ribbon and the cooling wheel) indeed leads to a relatively thick layer of equiaxed crystallites.

Constitutional undercooling will also play an important role in the formation of the top layer of equiaxed crystallites [10]. Within this context Fig. 1 serves as an additional indication: in pure aluminium no constitutional undercooling occurs, and no top layer of equiaxed grains is observed.

The solidification history of melt-spun ribbons, showing the three-zone morphology, implies that segregation of alloying elements occurs in particular in the central region. This was demonstrated recently [10].



Figure 5 Longitudinal section of an AlMg (16.5 at % Mg) ribbon (electrolytically polished; optical micrograph: bright field). At the location where an air bubble was enclosed (arrow) between ribbon and wheel, the chill zone is absent.

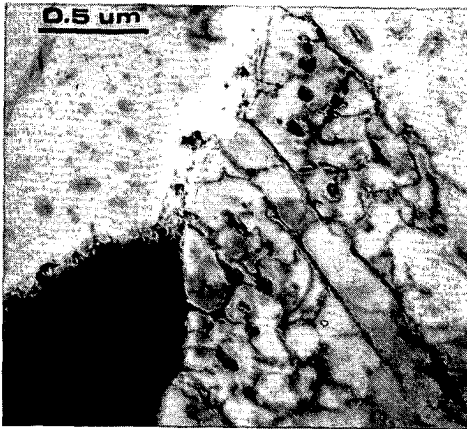


Figure 6 Transmission electron micrograph (bright field) of an AlSi (4.6 at % Si) ribbon, viewed in the direction of the surface normal. Note the small silicon particles.

The increased fineness of microstructure, the increase of the amount of randomly oriented crystallites and the decrease of distinctness of preferred orientation with increasing alloying element content can be due to the hindrance of preferred growth by micro-segregation (AlMg) and/or second-phase particles (AlSi), both at grain boundaries.

The microstructure of the AlSi ribbons is much finer than that of the AlMg ribbons (cf. Figs 2 and 4): the second-phase silicon particles are very effective structure refiners (see also Fig. 6).

### 3.3. Morphology of the extrudates

#### 3.3.1. Aluminium

Optical and transmission electron micrographs of extruded pure aluminium ribbons are shown in Figs 7a and b, respectively. Under the present conditions of extruding aluminium ribbons, the oxide layer, originally present on the ribbon surfaces, remains more or less intact (Figs 7a and b). The slightly fragmented oxide layer hinders intimate contact between the metallic bodies of the ribbons during extrusion. As a result, grain-boundary migration rarely occurred across the ribbon interfaces. In later stages of grain growth the grain boundaries within the ribbons extended from ribbon interface to ribbon interface and advanced in lateral directions (Fig. 7a).

As indicated by the oxide layers at the ribbon interfaces, during extrusion the ribbons are stretched and aligned roughly parallel to the extrusion direction (Fig. 7a, see also van Rooyen *et al.* [5]).

The oxide-layer barrier to grain growth is obviously absent for the conventionally cast aluminium, and hence very large crystals develop (Fig. 8; note the difference in magnification between Figs 7a and 8). It can reasonably be expected that on hot extrusion of both melt-spun and conventionally cast aluminium dynamic recovery occurs [15], and thus the observed recrystallization/grain growth was dominant during cooling after extrusion.

#### 3.3.2. Aluminium-magnesium

Micrographs of extruded AlMg ribbons are shown in Figs 9a to d. As compared to extruded ribbons of pure aluminium, AlMg has thicker oxide layers at the ribbon interfaces: electron microprobe analyses showed that at these locations a large amount of oxygen is present and that the Mg/Al ratio is significantly larger

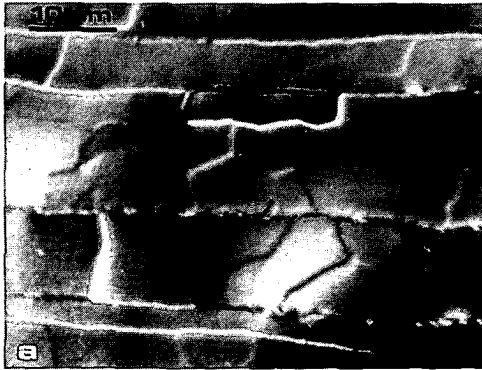


Figure 7 (a) Longitudinal section of consolidate of pure aluminium ribbons (electrolytically polished; optical micrograph: interference contrast). (b) Transmission electron micrograph (bright field) of consolidate of pure aluminium ribbons. Arrows indicate oxide layer.

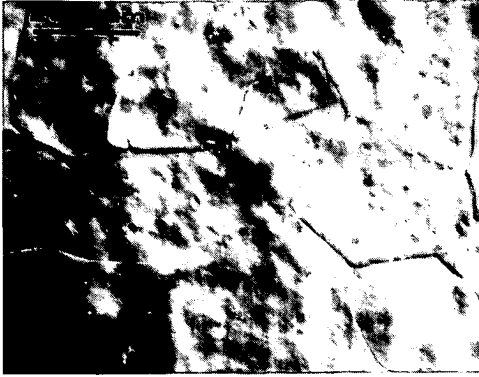


Figure 8 Longitudinal section of extruded conventionally cast pure aluminum (electrolytically polished; optical micrograph: interference contrast).

than in the bulk. (In view of the oxide layer thickness and the microprobe spot size only semi-quantitative analyses were possible.) The latter observation agrees with results obtained in an investigation of the oxidation of conventionally cast aluminum alloys [16]. It can be concluded that during extrusion of AlMg ribbons no sufficient fragmentation of oxide layers occurred to establish a predominantly metallic contact between the ribbons.

In particular, for magnesium contents larger than about 3at% dynamic recrystallization occurred during extrusion (a further discussion is given in Section 3.4.1.2.). The grain growth was generally restricted to within the (former) ribbon surfaces, as a consequence of the presence of the oxide layers. Grain growth is retarded by the solute-drag effect: the larger the amount of magnesium atoms dissolved, the smaller the final grain size (Figs 9a to d). This distinct effect is also clearly apparent in the microstructures of the extruded conventionally cast alloys (Figs 10a to d). In the latter case the grain growth is obviously not impeded by oxide layers.

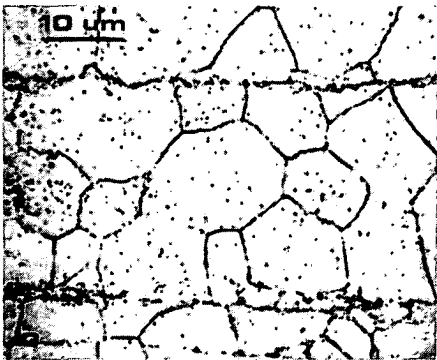
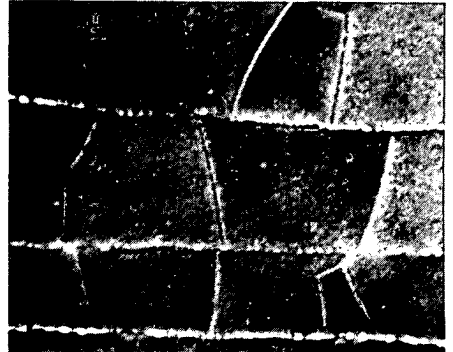
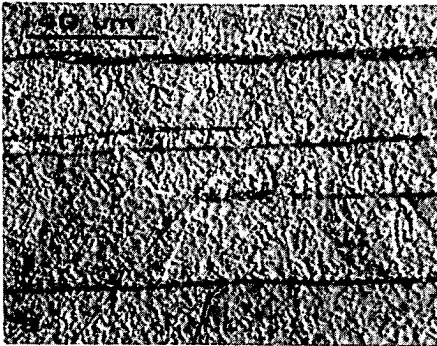


Figure 9 Longitudinal sections of consolidates of AlMg ribbons. (a) 2.6 at% Mg; etched with Keller and Wilcox's reagent; optical micrograph: interference contrast. (b) 5.6 at% Mg; electrolytically polished; scanning electron micrograph. (c) 11.2 at% Mg; etched with Keller and Wilcox's reagent; optical micrograph: conical illumination. (d) 16.5 at% Mg; electrolytically polished; optical micrograph: interference contrast.

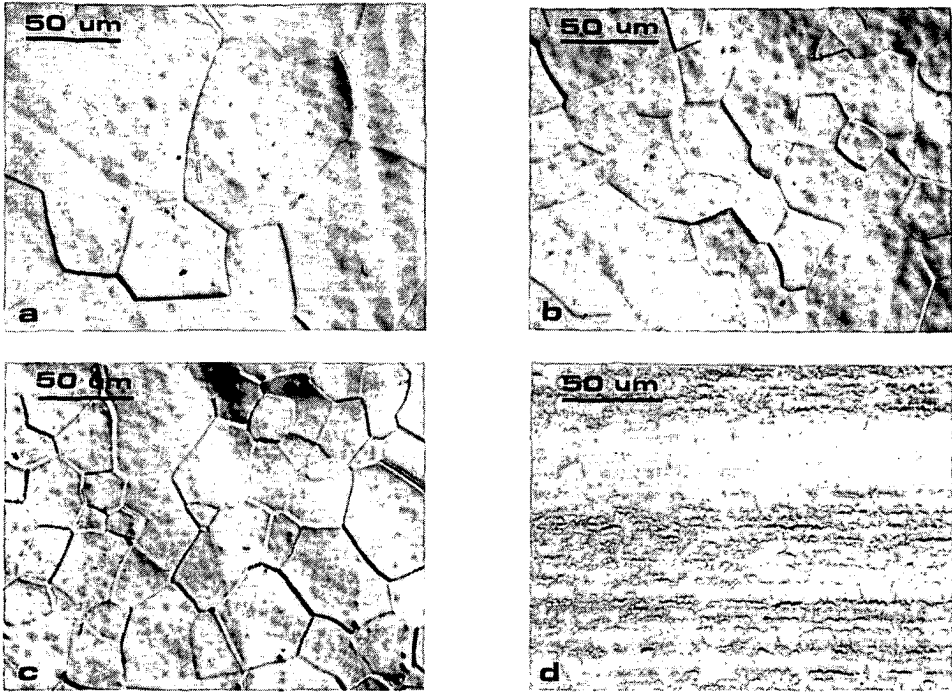


Figure 10 Longitudinal sections of extruded conventionally cast AlMg alloys. (a) 3.2 at % Mg; electrolytically polished; optical micrograph: interference contrast. (b) 5.8 at % Mg; electrolytically polished; optical micrograph: interference contrast. (c) 11.2 at % Mg; electrolytically polished; optical micrograph: interference contrast. (d) 17.0 at % Mg; electrolytically polished; optical micrograph: interference contrast.



Figure 11 Transmission electron micrograph (bright field) of consolidate of AlMg (3.2 at % Mg) ribbons. Note contrast due to dislocations.

The development of numerous second-phase particles during extrusion of the AlMg (16.5 at % Mg) alloy (see Section 3.1) provides an additional grain-growth impeding factor as evidenced by a comparison of grain-size differences between Figs 10a to c and Fig. 10d.

In contrast with the aluminium ribbons, the AlMg ribbons exhibit after extrusion more X-ray diffraction line-broadening (Debye-Scherrer photographs) than before. This corresponds with the presence of many deformation-induced dislocations (cf. Fig. 11 and Fig. 7b). The dissolved magnesium atoms form effective obstacles to dislocation movement.

### 3.3.3. Aluminium-silicon

Micrographs of extruded AlSi ribbons are shown in Figs 12a to d. As in the case of the ribbons, all extrudates are dual-phase: silicon particles at grain boundaries and within grains of the aluminium matrix are clearly visible (see also Fig. 13). With reference to

the melt-spun ribbons, the size of the silicon particles in the extrudates is much larger (cf. Figs 6 and 13). Ribbon interfaces are only slightly visible after etching, implying that, as compared with the AlMg alloys, a much more intimate contact between the ribbons was established by extrusion. (In this connection it can be remarked that oxidation of AlMg leads to porous, thick oxide layers, whereas oxidation of AlSi results in seclusive, thin oxide layers [16].) Furthermore, the grain size of the AlSi consolidates decreases with increasing silicon content and is much smaller than that of the AlMg consolidates. This result can be ascribed to grain-boundary pinning by second-phase particles during extrusion, whereas the AlMg alloys were single-phase during extrusion (except the AlMg (16.5 at % Mg) alloy).

Obviously, the matrix grain sizes and the second-phase particles are much larger for the extruded conventionally cast than for the extruded liquid-quenched AlSi alloys (Figs 14a to d). In the conventionally cast AlSi (20.2 at % Si) alloy, very large faceted primary silicon particles are present (Fig. 14d). During the deformation process the interaction between these relatively hard and brittle particles and the relatively soft and ductile matrix can lead to porosity at the interfaces, as can be seen in Figs 14d and 15.

### 3.4. Mechanical properties

#### 3.4.1. Aluminium–magnesium

*3.4.1.1. Hardness.* The hardness of the melt-spun AlMg ribbons as a function of magnesium content is presented in Fig. 16. All magnesium is in solid solution after liquid quenching (Section 3.1). Hence, the increase of hardness with increasing magnesium content can be ascribed to solid-solution strengthening. Guinier–Preston (GP) zone formation during ageing at room temperature can contribute to the enhanced hardness increase observed for the AlMg (16.5 at % Mg) alloy. This GP-zone formation occurs significantly for magnesium contents larger than about 10 at % [17].

The increase of the flow stress,  $\Delta\tau$ , due to misfitting solute atoms, can be represented [18] by

$$\Delta\tau = \frac{1}{4}\mu\varepsilon C^{1/2}$$

where  $\mu$  = shear modulus,  $\varepsilon$  = linear misfit parameter and  $C$  = solute atom concentration. The hardness is proportional to the flow stress [19]. Then, in the case of solid-solution hardening, a linear relation would occur between hardness increase and the square root of solute atom concentration. This is indeed observed for the AlMg ribbons, where no significant GP-zone formation occurred (Fig. 17). The deviation observed for the AlMg (16.5 at % Mg) alloy can be due to the presence of GP zones (see above discussion).

The AlMg ribbon extrudates are dominantly single-phase, except for the AlMg (16.5 at % Mg) alloy (see Section 3.1). Thus solid-solution strengthening again explains the hardness increase observed on alloying (Fig. 16). However, as compared with the liquid-quenched state, the pronounced increase of grain size provoked by extrusion (cf. Figs 2 and 9c) leads to a general decrease of hardness (Fig. 16). This hardness decrease is most pronounced for the AlMg (16.5 at % Mg) alloy, which is attributed to the precipitation of (coarse)  $\beta$  particles in (only) this alloy during extrusion (cf. Figs 3 and 9d).

*3.4.1.2. Tensile properties of extrudates.* The ultimate tensile strength as a function of magnesium content is shown in Fig. 18. In accordance with the discussion in Sections 3.1 and 3.3 the initial increase in tensile strength is ascribed to solid-solution strengthening. At higher magnesium contents, precipitation of  $\beta$  particles at (former) ribbon/grain boundaries (Fig. 9d) affects the tensile strength. As discussed in Section 3.3.2, hardly any grain growth across the original ribbon surfaces had occurred, implying an insufficient bonding of the constituents in the consolidated product. As a consequence the tensile strength of the consolidated ribbons is not better (and in transverse directions even worse [5]) than that of the extruded conventional castings (Fig. 18).

The elongation at fracture is presented in Fig. 19 as a function of magnesium content. Initially, the elongation decreases with increasing magnesium content and a minimum occurs at about 3 at % Mg. For larger magnesium contents the elongation increases, reaches a plateau value, and eventually declines rapidly. This peculiar behaviour may be explained as follows. In pure aluminium, recovery processes occur during hot extrusion (dynamic recovery). This has been ascribed to a high stacking-fault energy [15]. As a result a relatively high ductility is observed. Indications exist that alloying with magnesium lowers the stacking-fault energy [20] (but see discussion in Sheppard *et al.* [21]). It can then be anticipated that a less pronounced recovery occurs during extrusion (compare Figs 11 and 7b). Consequently, the ductility after hot extrusion continuously decreases with increasing magnesium content. Apparently the decrease of grain size on alloying with magnesium compensated only partly for this effect. Ultimately, on increasing the magnesium content, dynamic recrystallization is provoked which corresponds with an increase of the ductility. The appearance of  $\beta$  particles at ribbon/grain boundaries after extrusion at high magnesium contents is obviously accompanied by a low ductility.

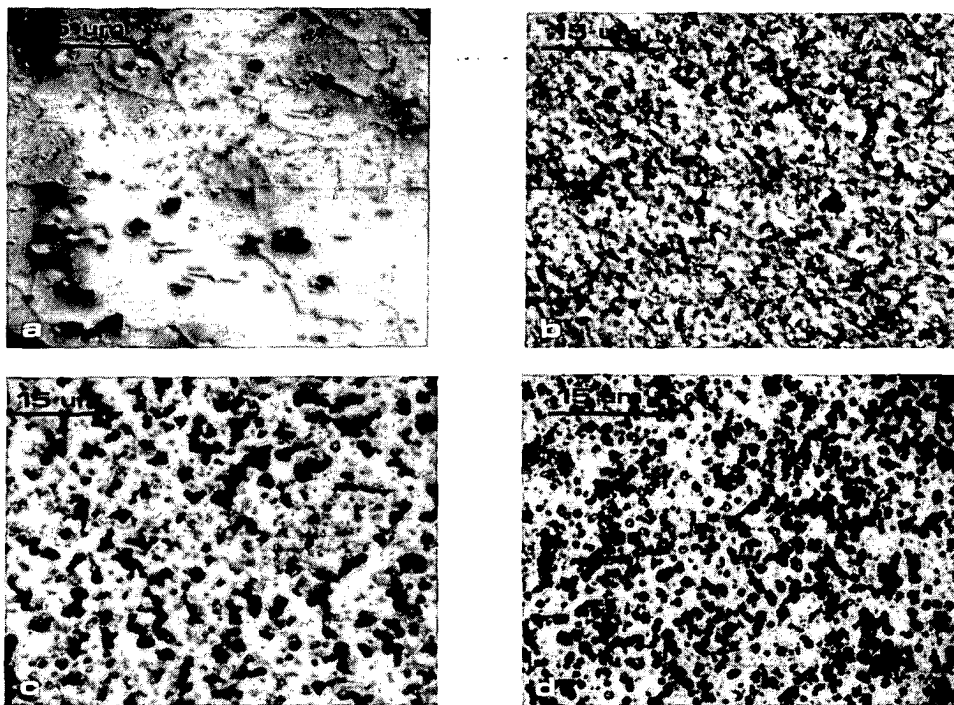


Figure 12 Longitudinal sections of consolidates of AlSi ribbons. (a) 1.1 at % Si; electrolytically polished and subsequently etched with Keller and Wilcox's reagent; optical micrograph: interference contrast. (b) 4.6 at % Si; electrolytically polished and subsequently etched with Keller and Wilcox's reagent; optical micrograph: interference contrast. (c) 11.4 at % Si; electrolytically polished and subsequently etched with Keller and Wilcox's reagent; optical micrograph: interference contrast. (d) 20.2 at % Si; unetched; optical micrograph: conical illumination.

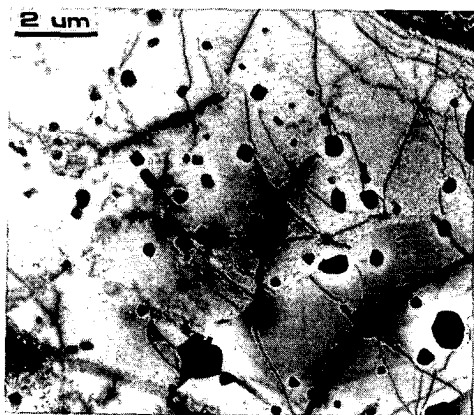


Figure 13 Transmission electron micrograph (bright field) of consolidate of AlSi (1.3 at % Si) ribbons.

### 3.4.2. Aluminium-silicon

3.4.2.1. *Hardness.* All AlSi ribbons are dual-phase after liquid quenching. The maximal amount of dissolved silicon occurs at about the eutectic composition (Table I and Bendijk *et al.* [11]). Both solid-solution and dispersion strengthening mechanisms explain the hardness increase observed on alloying with silicon, with a relatively important contribution of solid-solution strengthening for the lower silicon contents (Fig. 20).

For ribbon extrudates, the amount of silicon dissolved in the aluminium matrix is approximately equal to the maximal amount dissolved in equilibrium at the preheat temperature (equal to about 0.5 at % Si; see Section 3.1.). Consequently, as compared with the liquid-quenched state, the contribution of solid-solution strengthening to the observed hardening is much smaller. Further, a coarsening of the dual-phase

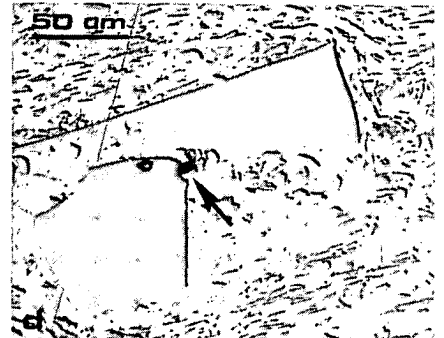
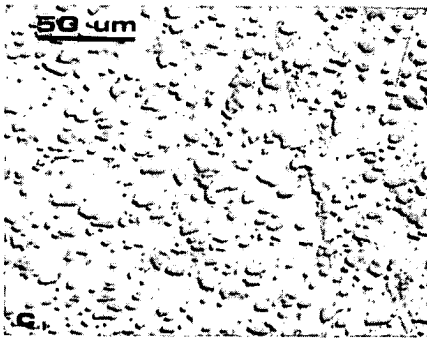
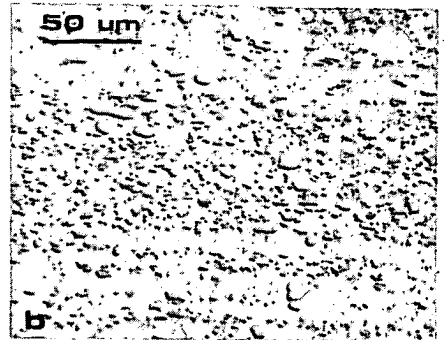
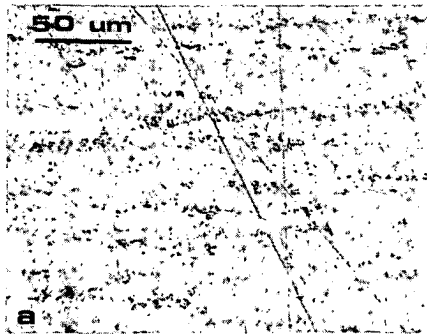


Figure 14 Longitudinal sections of extruded conventionally cast AlSi alloys. (a) 2.3 at % Si; etched with Keller and Wilcox's reagent; optical micrograph: interference contrast. (b) 8.0 at % Si; etched with Keller and Wilcox's reagent; optical micrograph: interference contrast. (c) 14.4 at % Si; etched with Keller and Wilcox's reagent; optical micrograph: interference contrast. (d) 19.0 at % Si; etched with Keller and Wilcox's reagent; optical micrograph: interference contrast. Arrow indicates void; see also Fig. 15.

microstructure is induced by extrusion (cf. Figs 6 and 12b). Both effects serve to explain the general decrease of hardness observed after extrusion (Fig. 20).

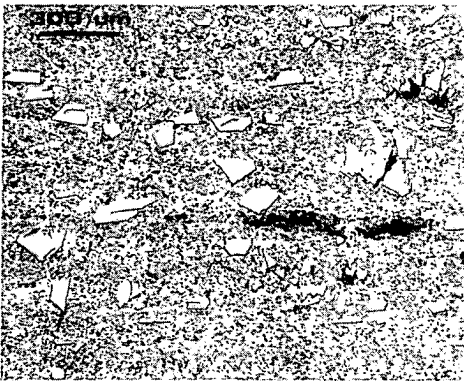


Figure 15 Longitudinal section of extruded conventionally cast AlSi (19.0 at % Si) alloy (etched with Keller and Wilcox's reagent; optical micrograph: interference contrast). Note the porosity.

3.4.2.2. *Tensile properties of extrudates.* The ultimate tensile strength is shown in Fig. 21 as a function of silicon content. As discussed above for the dependence of hardness on silicon content, strengthening in the AlSi extrudates mainly stems from the dispersed silicon phase; only 0.5 at % Si is dissolved in the matrix after

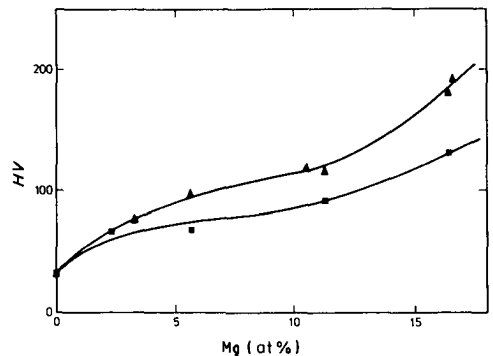


Figure 16 Microhardness of (▲) ribbons and (■) consolidates of AlMg as a function of gross magnesium content.

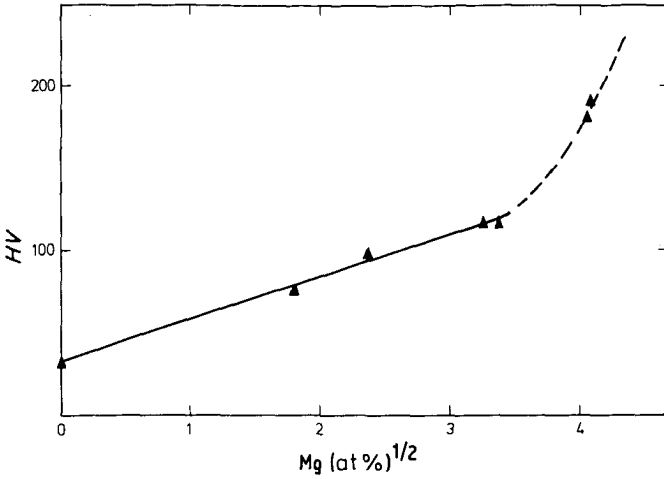


Figure 17 Microhardness of AlMg ribbons as a function of square root of gross magnesium content.

extrusion. In contrast with the AlMg extrudates, for the AlSi extrudates (in particular those with a high silicon content) the tensile strength of extruded ribbons is significantly larger (up to 50%) than that of extruded conventionally cast material. This difference between AlMg and AlSi extrudates originates (see Section 3.3.3.) from

(i) the moderate coarsening of the AlSi microstructure on extrusion, where the final microstructure of the AlSi extrudates is much finer for the ribbon material than for the conventionally cast material (cf. Figs 12d

and 14d; note the difference of magnification); and  
 (ii) a strong bonding between the consolidated ribbons.

The elongation at fracture of the consolidated materials decreased on alloying with silicon. The elongations at about 20 at % Si were 12 and 4% for the extruded ribbons and the extruded conventionally cast materials, respectively. This difference, too, can be considered as a result of the relatively small grain size occurring in the consolidated ribbon material (see above).

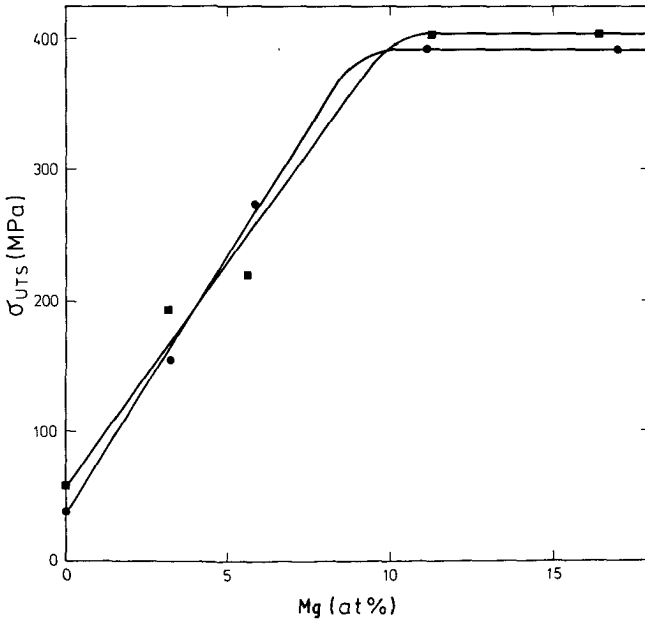


Figure 18 Ultimate tensile strength,  $\sigma_{UTS}$ , of (■) consolidated ribbons and (●) extruded conventional castings of AlMg as a function of gross magnesium content.

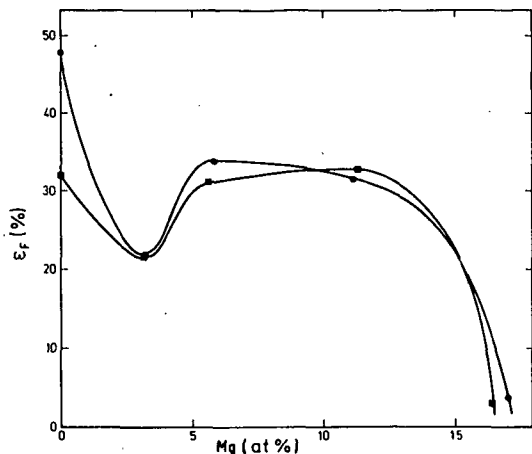


Figure 19 Elongation at fracture,  $\epsilon_F$ , of (■) consolidated ribbons and (●) extruded conventional castings of AlMg as a function of gross magnesium content.

## 4. Conclusions

### 4.1. Composition

1. In the as-liquid-quenched condition the AlMg alloys were single-phase, whereas the AlSi alloys were dual-phase.

2. After consolidation the composition of the aluminium-rich phase of the AlMg and AlSi ribbon material corresponded with the equilibrium solid solubility of the alloying element at the extrusion temperature.

3. Oxide layers at the ribbon surfaces were more pronounced for AlMg than for AlSi.

### 4.2. Morphology

1. As a combined result of heat-flow conditions and constitutional undercooling, in general the melt-spun alloys exhibited a three-zone morphology.

2. On extruding ribbon material, coarsening of the microstructure occurred with the growth of grains (AlMg and AlSi) and second-phase particles (AlSi). Grain growth was restricted mainly to within the original ribbon surfaces.

3. The microstructure became finer with increasing alloying-element content. This can be ascribed to solute-drag effects (in particular for AlMg) and the pinning of grain boundaries by second-phase particles (in particular for AlSi).

4. Second-phase particles as in AlSi are very effective structure refiners.

5. The microstructure of extruded ribbon material was much finer than that of extruded conventionally cast material of corresponding composition.

### 4.3. Hardness

1. The hardness of the AlMg ribbon material increased with increasing magnesium content as a result of solid-solution strengthening, implying a linear relation between the hardness and the square root of solute-atom concentration. The extrusion-induced increase of grain size contributed to a significant decrease in hardness.

2. The hardness of the AlSi ribbon material increased with silicon content as a result of both dispersion strengthening and solid-solution strengthening. The extrusion-induced increase of grain size and the progress of precipitation/coarsening of the second phase contributed to a drastic decrease in hardness.

### 4.4. Tensile properties

1. The increase of the tensile strength of consolidated AlMg and AlSi ribbon material with increasing alloying-element content is predominantly caused by solid-solution and dispersion strengthening respectively.

2. Relatively thick oxide layers (as with AlMg) hinder an intimate metallic contact between ribbons on extruding, which affects the tensile strength.

3. The decrease and subsequent increase of the elongation at fracture on increasing the alloying-element content in extruded AlMg alloys is ascribed to the predominance of either dynamic recovery (below about 3 at % Mg) or dynamic recrystallization (above about 3 at % Mg).

4. In contrast to the extruded AlMg ribbon material, the tensile strength of extruded AlSi ribbon material was significantly larger than that of extruded conventionally cast material of corresponding composition. This difference was most pronounced at higher amounts of alloying element (tensile-strength improvement of 50% at about 20 at % Si).

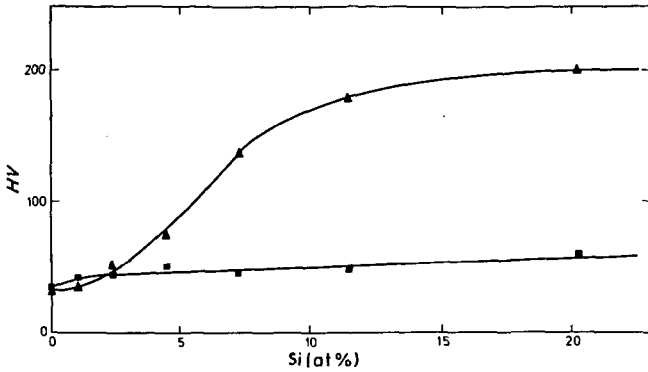


Figure 20 Microhardness of (▲) ribbons and (■) consolidates of AlSi as a function of gross silicon content.

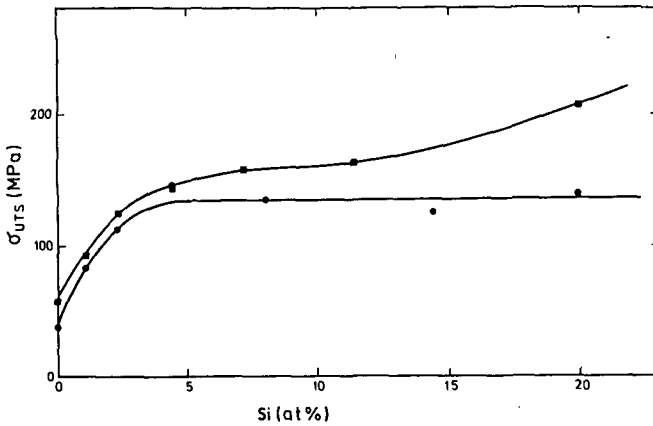


Figure 21 Ultimate tensile strength,  $\sigma_{UTS}$ , of (■) consolidated ribbons and (●) extruded conventional castings of AlSi as a function of gross silicon content.

### Acknowledgements

The authors are indebted to Professor B. M. Korevaar for stimulating discussions. Ir. P. van Mourik performed the X-ray diffraction lattice parameter determinations, Mr C. D. de Haan carried out the transmission electron microscopy and Mr D. P. Nelemans did the scanning electron microscopy and electron-microprobe analysis. Financial support by the Foundation for Fundamental Research of Matter (FOM) is gratefully acknowledged.

### References

1. R. W. CAHN, *Int. J. Rap. Sol.* **1** (1984) 81.
2. G. E. DIETER, "Mechanical Metallurgy" (McGraw-Hill, London, 1976) Ch. 5.
3. H. JONES, *J. Mater. Sci.* **19** (1984) 1043.
4. R. E. MARINGER, *SAMPE Q.* **12** (1980) 30.
5. M. VAN ROOYEN, J. A. VAN DER HOEVEN, L. KATGERMAN, P. VAN MOURIK, TH. H. DE KEIJSER and E. J. MITTEMEIJER, in Proceedings of the P.M. Aerospace Materials Conference, Berne (Switzerland), November 1984, Vol. 1, edited by Metal Powder Report, p. 341.
6. T. SHEPPARD, *Met. Technol.* **8** (1981) 130.
7. Proceedings of P.M. Aerospace Materials Conference, Berne (Switzerland), November 1984, Vols. 1 and 2, edited by Metal Powder Report.
8. E. J. MITTEMEIJER, P. VAN MOURIK and TH. H. DE KEIJSER, *Phil. Mag.* **43A** (1981) 1157.
9. L. KATGERMAN, *Scripta Metall.* **17** (1983) 537.
10. J. A. VAN DER HOEVEN, P. VAN MOURIK and E. J. MITTEMEIJER, *J. Mater. Sci. Lett.* **2** (1983) 158.
11. A. BENDIJK, R. DELHEZ, L. KATGERMAN, TH. H. DE KEIJSER, E. J. MITTEMEIJER and N. M. VAN DER PERS, *J. Mater. Sci.* **15** (1980) 2803.
12. R. DELHEZ, TH. H. DE KEIJSER, E. J. MITTEMEIJER, P. VAN MOURIK, N. M. VAN DER PERS, L. KATGERMAN and W. E. ZALM, *ibid.* **17** (1982) 2887.
13. K. TAKESHITA and P. H. SHINGU, *Trans. Jpn. Inst. Met.* **24** (1983) 529.
14. L. KATGERMAN, in Proceedings of 5th International Conference Rapidly Quenched Metals, Würzburg, September 1984, p. 819.
15. H. J. McQUEEN, *J. Metals* **32** (1980) 2.
16. H. J. VAN BEEK, MSc thesis, Delft University of Technology (1984).
17. J. A. SINTE MAARTENSDIJK, MSc thesis, Delft University of Technology (1985).
18. P. M. KELLY, *J. Aust. Inst. Metals* **16** (1971) 104.
19. J. R. CAHOON, W. H. BROUGHTON and A. R. KUTZAK, *Metall. Trans.* **2** (1971) 1979.
20. H. M. TENSI, P. DROPMAN and H. BORCHERS, *Z. Metallkde* **61** (1970) 518.
21. T. SHEPPARD, N. C. PARSON and M. A. ZAIDI, *Met. Sci.* **17** (1983) 481.

# Structure Refinement and Improved Mechanical Properties of Al-20wt.% Si by Rapid Solidification in Conjunction with Strontium Modification

M. VAN ROOYEN, N. M. VAN DER PERS, TH. H. DE KEIJSER and E. J. MITTEMEIJER

Laboratory of Metallurgy, Delft University of Technology, Rotterdamseweg 137, 2628 AL Delft (The Netherlands)

(Received December 3, 1986; in revised form March 11, 1987)

## ABSTRACT

*The effect of the addition of strontium on the morphology, microstructure and hardness of melt-spun Al-Si ribbons as well as on the morphology, hardness and tensile properties (in both the longitudinal and the transverse directions) of the ribbon consolidates (hot extrusion) was investigated.*

*Longitudinal sections of Al-Si ribbons both without strontium and with strontium showed three zones: a chill zone at the wheel side with primary aluminium dendrites grown more or less perpendicular to the wheel surface, a central zone consisting of a submicroscopic eutectic with randomly distributed primary aluminium dendrites and a top zone of a submicroscopic eutectic with primary silicon crystallites. For the ribbons with strontium, the primary aluminium dendrites were coarser while, in the chill zone of the ribbons without strontium, silicon particles were identified.*

*Optical microscopy and X-ray diffraction analyses indicate that the addition of strontium led to a much finer and more homogeneous structure with respect to grain size, preferred orientation, lattice defects and solid solubility.*

*The mechanical properties of the consolidates were examined by tensile testing and hardness measurements. Chopping of the ribbons and subsequent extrusion eliminated the anisotropy of mechanical properties; that is, the transverse properties were substantially improved. Ultimately, structure refinement due to liquid quenching in conjunction with strontium modification led to both an increase of about 85% in tensile strength and an increase of about 300% in ductility compared with extruded conventionally cast material with a corresponding silicon content. However, it is probable that, because of the process of consolidation, about half of the innate strength*

*improvement reached as a result of rapid solidification and strontium modification has not been utilized yet.*

## 1. INTRODUCTION

The mechanical properties of metallic materials can be improved in various ways. Grain refinement can in principle bring about an increase of both strength and ductility [1, 2].

Rapid quenching from the melt of aluminium-based alloys, as for example achieved by melt spinning, produces very fine grains as a result of a large undercooling on solidification [3, 4]. However, as a consequence of the high cooling rate required, at least one dimension of the rapidly quenched product is very small. For practical purposes a subsequent compaction treatment is necessary. Consolidation can be obtained by (hot) extrusion. Then, because of the elevated temperatures involved, an undesired coarsening of the microstructure can occur, leading to a partial loss of the initial gain of mechanical strength. Nevertheless, the alternative route of manufacturing by rapid solidification processing has potentials for a net improvement of the mechanical properties compared with those of conventionally cast material; for example, an increase of 50% in the ultimate tensile strength was obtained for Al-20at.%Si [5, 6].

It is well known that the mechanical performance of conventionally cast Al-Si alloys can be enhanced by adding a very small amount of strontium to the melt [7]. This so-called modification arises from the refinement of the microstructure.

The present study proposes a combination of "chill modification" (by melt spinning) and "impurity modification" (by the addition of

strontium) as a means of enhancing progressively the microstructural refinement and thus the mechanical properties of the alloys.

Melt spinning and subsequent extrusion of the as-melt-spun ribbons leads to extrudates exhibiting significant anisotropy of the mechanical properties [5]. In the present work, isotropic mechanical properties are aimed at by chopping the melt-spun ribbons before extrusion.

## 2. EXPERIMENTAL PROCEDURES

### 2.1. Production and consolidation of melt-spun ribbons

The Al-18.7at.%Si-0.031at.%Sr alloy was prepared from 99.998 wt.% Al, 99.99 wt.% Si and the master alloy Al-3.5wt.%Sr. Melt spinning was performed in an air atmosphere; the metal was melted in a graphite crucible by induction heating and ejected through an orifice in the bottom of the crucible (diameter, 0.9 mm) onto the cylindrical surface of a rotating copper wheel (diameter, 294 mm; circumferential velocity,  $30.8 \text{ m s}^{-1}$ ). For further details, see ref. 5. A granulator was used for chopping a part of the ribbons into small pieces with an average length of about 5 mm.

The unchopped ribbons were precompact to billets with a relative density of about 67%. Before extrusion, preheating occurred in the extrusion chamber for 30 min at 725 K. A degassing procedure was unnecessary; it would cause the properties to deteriorate (by coarsening) [5]. Extrusion was also carried out at 725 K with an extrusion ratio of 25. The extrusion speed was about  $1 \text{ m min}^{-1}$ , which corresponds to a ram speed of approximately  $7 \text{ cm min}^{-1}$ . The chopped ribbons were put in the extrusion chamber immediately after chopping; preheating and extrusion were executed as for the unchopped material.

### 2.2. Characterization of the microstructure

#### 2.2.1. Microscopy

Optical microscopy analysis was performed on longitudinal sections of ribbons and extrudates using a Neophot-2 microscope (Carl-Zeiss, Jena). For etching, a modified Keller and Wilcox's reagent was applied (2% $\text{HCl}$ -4% $\text{HNO}_3$ -1% $\text{HF}$ - $\text{H}_2\text{O}$ ).

Scanning electron microscopy was performed with a JEOL JSM 840 instrument.

#### 2.2.2. X-ray diffractometry

Specimens for X-ray diffraction analysis consisted of a number of ribbons placed parallel to each other, parallel to the spinning direction and with either all wheel or all upper sides exposed to the X-rays. The small effective penetration depth of the X-rays with respect to the total ribbon thickness allows detection of differences between the microstructure of the wheel sides and that of the upper sides of the ribbons.

{111} pole figures of the aluminium-rich phase were determined according to the Schulz reflection technique using a Siemens Lücke-type texture goniometer, applying  $\text{Cu K}\alpha$  radiation.

Line profiles were recorded using a Siemens-type D500 diffractometer ( $\text{Cu K}\alpha$ ) and a Siemens-type  $F\omega$  diffractometer ( $\text{Cr K}\alpha$ ), both equipped with a graphite monochromator in the diffracted beam. The radiation applied was chosen so that large-angle reflections of the silicon- and aluminium-rich phases could be analysed. Instrumental aberrations affecting the broadening and peak position were corrected by applying standard specimens of silicon and aluminium with no deformation and of high purity.

For the ribbons the line-broadening parameters were derived from the Al{222} reflections ( $\text{Cr K}\alpha$ ) and Si{311} reflections ( $\text{Cu K}\alpha$ ) using the Voigt deconvolution method [8]. The lattice parameters were obtained from the Al{222} reflection ( $\text{Cr K}\alpha$ ), after correction for background and after elimination of the  $\alpha_2$  component; the peak position was determined by fitting a parabola to the top of the  $\alpha_1$  profile.

Further, longitudinal sections of the extrudates were investigated. For the aluminium-rich phase both the line-broadening parameters and the lattice parameters were derived from Al{420} reflections ( $\text{Cu K}\alpha$ ), while for determination of the line-broadening parameters of the silicon-rich phase the Si{531} reflection ( $\text{Cu K}\alpha$ ) was analysed.

#### 2.3. Differential scanning calorimetry

The precipitation behaviour of the melt-spun material was analysed with a Perkin-Elmer DSC-2 differential scanning calorimeter.

The effective activation energy was determined by application of the Kissinger [9] method employing heating rates of 5, 10, 20 and 40 K min<sup>-1</sup>. For a justification of the application of the Kissinger method to solid state transformations, see ref. 10.

## 2.4. Mechanical properties

### 2.4.1. Hardness

The hardness was measured from longitudinal sections of ribbons and extrudates using a Leitz Durimet Vickers microhardness tester. The measurements were performed according to *DIN Standard 50133* [11], employing a load of 10 gf. For each hardness value, at least ten measurements were made.

### 2.4.2. Tensile strength

Tensile specimens in both the longitudinal and the transverse directions of the extruded bars were prepared by machining. The longitudinal test bars were made according to *DIN Standard 50125* [12] with a length-to-diameter ratio of 10. The preparation of the transverse test bars is described in detail in ref. 5. All tensile tests (about four for each value presented) were performed on an Instron tensile-testing machine (model TTCML MI 1.4.6).

## 3. MELT-SPUN RIBBONS

### 3.1. Morphology

In the Al-Si ribbons both with and without strontium, three zones are present (Fig. 1): a chill zone adjacent to the wheel with primary aluminium-rich dendrites (approximately) perpendicular to the wheel surface; a central zone with primary aluminium-rich dendrites embedded in a very fine submicroscopic eutectic matrix (the density of the primary aluminium-rich dendrites decreases with increasing distance to the wheel surface (decreasing undercooling)); a top zone consisting of primary silicon-rich particles also embedded in a submicroscopic eutectic matrix. However, apart from the morphological similarities along the main lines indicated, distinct differences in morphology between the Al-Si ribbons with strontium and those without strontium do occur (*cf.* Figs. 1(a) and 1(b)). In the chill zone of the ribbons with strontium no primary silicon-rich particles are present, in contrast

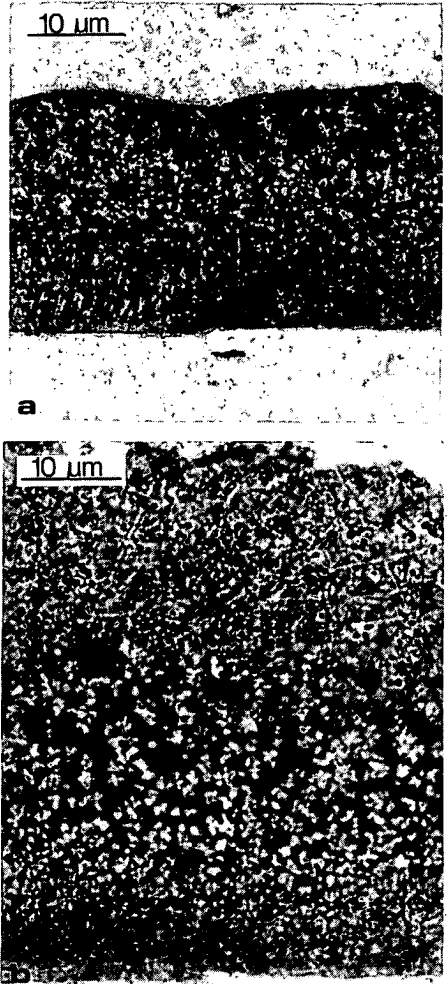


Fig. 1. Bright field optical micrographs of (a) a longitudinal section of an Al-Si ribbon and (b) a longitudinal section of an Al-Si-Sr ribbon (both etched with modified Keller and Wilcox's reagent).

with the chill zone of the ribbons without strontium. Further, in the ribbons with strontium, the primary aluminium-rich dendrites in both the chill and the central zone appeared to be coarser than in the ribbons without strontium. So, even after rapid solidification by melt spinning, the addition of strontium to a hypereutectic Al-Si alloy does result in a change in the solidification morphology.

TABLE 1

Microstructure of the ribbons as revealed by X-ray diffraction

Alloy	Si content (at.%)	Thick-ness ( $\mu\text{m}$ )	Ribbon part	Texture of Al-rich phase	Integral linewidth $2\theta$ (deg)		$a_{\text{Al}}$ {222} Cr K $\alpha$ (nm)	$x_{\text{Si}}$ (at. % Si)
					Al-rich phase, {222} Cr K $\alpha$	Si-rich phase, {311} Cu K $\alpha$		
Al-20wt.%Si without Sr	20.2	40	Upper side	Random	1.59	0.44	0.404400	3.05
Al-20at.%Si without Sr	20.2	40	Wheel side	Weak	2.13	0.65	0.404380	3.17
Al-18.7wt.%Si with 0.03 wt.% Sr	18.7	56	Upper side	Random	1.98	0.53	0.404510	2.41
Al-18.7wt.%Si with 0.03 at.% Sr	18.7	56	Wheel side	Random	1.79	0.53	0.404505	2.45

$a_{\text{Al}}$ , lattice parameter of the aluminium-rich phase at 298 K;  $x_{\text{Si}}$ , composition of the aluminium-rich phase obtained from  $a_{\text{Al}}$  and  $a_0$  for pure aluminium as measured according to refs. 15 and 16 ( $a_0 = 0.404\ 930$  nm at 298 K).

This change in morphology agrees with solidification theories based on experiments with conventional cooling rates. By the addition of strontium to Al-Si alloys the (skewed) coupled zone in the phase diagram is shifted to higher silicon contents [13, 14]. This implies that, in the solidification of hypereutectic Al-Si alloys with strontium, a smaller undercooling is required for the growth of primary aluminium-rich dendrites and also that, for the same degree of undercooling, a finer eutectic matrix might develop compared with that in Al-Si alloys without strontium.\*

\*A direct verification of the refinement of the eutectic could not be obtained from optical microscopy because of the submicroscopic morphology; however, the different appearance of the primary aluminium-rich and silicon-rich phases in the ribbons with and without strontium indirectly evidenced the refinement (see Section 3.1). Scanning electron microscopy also failed to detect the fineness of the eutectic because of preparation problems. Estimation of particle size from X-ray diffraction line broadening was not possible because (i) the reflections of the aluminium-rich phase originated from both the primary dendrites (relatively large crystals) and the eutectic structure (the same holds for the silicon-rich phase) and (ii) not only the finite crystallite size but also lattice imperfections and concentration variations contributed significantly to the line broadening; separation of these contributions caused very large uncertainties.

### 3.2. Microstructure

As revealed by X-ray diffraction, the microstructures of the ribbons with and without strontium are slightly different. The most striking point is that in the absence of strontium the upper and wheel sides have different textures, different amounts of crystal imperfections and different lattice parameters of the aluminium-rich phase (and therefore different silicon contents). No such differences were observed in the presence of strontium (Table 1). Hence, strontium reduces the differences between the microstructures of the wheel and upper sides of the ribbons.

The average lattice parameter of the aluminium-rich phase in the ribbons with strontium differs significantly from that in the ribbons without strontium (0.40451 nm vs. 0.40439 nm; see Table 1). This cannot be ascribed to the fact that strontium is dissolved in the aluminium-rich phase. According to the equilibrium phase diagram, strontium is almost not dissolvable in aluminium [17]. Furthermore, additional experiments indicated that the lattice parameter of the aluminium-rich phase in a melt-spun alloy containing as much as 1 gross at.% Sr was only  $20 \times 10^{-6}$  nm larger than the lattice parameter of pure aluminium. (If Vegard's law is adopted, this corresponds to about 0.01 at.% Sr dissolved in the aluminium-rich phase.) Consequently, the difference

in lattice parameter must be due to a difference in the silicon content of the aluminium-rich phase in the ribbons with and without strontium (see Table 1). As suggested by the ribbon thickness (Table 1), the relatively low silicon content of the aluminium-rich phase in the ribbons with strontium is probably coupled with a relatively low average cooling rate [15] and not with the presence of strontium.

Differential scanning calorimetry analyses of the melt-spun Al-Si ribbons with strontium and those without strontium resulted in activation energies for precipitation of  $87 \text{ kJ mol}^{-1}$  and  $99 \text{ kJ mol}^{-1}$  respectively. According to refs. 18 and 19, the activation energy for diffusion of silicon in aluminium is about  $130 \text{ kJ mol}^{-1}$ . The low activation energy for the melt-spun ribbons could be due to the presence of excess vacancies [16].

### 3.3. Hardness

The Vickers microhardness of the ribbons with strontium is significantly larger than that of the ribbons without strontium, *i.e.* 249 HV 0.01 *vs.* 182 HV 0.01 (see Table 3). So also after rapid solidification of Al-Si alloys by melt spinning, the addition of strontium leads to a significant improvement in the mechanical strength. Just as for conventionally cast alloys, this improvement is undoubtedly due to the refinement of the eutectic phase by strontium (see Section 3.1 and its footnote).

The ribbons with strontium experienced a lower solidification rate than those without strontium (see Section 3.2). In general, for the same alloy (fixed composition) a lower solidification rate results in a lower silicon content of the aluminium-rich phase and in a coarser microstructure, and therefore in poorer mechanical properties. Despite the relatively low cooling rate the ribbons with strontium still have a higher hardness than the ribbons without strontium. This emphasizes the potential of strontium addition in the improvement of mechanical properties of Al-Si alloys.

## 4. CONSOLIDATES

### 4.1. Morphology and microstructure

Longitudinal sections of the extruded bars for the different consolidates prepared from

as-liquid-quenched Al-Si ribbons, as-liquid-quenched strontium-modified Al-Si ribbons and as-liquid-quenched strontium-modified and subsequently chopped Al-Si ribbons respectively are shown in Figs. 2(a), 2(b) and 2(c).

The original ribbon boundaries cannot be discerned. This indicates a good bonding between the constituents of the extrudates (see also the discussion in refs. 5 and 6). Phase contrast microscopy revealed that silicon particles frequently occupy the grain boundary junctions, and thus the interparticle distance of the dispersed silicon phase appears to govern the ultimate matrix grain size. This may explain why the much larger size of the silicon particles in a conventionally cast Al-Si alloy with the same amount of silicon, leads to a much larger matrix grain size after extrusion (Fig. 3; the difference in magnification from those of Figs. 2(a)-2(c) should be noted). It should also be noted that the silicon particles in the liquid-quenched material exhibit a much more globular morphology than those of the conventionally cast material (Figs. 2 *vs.* Fig. 3).

The larger silicon particles, as made visible by optical microscopy (Fig. 2), could have developed by coarsening during extrusion from the initial silicon particles present after liquid quenching, whereas the small amount of significantly smaller silicon particles, as shown by scanning electron microscopy (Fig. 4), could be mainly due to precipitation from the minor amount of silicon originally dissolved in the matrix (*cf.* Section 3.2).

From a comparison of Fig. 2(a) with Figs. 2(b) and 2(c), it is concluded that a smaller average silicon particle size (finer dispersion) results for the material with strontium added. This is consistent with the observation of a finer microstructure in the as-liquid-quenched strontium-modified material (see Section 3.1).

It has been shown earlier [16, 20, 21] that strains develop in dual-phase Al-Si alloys on cooling, as a consequence of the difference between the thermal shrinkage of the aluminium matrix and that of the dispersed silicon particles. Compared with the unstrained condition, an increase in the lattice parameter of the aluminium matrix (and a decrease in the lattice parameter of the silicon particles) and the development of microstrains take place. The values observed after extrusion of the

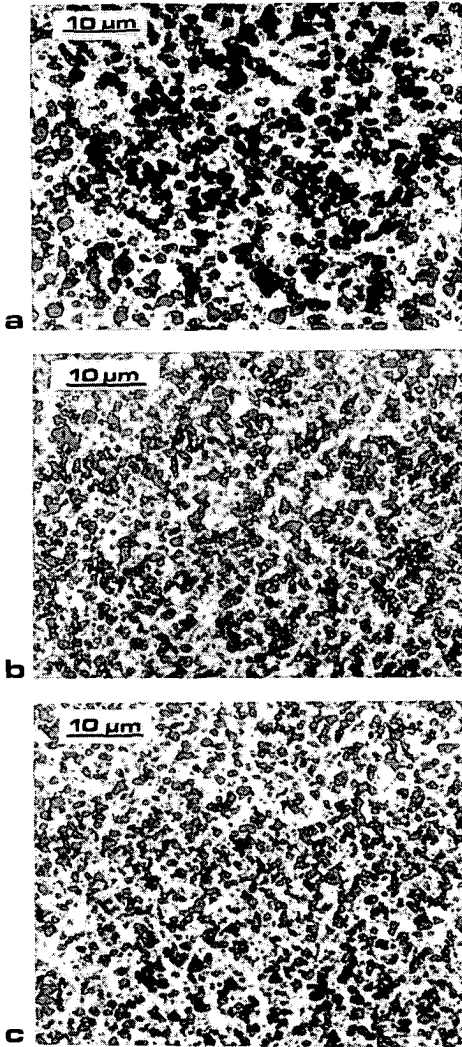


Fig. 2. Bright field optical micrographs of (a) a longitudinal section of a consolidate of Al-Si ribbons without strontium, (b) a longitudinal section of a consolidate of strontium-modified Al-Si ribbons and (c) a longitudinal section of a consolidate of strontium-modified and subsequently chopped Al-Si ribbons (all unetched).

ribbon material for the lattice parameter of the aluminium matrix and the structural line broadening (Table 2) can be explained semi-quantitatively in the above sense (*cf.* calculations performed in refs. 16 and 21).

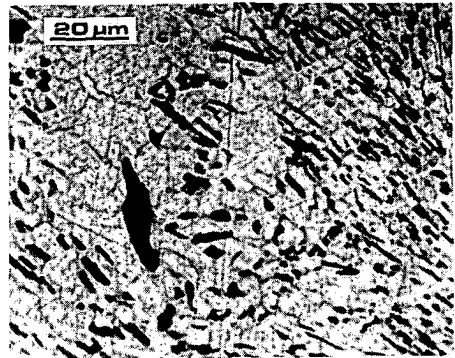


Fig. 3. Phase contrast optical micrograph of a longitudinal section of an extrudate of conventionally cast Al-Si (etched with Keller and Wilcox's reagent).

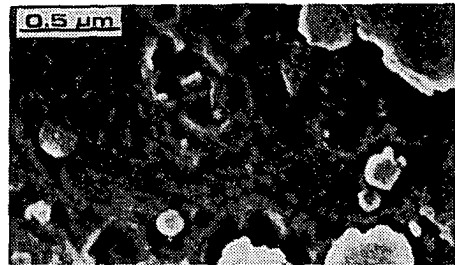


Fig. 4. Scanning electron micrograph of a longitudinal section of a consolidate of Al-Si-Sr ribbons (etched with Keller and Wilcox's reagent).

TABLE 2

Microstructure of consolidates as revealed by X-ray diffraction

Alloy	Integral linewidth		$a_{Al}$ , {420} Cu K $\alpha$ (nm)
	$2\theta$ (deg)		
	<i>Al-rich phase,</i> {420} Cu K $\alpha$	<i>Si-rich phase,</i> {531} Cu K $\alpha$	
CC Al-Si	0.13	0.06	0.404930
LQ Al-Si	0.19	0.35	0.404990
LQ Al-Si-Sr	0.19	0.38	0.405090

Consolidates prepared from conventionally cast Al-Si (CC Al-Si); liquid-quenched Al-Si ribbons (LQ Al-Si) or liquid-quenched strontium-modified Al-Si ribbons (LQ Al-Si-Sr).

$a_{Al}$ , lattice parameter of the aluminium-rich phase at 298 K.

A reduction in the interfacial area between the dispersed phase and matrix contributes to a decrease in the (thermal) microstrain values, as indicated by results presented in refs. 16 and 21. This may explain the relatively small value of the structural broadening, as observed for the extruded conventionally cast alloy where very large silicon particles occur.

#### 4.2. Hardness

Microhardness measurements made on longitudinal sections of the extruded bars established that after extrusion the hardness was homogeneous; no significant differences were obtained between the microhardness values measured in the surface regions and those measured in the cores of the extrudates.

The average microhardness values for the three types of extrudate have been collected together in Table 3. The microhardnesses of all the extrudates from the strontium-modified alloys are equal, implying that chopping the ribbons had no effect on the hardness of the extrudates. Further, the microhardnesses of the extrudates from the strontium-modified alloy are much larger (about 70%) than the microhardness of the extrudate from the pure Al-Si alloy, which is attributed to the finer microstructure obtained for the strontium-modified alloy (see Section 4.1).

#### 4.3. Tensile properties

The measured values of the tensile strength and ductility parameters in both the longitudinal and the transverse directions (denoted by the superscripts // and  $\perp$  respectively) are presented in Table 4. For comparison the corresponding values for the extrudate of conventionally cast material, as given in ref. 5, have been included.

As discussed in a preceding paper [5], alignment of ribbons parallel to the extrusion (longitudinal) direction leads to appreciable anisotropy of the tensile strength:  $\sigma_{\text{uts}}^{\text{//}}/\sigma_{\text{uts}}^{\perp} = 1.44$ . Clearly, this anisotropy is eliminated by chopping the ribbons before extrusion, so that  $\sigma_{\text{uts}}^{\text{//}}/\sigma_{\text{uts}}^{\perp} = 0.97$ , while retaining the improvement in (longitudinal) tensile strength (see below).

It follows from Table 4 that liquid quenching alone enhances the (longitudinal) ultimate tensile strength by 50% and the elongation (at fracture) by 150%. Modification by strontium enhances tensile strength by a further 35%

TABLE 3

Microhardness values for ribbons and ribbon consolidates

Alloy	Vickers microhardness (HV 0.01)	
	Ribbon	Consolidate
LQ Al-Si	182	61
LQ Al-Si-Sr	249 <sup>a</sup>	103
LQ Al-Si-Sr chop	238 <sup>a</sup>	103

Ribbons and ribbon consolidates prepared from liquid-quenched Al-Si (LQ Al-Si), liquid-quenched strontium-modified Al-Si (LQ Al-Si-Sr) or liquid-quenched strontium-modified and subsequently chopped Al-Si (LQ Al-Si-Sr chop).

The data given are average values obtained from at least ten measurements.

<sup>a</sup>Identical within experimental accuracy.

TABLE 4

Tensile properties for four types of consolidate

Consolidate from alloy	$\sigma_{0.2}^{\text{//}}$ (MPa)	$\sigma_{\text{uts}}^{\text{//}}$ (MPa)	$\epsilon_f^{\text{//}}$ (%)	$\psi^{\text{//}}$ (%)	$\sigma_{\text{uts}}^{\perp}$ (MPa)	$\psi^{\perp}$ (%)
CC Al-Si	85	139	4	7	96	10
LQ Al-Si	112	206	10	20	166	7
LQ Al-Si-Sr	146	257	13	31	179	5
LQ Al-Si-Sr chop	143	253	16	29	261	10

Consolidates prepared from conventionally cast Al-Si (CC Al-Si), liquid-quenched Al-Si ribbons (LQ Al-Si), liquid-quenched strontium-modified Al-Si ribbons (LQ Al-Si-Sr) or liquid-quenched strontium-modified and subsequently chopped Al-Si ribbons (LQ Al-Si-Sr chop).

//, parallel to the extrusion direction,  $\perp$ , perpendicular to the extrusion direction;  $\sigma_{0.2}$ , 0.2% offset yield strength,  $\sigma_{\text{uts}}$ , ultimate tensile strength;  $\epsilon_f$ , elongation at fracture;  $\psi$ , reduction in cross-sectional area at fracture.

and the elongation at fracture by a further 150% of the original values. The modification by strontium is ascribed to the finer microstructure of the extrudate compared with the extrudates of liquid-quenched unmodified material (see Section 4.1).

It is anticipated that the mechanical properties of the present extrudates produced from melt-spun strontium-modified Al-20wt.%Si alloy ribbons already suggest commercial application. However, a full use of the poten-

tials of the as-liquid-quenched microstructure has not yet been achieved. Hot extrusion inevitably affects the inherent mechanical properties as a consequence of precipitation and/or coarsening processes which occur at the extrusion temperature. The fraction lost of the innate values of mechanical strength may be assessed in the following way.

Tensile strength is proportional to hardness [22]. The ratio of the microhardness value of the extrudates to that of the as-liquid-quenched ribbons for the strontium-modified material equals  $103/249 = 0.41$  (see Table 3). This implies that more than half of the improvement in mechanical strength attained by liquid quenching is lost during extrusion. (This loss may be even larger because the ratio of tensile strength to hardness is relatively large for a strained material [23], as it is for melt-spun ribbons; see Section 3.3.)

Cold compaction could provide an alternative. However, cold compaction can be impeded by a large, but not available, extrusion pressure. It should also be realized that a very significant temperature increase of the material occurs during (even cold) extrusion [24]. Further study should be devoted to temperature control and deformation processes occurring during extrusion.

## 5. CONCLUSIONS

### 5.1. As-liquid-quenched material

(1) The fineness of the microstructure of melt-spun Al-Si alloys is significantly enhanced by the addition of strontium. This is exemplified by a hardness value which is 35% larger. Hence, as in a conventional casting process, strontium modification is possible in a rapid solidification process also.

(2) The addition of strontium improves the homogeneity of the microstructure; there is no preferred orientation and no significant differences occur between the solid solubilities and the amounts of crystal imperfections at the wheel and the upper sides of the ribbons.

### 5.2. As-extruded material

(1) Modification by the addition of strontium leads to a finer microstructure of the extrudates of liquid-quenched material compared with extrudates of liquid-quenched unmodified material. This is exemplified by

a hardness value which is 70% larger and a tensile strength which is 24% larger.

(2) Anisotropy of mechanical properties in extrudates of melt-spun ribbons can be eliminated by chopping the ribbons before extrusion.

(3) The joint effect of liquid quenching and strontium modification leads to an increase of 85% in the tensile strength and of 300% in the ductility over the corresponding values for conventionally cast material. This suggests that rapid solidification processing can be used for commercial application of Al-20wt.%Si alloys.

## ACKNOWLEDGMENTS

We are indebted to Mr. P. F. Colijn for assistance with optical and scanning electron microscopy, to Mr. P. de Ruyter for technical assistance and to Professor B. M. Korevaar for stimulating discussions.

The financial support of the Foundation for Fundamental Research of Matter is gratefully acknowledged.

## REFERENCES

- 1 G. E. Dieter, *Mechanical Metallurgy*, McGraw-Hill, London, 2nd edn., 1976, Chapter 5.
- 2 R. P. Carreker, Jr., and W. R. Hibbard, Jr., *Trans. AIME*, 209 (1957) 1157.
- 3 H. Jones, *J. Mater. Sci.*, 19 (1984) 1043.
- 4 R. W. Cahn, in R. W. Cahn and P. Haasen (eds.), *Physical Metallurgy*, North-Holland, Amsterdam, 3rd edn., 1983, p. 1836.
- 5 M. van Rooyen, J. A. van der Hoeven, L. Katgerman, P. van Mourik, Th. H. de Keijser and E. J. Mittemeijer, *Powder Metallurgy Aerospace Materials Conf.*, Berne, November 12-14, 1984.
- 6 M. van Rooyen, P. F. Colijn, Th. H. de Keijser and E. J. Mittemeijer, *J. Mater. Sci.*, 21 (1986) 2273.
- 7 I. J. Polmear, *Light Alloys (Metallurgy of Light Metals)*, Edward Arnold, London, 1981, pp. 118-120.
- 8 Th. H. de Keijser, J. I. Langford, E. J. Mittemeijer and A. B. P. Vogels, *J. Appl. Crystallogr.*, 15 (1982) 308.
- 9 H. E. Kissinger, *Anal. Chem.*, 29 (1957) 1702.
- 10 L. V. Meisel and P. J. Cote, *Acta Metall.*, 31 (1983) 1053.
- 11 *DIN Stand. 50133*, 1972 (Deutsches Institut für Normung).
- 12 *DIN Stand. 50125*, 1951 (Deutsches Institut für Normung).

- 13 W. Kurz and D. J. Fisher, *Int. Metall. Rev.*, 5-6 (1979) 177.
- 14 W. Meijer, *Aluminium*, 11 (1974) 699.
- 15 A. Bendijk, R. Delhez, L. Katgerman, Th. H. de Keijser, E. J. Mittemeijer and N. M. van der Pers, *J. Mater. Sci.*, 15 (1980) 2803.
- 16 P. van Mourik, E. J. Mittemeijer and Th. H. de Keijser, *J. Mater. Sci.*, 18 (1983) 2706.
- 17 H. Nowotny and H. Wesenberg, *Z. Metallkd.*, 31 (1939) 363.
- 18 W. Koster and W. Knorr, *Z. Metallkd.*, 45 (1954) 616.
- 19 R. F. Mehl, F. N. Rhines and K. A. von den Steinen, *Met. Alloys*, 13 (1941) 41.
- 20 E. J. Mittemeijer, P. van Mourik and Th. H. de Keijser, *Philos. Mag. A*, 43 (1981) 1157.
- 21 P. van Mourik, Th. H. de Keijser and E. J. Mittemeijer, in P. W. Lee and R. S. Carbonara (eds.), *Proc. 1st Int. Conf. on Rapidly Solidified Materials, San Diego, CA, February 3-5, 1986*, American Society for Metals, Metals Park, OH, 1986, p. 341.
- 22 D. Tabor, *The Hardness of Metals*, Oxford University Press, London, 1951, p. 107.
- 23 J. B. Cahoon, W. H. Broughton and A. H. Kutzak, *Metall. Trans.*, 2 (1971) 1979.
- 24 T. Sheppard, *Met. Technol.*, 8 (1981) 130.

## Summary

This thesis involves a number of publications concerned with the morphology, microstructure and precipitation behaviour of melt-spun AlMg(12.1-17.2 at% Mg) and AlSi(1.3-19.1 at% Si) ribbons. The structure and mechanical properties of the melt-spun ribbons after hot extrusion were also investigated, while further in the case of AlSi alloys the influence of Sr addition was analysed.

With light microscopy three zones were observed in the ribbons. First, at the wheelside a chill zone appears with grain boundaries initially perpendicular to the wheel surface. Then a central zone of columnar grains caused by a unidirectional heat flow in the freezing metal. Finally, a top layer consisting of equiaxed grains, which can be ascribed to a combination of a relatively slow heat transfer (constitutional undercooling) and convection in the liquid.

X-ray diffraction analysis showed that all AlMg alloys were single-phase, whereas the AlSi alloys were dual-phase. By texture analysis a decreasing distinctness of preferred orientation with increasing alloying-element content was observed.

The heat effects and kinetics of precipitation in liquid-quenched (LQ; rapidly solidified) AlMg and AlSi alloys were examined with differential scanning calorimetry (DSC). For comparison, also solid-quenched (SQ; quenched after annealing the solid at elevated temperature) AlMg and AlSi alloys of identical compositions were investigated.

In the case of AlMg the results were consistent with the following precipitation model:

(1) on aging preprecipitates (Guinier-Preston zones) and clustering of vacancies (void/loop formation) occurs;

(2) on subsequent annealing the GP-zones dissolve before  $\beta'/\beta$  precipitation develops.

In SQ alloys the GP-zone formation proceeds more rapidly than in LQ alloys due to a larger amount of excess vacancies retained after (drastic) SQ than after LQ (melt-spinning). On annealing  $\beta'/\beta$  precipitation (heterogeneous nucleation) starts at a lower temperature in LQ alloys than in SQ alloys because of the larger amount of structural heterogeneities (grain-boundary area) in LQ alloys. The GP-zone solvus was estimated by adopting established models for the chemical and strain contributions to the free enthalpy of mixing. Quantitative analysis of the heat of dissolution of GP-zones demonstrated a linear relation between the enthalpy of formation of GP-zones and the dissolved magnesium atomic fraction  $x$ :

$$\Delta H_{GP}(x) = -2160 \cdot x + 1932 \text{ J/mole.}$$

Analysis of the kinetics of the formation of GP-zones showed that this is governed by the process of nucleation and excess-vacancy enhanced diffusion of magnesium. The dissolution of GP-zones is controlled by the diffusion of

magnesium. Values found for the activation energy of dissolution are smaller than those for volume diffusion of magnesium, which can be explained by the emitting of vacancies from vacancy voids/loops; the latter becoming unstable at the temperatures where the GP-zones dissolve. The values for the activation energy of GP-zone dissolution in SQ alloys are significantly smaller than in LQ alloys. This also indicates that the amount of excess vacancies retained after SQ is larger than after LQ.

For AlSi the precipitation of silicon starts in LQ alloys at lower temperatures than in SQ alloys; this is due to a larger driving force caused by a higher supersaturation. Another significant difference between LQ and SQ alloys is also observed. In LQ alloys the total exothermic heat effect is caused by precipitation of silicon initially dissolved in the supersaturated Al-rich phase and by coarsening of the silicon-particles already present after rapid solidification. The heat of precipitation in SQ alloys equals, within the experimental accuracy, that of dissolution of silicon in the Al-rich phase (the latter calculated from the equilibrium phase diagram). The surplus heat production for the LQ alloys is mainly ascribed to reduction of the amount of interfacial area and possibly also to the atomic volume difference for silicon as second-phase particles (precipitated in the low temperature region of the quench) and as dissolved element. For both LQ and SQ AlSi alloys the activation energies for silicon precipitation are smaller than that for volume diffusion of silicon in aluminium. This is due to a higher amount of quenched-in excess vacancies. In the case of hypo-eutectic alloys the activation energy increased with increasing silicon content, which can be explained by a decreasing solidification start temperature and a decreasing Al-matrix grain size with increasing alloying-element content, which cause a decrease of the excess vacancy concentration.

Both melt-spun ribbons and conventionally cast materials of identical compositions were consolidated by hot extrusion.

In general, compared to the extrusion of massive conventional castings, additional redundant work during extrusion is required to achieve a coherent product from melt-spun ribbons.

The hardness of the AlMg ribbons increased with increasing magnesium content as a result of solid-solution strengthening, showing a linear relation between the hardness and the square root of solute atom concentration. The extrudates of the AlMg-ribbons demonstrated a significant decrease of hardness, due to large increase of grain size.

The AlSi ribbon material also showed an increasing hardness with increasing silicon content. This is ascribed to both solid-solution strengthening and dispersion strengthening. The extrusion-induced increase of grain size and the progress of precipitation/coarsening of the second phase contributed to a drastic decrease of hardness of the AlSi-compacts.

The mechanical properties of extruded AlMg and AlSi alloys were determined in both longitudinal and transverse directions, while also the effects of degassing before consolidation were analysed. For comparison, the mechanical properties of extruded conventionally cast materials of identical compositions were also determined.

The increase of tensile strength of AlMg and AlSi extrudates on increasing alloying element content is dominantly due to solid solution and dispersion strengthening mechanisms respectively. The less intimate bonding between the extruded AlMg-ribbons compared with that of AlSi can be ascribed to the difference in thickness of the oxide layer occurring at the surfaces of the ribbons.

In the case of AlMg the tensile strength of consolidated ribbons is smaller than that of extruded conventional castings. This holds especially for the transverse properties. The ductility, expressed by the elongation at fracture, showed a decrease and subsequent increase on increasing the alloying-element content in extruded AlMg alloys; this is ascribed to the predominance of either dynamic recovery (below about 3 at.% Mg) or dynamic recrystallization (above about 3 at.% Mg).

For the AlSi alloys the tensile strength of the ribbon extrudates was significantly larger (up to 50 %) than that of the extruded conventional castings.

Degassing before extrusion at high temperature leads to growth of matrix grains and/or precipitation and coarsening of second-phase particles, which has detrimental effects upon tensile strengths. It is shown that for many alloys vacuum degassing can be replaced by preheating before consolidation.

The influence of addition of strontium to AlSi alloys upon the structure and mechanical properties was also analysed. In the as-liquid-quenched ribbons addition of Sr lead to a significantly improved fineness and homogeneity of the microstructure. Also the microstructure of the extruded ribbons was refined by Sr modification, while an increase of 85 % of the tensile strength and 300 % of the ductility (compared with extruded conventionally cast alloys) was achieved.

The main advantage of the rapid-solidification techniques appears to be the resulting ultrafine grain size and the very fine second phase-dispersion. Retention of the favourable mechanical properties, as obtained by rapid solidification, requires alloy development to minimize microstructural changes during subsequent consolidation.

## Samenvatting

Dit proefschrift omvat een aantal publikaties betreffende de morfologie, mikrostructuur en het precipitatiegedrag van geflitsgiete AlMg(12.1-17.2 at.%Mg) en AlSi(1.3-19.1 at.%Si) legeringen. Eveneens werden de structuur en mechanische eigenschappen van warm geëxtrudeerd geflitsgiet lint bestudeerd. Verder werd de invloed van toevoeging van strontium aan AlSi-legeringen onderzocht.

Met lichtoptische mikroskopie werden in langsdoorsneden van de geflitsgiete linten drie zones waargenomen. Aan de wielzijde een afschrikzone, welke wordt gekenmerkt door kristallen, die in de beginfase van het stolproces loodrecht op het wieloppervlak uitgroeien. Vervolgens een centrale zone van kolomvormige kristallen, ontstaan t.g.v. een unilaterale warmtestroom in het stollende metaal. Tenslotte, de toplaag aan de luchtzijde, opgebouwd uit equ-axiale kristallen; deze kunnen worden toegeschreven aan een combinatie van een relatief langzame warmteoverdracht (wat aanleiding kan geven tot constitutionele onderkoeling) en konvektie in de vloeistof.

Röntgendiffractie toonde aan dat alle AlMg-legeringen éénfasig waren, de AlSi-legeringen daarentegen tweefasig. Via textuuranalyse kon worden vastgesteld dat de voorkeursoriëntatie van de kristallen in het geflitsgiete lint afneemt met toenemend gehalte legeringselement.

Het warmte-effekt en de kinetiek van de precipitatieprocessen in geflitsgiete AlMg- en AlSi-legeringen werden geanalyseerd met behulp van differentiële calorimetrische analyse (DSC). Ter vergelijking zijn ook vast afgeschrikte legeringen met identieke composities onder dezelfde omstandigheden onderzocht.

Voor wat betreft AlMg waren de resultaten in overeenstemming met het volgende precipitatiemodel.

- (1) bij veroudering treedt er preprecipitatie (Guinier-Preston (GP) zones) en clustering van vakatures (in de vorm van poriën of ringen) op.
- (2) bij voortgaande veroudering lossen de GP-zones op in de matrix, vóórdat er  $\beta'/\beta$ -precipitatie plaatsvindt.

In de vast afgeschrikte legeringen is de vormingssnelheid van GP-zones groter dan in de geflitsgiete materialen. Dit wordt toegeschreven aan een hogere concentratie overschot-vakatures in eerstgenoemde substanties; bij vast afschrikken treedt in het lagere temperatuurgebied een hogere afkoelsnelheid op dan bij het flitsgieten. Verder blijkt uit calorimetrisch onderzoek dat  $\beta'/\beta$ -precipitatie in geflitsgiet materiaal bij lagere temperaturen optreedt dan in vast afgeschrikte legeringen; dit wordt veroorzaakt door een grotere concentratie structuurheterogeniteiten (groter kristalgrensooppervlak) in geflitsgiet lint.

De ligging van de GP-zone solvus werd geschat door toepassing van bekende modellen voor de chemische en elastische bijdragen aan de vrije

mengenthalpie. Kwantitatieve analyse van de oploswarmte van GP-zones toonde een lineaire relatie aan tussen de vormingsenthalpie van GP-zones en de atoomfractie opgelost magnesium, x, volgens:

$$\Delta H_{GP} = -2160 \cdot x + 1932 \text{ J/mol.}$$

Bestudering van de kinetiek van de vorming van GP-zones toonde aan dat deze wordt bepaald door zowel het proces van kiemvorming als de (t.g.v. overschot-vakatures) versnelde diffusie van magnesium. Het oplossen van GP-zones wordt beheerst door de (t.g.v. overschot-vakatures) versnelde diffusie van magnesium. De aktiveringsenergie van het oplossen van GP-zones blijkt lager te zijn dan die van volumediffusie van magnesium, wat kan worden verklaard door de emissie van vakatures uit de vakature ringen/poriën; de laatsten worden instabiel bij temperaturen waar de GP-zones in oplossing gaan. De aktiveringsenergie van het oplossen van GP-zones in vast afgeschrikte materialen is lager dan die van geflitsgiete legeringen. Dit geeft eveneens aan dat de hoeveelheid overschot-vakatures na vast afschrikken groter is dan na flitsgieten.

Kalorimetrisch onderzoek van AlSi-legeringen toonde aan dat de precipitatie van silicium in geflitsgiete legeringen bij lagere temperaturen begint dan in vast afgeschrikte legeringen; dit is te wijten aan een grotere drijvende kracht ten gevolge van een hogere oververzadiging in eerstgenoemde materialen. Een ander significant verschil tussen geflitsgiete en vast afgeschrikte legeringen is dat in geval van eerstgenoemden het totale exotherme warmte-effekt wordt veroorzaakt door zowel precipitatie van silicium uit de oververzadigde legering als vergroving van de siliciumdeeltjes, die na de snelle stolling reeds in uitgescheiden vorm aanwezig zijn. Het exotherme warmte-effekt van de vast afgeschrikte legeringen is, binnen de meetnauwkeurigheid, gelijk aan de m.b.v. het fasendiagram berekende oploswarmte van silicium in de Al-rijke fase. Het surplus warmte-effekt van de geflitsgiete legeringen kan voornamelijk worden toegeschreven aan de verlaging van de hoeveelheid grensooppervlak (vergroving) en mogelijk ook aan het verschil in atomair volume van silicium als tweede fase-deeltje (geprecipiteerd in het lage temperatuurgebied tijdens het afschrikken) en van silicium als opgelost element, beide t.o.v. aluminium.

Zowel voor de vast afgeschrikte als de geflitsgiete AlSi-legeringen is de aktiveringsenergie van precipitatie lager dan die van volumediffusie van silicium in aluminium. Dit wordt veroorzaakt door de aanwezigheid van overschot-vakatures. Verder vertoonden de hypo-eutektische geflitsgiete legeringen een toename van de aktiveringsenergie met toenemend siliciumgehalte, wat kon worden verklaard door een dalende liquidustemperatuur bij stijgend siliciumgehalte en een afnemende kristalgrootte van de Al-rijke fase; beide veroorzaken een verlaging van de hoeveelheid overschot-vakatures.

De hardheid van het geflitsgiete AlMg-lint neemt toe met toenemend magnesiumgehalte ten gevolge van oplosharding, wat zich manifesteert in een lineair verband tussen de hardheid en de wortel van de concentratie opgeloste atomen. Het geëxtrudeerde AlMg-lint vertoonde een daling van de hardheid ten opzichte van die van het lint in geflitsgiete toestand, ten gevolge van een sterke kristalgroei tijdens extrusie.

De geflitsgiete AlSi-legeringen vertoonden eveneens een toename van de hardheid met toenemend gehalte legeringselement, wat wordt veroorzaakt door zowel oplosharding als dispersieharding. De toegenomen kristalgrootte van de primaire fase alsmede de precipitatie/vergroving van de tweede fase-deeltjes leidden ook in dit geval tot een lagere hardheid van het geëxtrudeerde lint t.o.v. het geflitsgiete materiaal.

De mechanische eigenschappen van geëxtrudeerde AlMg- en AlSi-legeringen werden zowel in longitudinale als transversale richting bepaald, terwijl tevens de effecten van ontgassen vóór consolidatie werden geanalyseerd. Ter vergelijking werden de mechanische eigenschappen van geëxtrudeerde conventioneel gegoten materialen onder dezelfde beproevingscondities onderzocht.

De toename van de treksterkte van zowel de AlMg- als de AlSi-legeringen met toenemend gehalte legeringselement wordt voornamelijk veroorzaakt door respektievelijk oploshardings- en dispersiehardingsmechanismen. De zwakkere binding tussen de geëxtrudeerde AlMg-linten, vergeleken met die van AlSi, wordt veroorzaakt door het verschil in dikte van de oxidehuid; eerstgenoemde materialen hebben een grotere laagdikte, zodat een minder hecht metallisch contact mogelijk is.

Bij AlMg is de treksterkte van het geëxtrudeerde geflitsgiete lint lager dan die van het geëxtrudeerde conventioneel gegoten materiaal. Dit geldt met name voor de transversale treksterkte. De taaiheid, uitgedrukt door de breekrek, vertoont een afname (met een minimum bij ca. 3 at.%Mg) en vervolgens een toename met stijgend gehalte legeringselement in de geëxtrudeerde AlMg-legeringen; dit wordt toegeschreven aan het overheersen van dynamisch herstel (beneden circa 3 at.%Mg) of dynamische rekristallisatie (bij gehalten groter dan 3 at.%Mg).

Het geëxtrudeerde AlSi-lint vertoonde een significante toename van de treksterkte t.o.v. geëxtrudeerd conventioneel gegoten materiaal; dit ten gevolge van de aanwezigheid van fijn gedispergeerde tweede fase-deeltjes in het gekompakteerde lint.

Vacuum ontgassen op hoge temperatuur vóór consolidatie leidt tot vergroving van de matrixkristallen en precipitatie en vergroving van tweede fase-deeltjes, wat ongunstige gevolgen heeft voor de mechanische eigenschappen. Aangetoond is dat voor vele legeringen het vacuum ontgassen kan worden vervangen door voorverwarmen vóór consolidatie.

De invloed van toevoeging van strontium aan AlSi-legeringen op de structuur en mechanische eigenschappen werd eveneens onderzocht. In het geflitsgiete lint leidde toevoeging van strontium tot een belangrijke toename van de fijnheid en homogeniteit van de mikrostructuur. Het geëxtrudeerde lint bleek eveneens een fijnere mikrostructuur te vertonen ten gevolge van strontium modificatie, terwijl de treksterkte en de breekrek een toename van 85 %, respectievelijk 300 % t.o.v. de overeenkomstige eigenschappen van het geëxtrudeerde conventioneel gegoten materiaal vertoonden.

De belangrijkste voordelen van snelle stolling blijken de zeer fijne kristallen en tweede fase deeltjes te zijn. Om de gunstige eigenschappen van materialen, zoals d.m.v. snelle stolling verkregen, te behouden is ontwikkeling van legeringen vereist, zodanig, dat er minimale mikrostrukturele veranderingen optreden gedurende het na snelle stolling noodzakelijke consolidatieproces.

## CURRICULUM VITAE

- 1955 geboren te Katwijk aan Zee;
- 1974 eindexamen Atheneum-B, Pieter Groencollege te Katwijk aan Zee;
- 1982 doktoraal examen Metaalkunde, Technische Universiteit Delft;
- 1982-1987 wetenschappelijk medewerker in tijdelijke dienst van de Stichting voor Fundamenteel Onderzoek der Materie, (F.O.M.). Het onderzoek, gefinancierd door de Stichting Technische Wetenschappen (S.T.W.), werd verricht in de vakgroep Produktietechnologie, Sektie Warmtebehandeling, Laboratorium voor Metaalkunde, Technische Universiteit Delft